

**SPECTROSCOPY OF SUPERNOVA HOST GALAXIES
FROM THE SDSS-II SN SURVEY
WITH THE SDSS AND BOSS
SPECTROGRAPHS**

by

Matthew Dwaune Olmstead

A dissertation submitted to the faculty of
The University of Utah
in partial fulfillment of the requirements for the degree of

Doctor of Philosophy

in

Physics

Department of Physics and Astronomy

The University of Utah

December 2013

Copyright © Matthew Dwaune Olmstead 2013

All Rights Reserved

The University of Utah Graduate School

STATEMENT OF DISSERTATION APPROVAL

This dissertation of Matthew Dwaune Olmstead

has been approved by the following supervisory committee members:

<u>Kyle Dawson</u>	, Chair	<u>July 23, 2013</u>
		Date Approved

<u>Adam Stallard Bolton</u>	, Member	<u>July 23, 2013</u>
		Date Approved

<u>Benjamin C. Bromley</u>	, Member	<u>July 23, 2013</u>
		Date Approved

<u>Andrey Rogachev</u>	, Member	<u>July 23, 2013</u>
		Date Approved

<u>Tolga Tasdizen</u>	, Member	<u>July 23, 2013</u>
		Date Approved

and by Carleton Detar, Chair of
the Department of Physics and Astronomy

and by David B. Kieda, Dean of the Graduate School.

ABSTRACT

Type Ia supernovae (SNe Ia) have been used as standard candles to measure cosmological distances. The initial discovery of the accelerated expansion of the universe was performed using ~ 50 SNe Ia. Large SNe surveys have increased the number of spectroscopically-confirmed SNe Ia to over a thousand with redshift coverage beyond $z = 1$. We are now in the age of abundant photometry without the ability for full follow-up spectroscopy of all SN candidates. SN cosmology using these large samples will increasingly rely on robust photometric classification of SN candidates.

Photometric classification will increase the sample by including faint SNe as these are preferentially not observed with follow-up spectroscopy. The primary concern with using photometrically classified SNe Ia in cosmology is when a core-collapse SNe is incorrectly classified as an SN Ia. This can be mitigated by obtaining the host galaxy redshift of each SN candidate and using this information as a prior in the photometric classification, removing one degree of freedom. To test the impact of redshift on photometric classification, I have performed an assessment on photometric classification of candidates from the Sloan Digital Sky Survey-II (SDSS-II) SN Survey. I have tested the classification with and without redshift priors by looking at the change of photometric classification, the effect of data quality on photometric classification, and the effect of SN light curve properties on photometric classification.

Following our suggested classification scheme, there are a total of 1038 photometrically classified SNe Ia when using a flat redshift prior and 1002 SNe Ia with the spectroscopic redshift. For 912 (91.0%) candidates classified as likely SNe Ia without redshift information, the classification is unchanged when adding the host galaxy redshift.

Finally, I investigate the differences in the interpretation of the light curve properties with and without knowledge of the redshift. When using the SALT2 light curve fitter, I find a 17% increase in the number of fits that converge when using the spectroscopic redshift. Without host galaxy redshifts, I find that SALT2 light curve fits are systematically biased towards lower photometric redshift estimates and redder colors in the limit of low signal-to-noise data.

To my wife Stephanie

CONTENTS

ABSTRACT	iii
LIST OF TABLES	vii
LIST OF FIGURES	viii
ACKNOWLEDGMENTS	x
CHAPTERS	
1. INTRODUCTION TO SUPERNOVA ASTRONOMY	1
1.1 Introduction	1
1.2 Supernova Astrophysics	3
1.2.1 SN Ia	3
1.2.1.1 White Dwarf Progenitor	3
1.2.1.2 Single-Degenerate Scenario	6
1.2.1.3 Double-Degenerate Scenario	6
1.2.2 Core-Collapse SN	7
1.2.2.1 SN Ib/Ic	7
1.2.2.2 SN II	9
1.2.3 Light Curve Fitting	9
1.2.3.1 SALT2	10
1.2.3.2 MLCS2k2	11
1.3 SN Cosmology	11
1.3.1 Cosmology Review	11
1.3.1.1 Luminosity Distance	13
1.3.2 Spectroscopic SN Ia	13
1.3.2.1 1990s	13
1.3.2.2 2000s	14
1.3.2.3 2010s and Beyond	14
1.3.3 Photometric SN Ia	17
1.3.4 Correlations Between SN Ia Properties and Host Galaxy Properties	17
2. THE SDSS AND BOSS SPECTROGRAPHS	19
2.1 Introduction	19
2.2 SDSS and BOSS Spectrograph Design and Predicted Optical Performance	20
2.2.1 Resolving Power	20
2.2.2 Throughput and Signal to Noise Ratio	20
2.2.3 Flexure	22
2.2.4 BOSS Detector Read Noise and Dark Current	22
2.3 SDSS and BOSS Spectrograph Performance	24
2.3.1 Spectroscopic Pipeline	24
2.3.2 Spectrograph Performance	27
2.3.2.1 Wavelength Coverage	27
2.3.2.2 Spectral Resolution	28

2.3.2.3 Throughput	31
2.3.3 Flexure	35
2.3.4 CCD and Electronics Performance	39
3. SUPERNOVA HOST GALAXY TARGET SELECTIONS	42
3.1 Imaging and Light curves	42
3.2 Photometric Classification	43
3.3 BOSS Target Selection	46
3.4 BOSS Observations	47
3.5 Photometric Classification and Host Galaxy Differences Between C13 and the SDSS-II SN Data Release	48
3.6 Spectroscopic Data Reduction and Redshift Determination	49
3.7 SDSS Spectroscopy of SN Host Galaxies	54
3.8 Host Galaxy Ambiguity	58
4. PERFORMANCE OF PHOTOMETRIC SN CLASSIFICATION	60
4.1 Photometric Typing with SDSS and BOSS Redshifts	62
4.2 Comparison of Classification Techniques	64
4.3 Effects of Data Quality on Contamination and Completeness	66
5. GALAXY PROPERTIES	71
5.1 Photometric Galaxy Properties with SDSS and BOSS Redshifts	71
5.2 Galaxy Properties from SDSS and BOSS Spectra	72
5.3 Correlating SN Properties With Galaxy Properties	77
6. SN IA LIGHT CURVE PROPERTIES	82
6.1 Effects of Light Curve Parameters on Contamination and Completeness	82
6.2 Distribution of SN Light Curve Properties With Redshifts From the Host Galaxies	85
6.3 SN Light curve Properties With and Without Host Galaxy Redshifts	85
7. CONCLUSIONS	93
7.1 Summary	93
7.2 Summary of Other Related Work	94
7.3 Future Work	97
REFERENCES	98

LIST OF TABLES

1.1 Types of Iron Core-Collapse SN	8
2.1 Design Predictions and Measured Performance for SDSS and BOSS	25
2.2 CCD Performance for SDSS and BOSS	40
3.1 Sample Selection	45
3.2 Target Priority	45
3.3 Properties of Figure 3.2 Spectra	51
3.4 BOSS Target Properties	53
4.1 SN Classification	63
4.2 Classification Statistics	65
4.3 Typing Approach Contamination and Completeness	67
4.4 Data Quality Effects of Full Photometric Classification	69
5.1 Summary of SN Ia Host Galaxy Properties	73
6.1 Light Curve Restrictions	84

LIST OF FIGURES

1.1	Example spectra of four different SN spectral classes observed in the SDSS-II SN Survey.	4
1.2	An artists rendition of a binary system consisting of a white dwarf star and a companion star.	6
1.3	A cross-section of an evolved, massive star ($M > 8M_{\odot}$) before core has begun to collapse.	8
1.4	The light curve shapes of SNII-P and SNII-L.	10
1.5	Hubble diagram with best fit cosmology for a flat Λ CDM universe using only supernovae.	15
1.6	Λ CDM model and w CDM model with confidence regions.	16
2.1	Predicted resolving power, R , as a function of wavelength for the SDSS and BOSS spectrographs	21
2.2	Contour image of the BOSS CCDs showing the RMS width σ_p of the line-spread function in native pixels to demonstrate the predicted variation in resolution over the focal plane.	22
2.3	Expected throughput for the SDSS and BOSS spectrographs.	23
2.4	Raw arc image taken with the BOSS spectrograph.	26
2.5	The resolving power for BOSS (gray) and SDSS (red).	29
2.6	The requirements and the measured resolving power for the two BOSS spectrographs.	30
2.7	The RMS width in pixels in the wavelength direction for each of the four BOSS CCDs.	31
2.8	Throughput curves for SDSS (black) and BOSS (red).	33
2.9	Ratio of throughput (BOSS/SDSS) after applying a median smoothing kernel of width 100 pixels.	34
2.10	Photograph of the spectrographs mounted to the Cassegrain rotator.	35
2.11	Gravity induced image motion in SDSS Spectrograph 1 as a function of rotator angle for a zenith angle of 72°	36
2.12	Gravity induced image motion in BOSS Spectrograph 1 as a function of rotator angle for a zenith angle of 72°	38
3.1	The projected five year coverage of BOSS in the South Galactic Cap in equatorial coordinates.	47
3.2	A selection of BOSS spectra with secure redshift from the observed SN host galaxy sample.	50
3.3	The distribution of redshifts and r -band cmodel magnitude of the observed SDSS and BOSS samples.	55
3.4	Apparent magnitude as function of S/N and redshift.	56

3.5	A comparison between the BOSS spectroscopic redshift and the SDSS spectroscopic redshift.	57
3.6	Example of a misidentified host galaxy	58
4.1	A comparison between the BOSS spectroscopic redshift and the galaxy photometric redshift.	61
4.2	Distribution of Bayesian probability of being a SN Ia (core-collapse SN) using the host galaxy redshift as a prior	63
4.3	The redshift distribution of galaxies hosting SNe Ia in redshift bins of 0.05.	67
4.4	Example of the light curves for one SN candidate at $z_{spec} = 0.116$ that is in the contamination sample when there are at least 10 epochs.	70
5.1	Distribution of stellar mass and sSFR for the SNe Ia and core-collapse samples.	74
5.2	The r -band absolute magnitude (derived from <code>cmodelmag</code>) distribution for galaxies hosting SN Ia (solid) and core-collapse SN (red, dashed).	75
5.3	The absolute magnitudes of the SN Ia host galaxy sample by filter.	76
5.4	Stellar velocity dispersion distribution and photometric stellar mass estimates as a function of velocity dispersion.	78
5.5	$H\beta$ equivalent width distribution and $H\beta$ equivalent width as a function of photometric stellar mass.	79
5.6	Metallicity as a function of stellar mass and distribution of metallicity.	81
6.1	SALT2 parameters x_1 and c	86
6.2	The best fit SN Ia photometric redshift versus the spectroscopic redshift.	87
6.3	Comparisons of x_1 with and without spectroscopic redshift.	88
6.4	Comparisons of color with and without spectroscopic redshift.	89
6.5	The difference between the SALT2 redshift estimate and the host galaxy spectroscopic redshift as a function of color for different data quality cuts.	91
6.6	A plot of the SALT2 parameters c vs x_1 including the ellipse found in C13.	92
7.1	Hubble diagram for the photometrically-classified SNe Ia sample in C13.	95
7.2	The 68% and 95% confidence contours of Ω_m versus Ω_Λ for the photometrically-classified SNe Ia in C13.	96

ACKNOWLEDGMENTS

I am very grateful to all of the people that have helped me along my graduate school career. I want to first thank my advisor, Kyle Dawson for giving me this chance to work on a variety of interesting topics and for being available for all of my questions and discussions.

I would next like to thank my committee members, Adam Bolton, Ben Bromley, Andrey Rogachev, and Tolga Tasdizen for help along the way and guidance throughout the completion of this thesis.

Thanks to the members of the Dawson group: Peter Brown, David Harris, Chris Ahn, Sarah Moran, and Trey Jensen. Peter, you were very helpful in getting started in all of this and have continued to provide excellent assistance through to completion, thanks again.

I would like to thank Joel Brownstein and Antonio Montero-Dorta for many useful conversations and assistance with the BOSS data products.

To Nao Suzuki, thanks for all of the discussions, advice, and encouragement over the last several months while finishing this thesis and the related paper and for helping me get started on my next project.

To my collaborators in both BOSS and the SDSS SN Survey, thanks for everything you have done in order for these projects to be as successful they have been. Particular thanks to Ravi Gupta, Heather Campbell, Chris D'Andrea, and Maso Sako for all the discussions and the careful reading and revisions of my paper.

Thanks to the staff members of the Department of Physics and Astronomy who have helped me along the way. Special thanks to Mary Ann Woolf who has always been available for anything I wanted to discuss.

CHAPTER 1

INTRODUCTION TO SUPERNOVA ASTRONOMY

1.1 Introduction

Observers of the night sky in centuries and millenia past occasionally saw very bright objects that lasted for several months, now known as supernovae (SNe). The first historical instance of one of these bright objects was visible for eight months and recorded by Chinese astronomers as a guest star in 185 AD and is now known as SN 185. Another guest star made an appearance for European and Asian observers in 1006, likely the brightest such event in recorded history. This transient was visible during the day and is called SN 1006. In 1054, Chinese astronomers again recorded a guest star and it was visible for the better part of two years. The Crab Nebula is the remnant of SN 1054. Another historically important SN was first observed in 1572. SN 1572, also known as Tycho's supernova, was observed by many European observers before the Danish astronomer Tycho Brahe, but was named after him for his work on astronomy using SN 1572. With precise measurements (using only the naked eye), the ancient idea of the unchanging heavens was challenged. The last detected SN in the Milky Way galaxy was SN 1604, known as Kepler's Nova, named for Kepler who observed the explosion for over a year.

With the invention of the telescope, these bright explosions were first detected in other galaxies, beginning with supernova S Andromedae in the Andromeda galaxy in 1885 (de Vaucouleurs & Corwin 1985). Studies in the 1930s by Baade and Zwicky of nearby galaxies saw these bright explosions and initially considered them a new class of novae, naming them super-novae. It was later determined that these bright transient events were caused by the explosion of a star. With more observations of SNe, it was determined that there were several fundamental distinctions between SNe explosions as described below in Section 1.2.

The detection of SNe require finding an object that can be as bright as a galaxy for a short period of time. In order to find these events, image subtraction is crucial. In image subtraction, two images of the same section of sky taken at different periods of time are subtracted from each other and the locations where variation occurred are noted. During an SN explosion, the host galaxy light remains essentially constant except for the large increase at the location of the SN. Image subtraction reveals the location of the SN. As SNe are rare in any particular galaxy, using

a telescope with a large field of view is very important. In 1995, 11 SNe were discovered using a CCD imager and then spectroscopically-confirmed.

To efficiently observe SNe in distant galaxies, astronomers can no longer rely on the serendipitous detection of SNe. One technique for detecting SNe is to image a large region of sky every few days, observing many galaxies at a time. The images from different days from this rolling search technique can be subtracted and the appearance of a variable object will be detected. This technique has been used for many of the surveys in the early 21st century including the Sloan Digital Sky Survey (SDSS) SN Survey and the Supernova Legacy Survey (SNLS). Using the Hubble Space Telescope (HST), distant SNe have been observed through programs that imaged massive galaxy clusters on the order of every month and again found transients through image subtraction.

The spectroscopically-confirmed sample of SNe Ia are used for distance measurements in cosmology, using SNe Ia as standard candles, resulting in the first detection of an accelerating universe. The current and future rolling search surveys provide more candidate photometric SNe Ia than can be followed up with spectroscopic confirmation. Spectroscopic-confirmation provides a biased sample as brighter, more probable SN Ia candidates are targeted for spectroscopic follow-up. The ability to confirm the photometric SN Ia candidates without spectroscopy is needed to make full use of these large samples. The addition of the photometrically-confirmed SNe Ia expands the redshift coverage and increases the diversity of galaxies hosting SNe Ia. The host galaxy spectroscopic redshift can be used to reduce the number of free-parameters during the photometric classification. Large numbers of host galaxies can be quickly observed using multiobject spectrographs. This not only provides the redshift, but also allows for determination of spectroscopic host galaxy properties. These samples can then be used to find correlations between host galaxy property and SNe properties.

The photometric classification can be assessed using both a spectroscopically-confirmed subsample of SNe Ia and by comparing the photometrically-classified sample using redshift priors to the photometrically-classified sample found without redshift priors. The photometrically-classified sample with redshift can be used as a test bed for classification techniques. In Chapter 2, I describe the performance of the BOSS and SDSS spectrographs. In Chapter 3, I describe the process used to obtain spectra for host galaxies of SDSS-II SN candidates and determine updated photometric classifications using the host galaxy spectroscopic redshift. In Chapter 4, I compare the classification with and without redshift using different restrictions on data quality. In Chapter 5, I determine galaxy properties of the SNe host sample using both imaging and spectroscopy. I again compare the effect of redshift on the SNe sample using the SNe light curve properties in Chapter 6.

1.2 Supernova Astrophysics

In 1941, a sample of 14 SNe were used to determine that SN come in at least two types: Type I and Type II SN. Type I SN explosions have very homogeneous light curves and do not have hydrogen lines in their optical spectra while all Type II SN exhibit Balmer lines and exhibit a wide range of light curve profiles (Minkowski 1941; da Silva 1993). The modern scheme of SN classification still uses this definition of Type I and Type II classification. In addition, the Type I class is divided into three classes, Type Ia, Type Ib, and Type Ic, while the Type II SN are divided into Type II-P, Type II-L, Type II_n, and Type IIb subclassifications as described below in Section 1.2.2. Spectroscopic confirmation is used to distinguish between these classifications. A sample of four SN from the SDSS-II SN Survey is shown in Figure 1.1. It is also useful to classify SNe based on the explosion type: SNe Ia are the result of a thermal runaway in the core while all other SN explosions are the result of gravitational collapse of the core and are called core-collapse SNe.

A typical SN lasts for several months and can therefore have multiple nights of photometry. This time domain photometry can be used to generate the SN light curve. The optical light curves of each class of SN vary due to the cause of explosion and the transparency of the ejected material the light must travel through and will be described in more detail below.

1.2.1 SN Ia

In the 1960s, a subgroup of the Type I SNe, SNe Ia, were noticed to have very similar peak luminosities. This homogeneity allows normal SNe Ia to be used as standard candles for distance measurements to the host galaxy as described in detail in Section 1.3. SNe Ia occur in binary systems with at least one of the stars being a white dwarf.

1.2.1.1 White Dwarf Progenitor

A white dwarf is the final evolutionary state of low mass main sequence stars. A main sequence star fuses hydrogen atoms in the core into helium through the proton-proton chain shown in Equation 1.1.



Two protons fuse to create the unstable helium isotope ${}^2_2\text{He}$, which then decays into deuterium. One deuterium atom then fuses with a proton to create ${}^3_2\text{He}$. There are four paths to create ${}^4_2\text{He}$ from helium-3 known as the pp I, II, III, and IV branch, respectively. The star is in thermal equilibrium as the gravitational pressure of the star is balanced by the thermal pressure from the

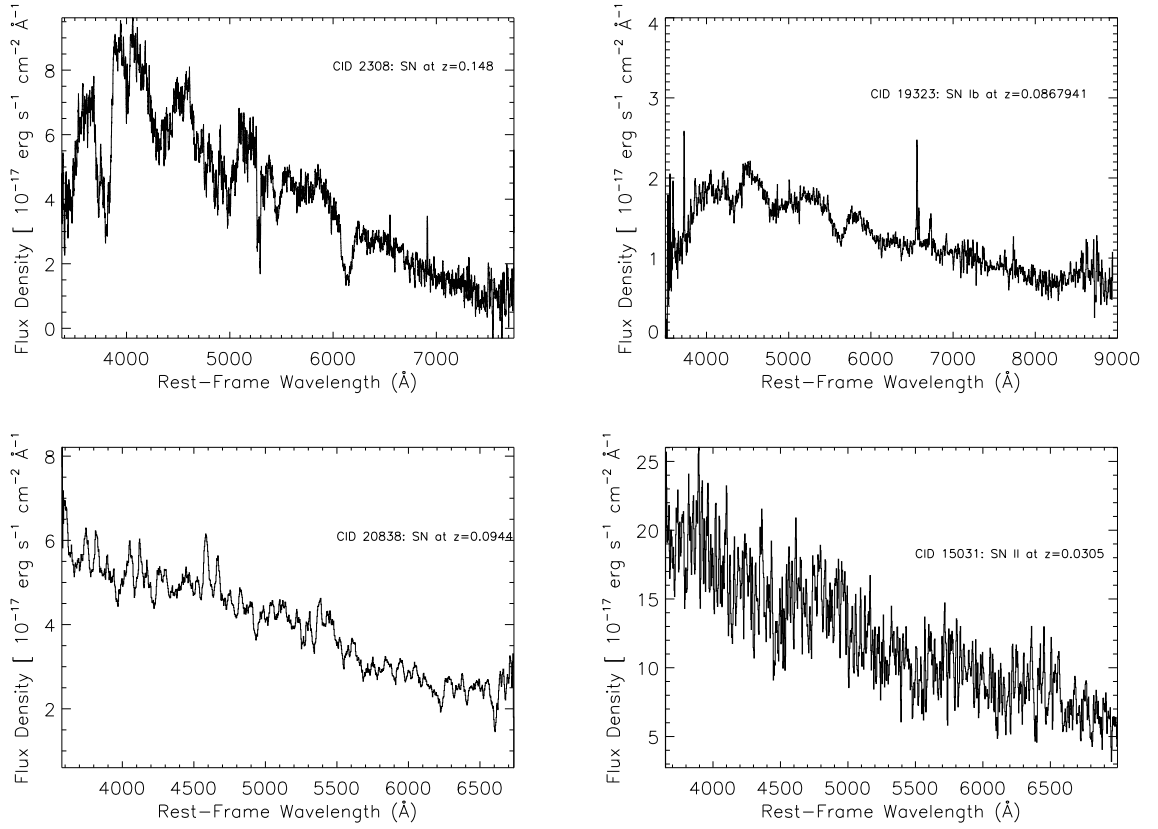
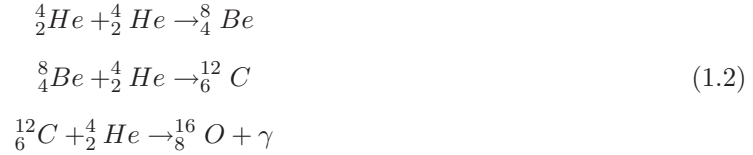


Figure 1.1 Example spectra of four different SN spectral classes observed in the SDSS-II SN Survey. Top Left: An SN Ia at $z = 0.148$. Top Right: An SN Ib at $z = 0.0868$. Bottom Left: An SN Ic at $z = 0.0944$. Bottom Right: An SN II at $z = 0.0305$.

nuclear fusion at the core. A main sequence star with $0.5M_{\odot} \leq M \leq 8M_{\odot}$ will evolve into a red giant star after the hydrogen fusion phase.

During the red giant phase, initially the core will shrink because the temperature is not hot enough for the helium in the core to fuse. This collapse will eventually cause helium fusion in the core when the core temperature reaches 10^8 K. The nuclear fusion of the helium in the core creates carbon and oxygen through the triple-alpha process shown in Equation 1.2. Two helium atoms first fuse together to form unstable beryllium. At these temperatures, the rate of fusion is greater than the decay rate of beryllium-8 so that some of the beryllium can fuse with helium to form stable carbon-12. Again by the alpha process, carbon-12 can fuse with a helium nucleus to form stable oxygen-16. This process creates a large amount of stable carbon and oxygen in the core of the red giant. For stars of mass $M \lesssim 8M_{\odot}$, the core does not reach the required temperature to fuse carbon, 10^9 K. The outer layers of the red giant will shed forming a planetary nebula and reveal a core of carbon and oxygen known as a carbon-oxygen white dwarf.



A white dwarf star is the final evolutionary state of stars that are not massive enough to become neutron stars. White dwarfs are very dense stellar objects, with masses on order of one solar mass and with radius on order of one earth radius. White dwarfs are no longer supported by the radiation pressure from fusion at the core; instead they are supported by electron degeneracy pressure. The Pauli exclusion principle does not allow fermions, in this case electrons, to occupy the same quantum state. There is a limit to the maximum mass of a star that can be supported by electron degeneracy pressure, the Chandrasekhar limit, which is about $1.44 M_{\odot}$ for a nonrotating white dwarf. If the Chandrasekhar mass is reached, a white dwarf will no longer be supported by the electron degeneracy pressure and will collapse, resulting in an SN Ia.

When the star collapses, the temperature increases to the point at which carbon fusion begins, creating a thermonuclear runaway and the elements in the core including carbon and oxygen burn into heavier elements in seconds. This creates $\sim 10^{44}$ J of energy which is enough kinetic energy to unbind the star. Matter is ejected to speeds of $\sim 0.06c$ and creates the extreme luminosity increase.

The light curves of SNe Ia are very homogeneous and have a consistent peak luminosity. The homogeneity results from each explosion having very similar initial conditions. After peak luminosity, the light curve is powered by the quick decay of nickel-56 into cobalt-56 ($t_{1/2} = 6.1$ days) and then the longer decay of cobalt-56 into stable iron-56 ($t_{1/2} = 77$ days).

The exact mass accretion mechanism for reaching the Chandrasekhar mass is not known. The two favored models require a binary system and transfer of mass that results in an SN Ia, the single-degenerate and the double-degenerate scenarios.

1.2.1.2 Single-Degenerate Scenario

In the single-degenerate scenario, the binary system consists of a white dwarf and a companion star, likely a red giant, but possibly a subgiant or main sequence star (Whelan & Iben 1973) as shown in Figure 1.2. If the white dwarf and the companion star are close enough, the white dwarf can accrete mass from the companion star, eventually reaching the Chandrasekhar mass. The companion star is expected to fill its Roche lobe, while the white dwarf is small compared to its Roche lobe. Material outside the Roche lobe of the companion star is not gravitationally bound to the companion star and the tidal forces on this material from the white dwarf cause mass transfer onto the white dwarf due to Roche-lobe overflow. A search for the companion star of SN 1006, combined with other results, find an upper limit of 20% of SNe Ia resulting from the single-degenerate scenario (González Hernández et al. 2012).

1.2.1.3 Double-Degenerate Scenario

The other scenario in creating an SN Ia is the merger of two white dwarfs. If the combined mass of the white dwarfs is greater than the Chandrasekhar mass and the two stars merge, they will create a super-Chandrasekhar mass white dwarf. It has been found that in the Milky Way,

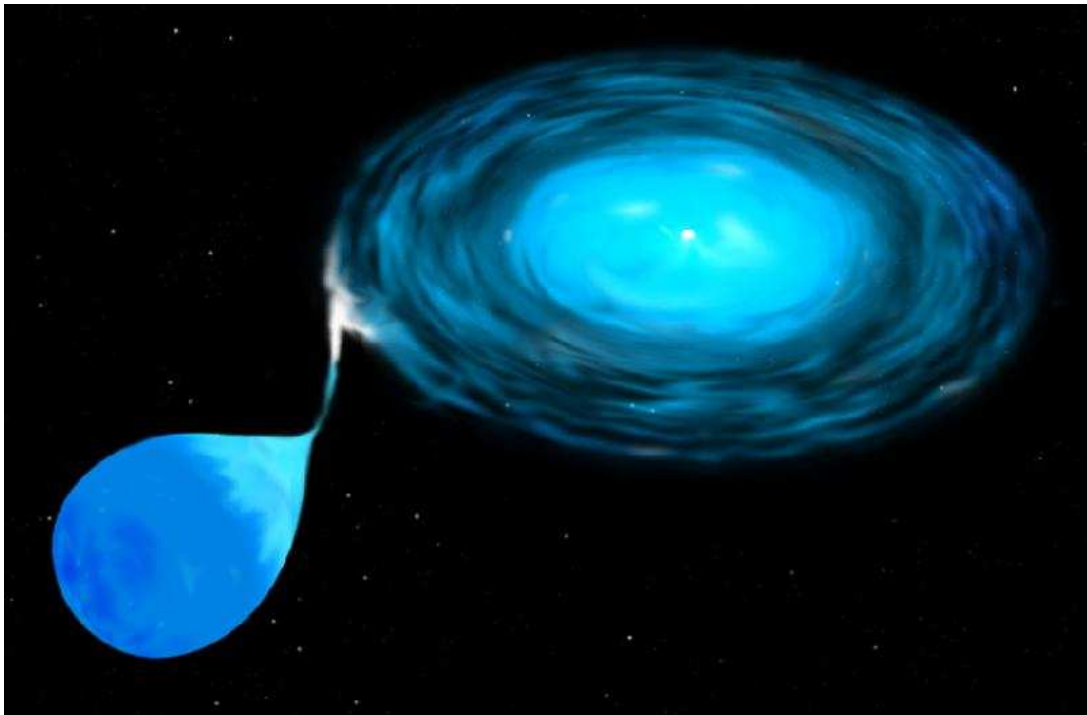


Figure 1.2 An artists rendition of a binary system consisting of a white dwarf star and a companion star. The stars are close enough together that the white dwarf is accreting mass from the companion star. Credit: STScI (via <http://hubblesite.org/newscenter/archive/releases/1995/23/>)

solitary stars rarely collide. In order to achieve the high rate needed to match the observations of SNe, collisions in very dense regions like the core of globular clusters can create binary star systems consisting of two white dwarfs. Analysis of 4000 white dwarfs in the Sloan Digital Sky Survey (SDSS) found 15 double-degenerate systems and through Monte Carlo simulations found a rate of one white dwarf merger per century in the Milky Way, matching the rate found in similar galaxies (Badenes & Maoz 2012).

1.2.2 Core-Collapse SN

When massive stars are at the end of their evolutionary tract, nuclear fusion can no longer support the core against the gravitational pressure and they undergo core-collapse. Unlike the less massive stars described in Section 1.2.1.1, stars of mass $10M_{\odot} \leq M \leq 140M_{\odot}$ are at high enough temperature to continue nuclear fusion of carbon which lasts for $\sim 10^3$ years. In addition, they can fuse the additional elements resulting from this fusion, neon (3 years), oxygen (0.3 years), and silicon (5 days). The silicon creates unstable nickel which decays into iron at the core. Because not all of each generation of element is fused in the core, the star has layers of different elements, shown in Figure 1.3, with the lighter elements near the surface and the heavier elements near the core. The hydrogen shell does not exist for certain scenarios as described in Section 1.2.2.1 and Section 1.2.2.2. Iron-56 has the second highest binding energy per nucleon and will require energy for additional fusion. The isotope with the highest binding energy per nucleon, nickel-62, is not a favored process in the conditions present in the stellar core. Fusion is no longer taking place in the core, and the core begins to collapse when the electron degeneracy pressure can no longer support the core when iron in the core reaches the Chandrasekhar limit, $1.44M_{\odot}$. The gravitational collapse can occur with speeds of up to $0.23c$, causing massive temperature and density increases. The initial conditions of the star prior to collapse, primarily mass and metallicity, are important factors on the nature of the explosion and the remnant of the star as summarized in Table 1.1 (Heger et al. 2003).

There are additional scenarios of core-collapse SN including electron capture for stars with $8M_{\odot} \leq M \leq 10M_{\odot}$, pair instability for stars with $140M_{\odot} \leq M \leq 250M_{\odot}$, and possibly photo-disintegration for the most massive stars in the early universe, $M \geq 250M_{\odot}$.

1.2.2.1 SN Ib/Ic

There are two additional classifications of Type-I SNe as a result of core-collapse, Type-Ib (SN Ib) and Type-Ic (SN Ic). Like SNe Ia, SNe Ib and SNe Ic do not have hydrogen emission lines in their spectra. This is because the massive progenitor star has lost most of the hydrogen layer either through stellar winds or interaction with a companion star. SN Ib are the more common of the two core-collapse Type-I SNe and occur in stars that have helium layers. There is a range of

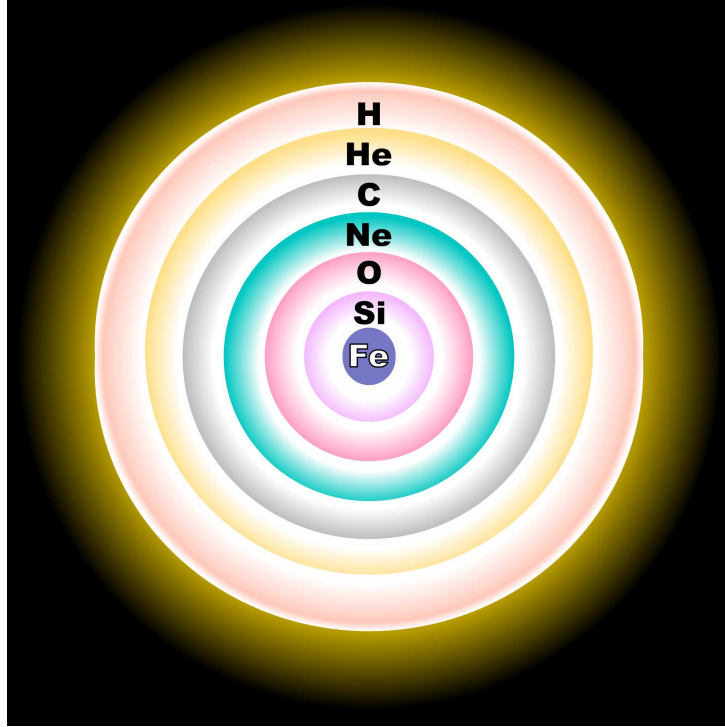


Figure 1.3 A cross-section of an evolved, massive star ($M > 8M_{\odot}$) before core has begun to collapse. Credit: Public Domain, (via Wikimedia Commons http://en.wikipedia.org/wiki/File:Evolved_star_fusion_shells.svg, User:Rursus)

Table 1.1. Types of Iron Core-Collapse SN

Mass (M_{\odot})	SN Type	Remnant
10-25	II-P (Faint)	Neutron Star
25-40 (low metallicity)	II-P (Normal)	Neutron Star \rightarrow Black Hole
25-40 (high metallicity)	II-L or II-b	Neutron Star
40-90 (low metallicity)	None	Black Hole
40-140 (near solar metallicity)	Ib/c (Faint); GRB and Hypernova	Neutron Star \rightarrow Black Hole
40-140 (high metallicity)	Ib/c	Neutron Star
90-140 (low metallicity)	None, possible GRB	Black Hole

metallicity and masses that can evolve where there is also little helium in the layers of the star and these create SNe-Ic explosions. The light curves of SNe-Ib and SNe-Ic are very similar in shape to SNe Ia and are powered by the same radioactive decay process, but have a lower peak luminosity. The peak luminosity can vary by orders of magnitude.

Since the light curve shape of SN Ib and SN Ic are very similar to that of an SN Ia, but the peak luminosities vary significantly, they are a source of contamination in cosmology where SNe Ia are used as standard candles.

1.2.2.2 SN II

A Type-II SN occurs for stars with mass $8M_{\odot} \leq M \leq 40M_{\odot}$. The progenitor stars still have the shell of hydrogen which is observed in the SNe spectra and distinguishes them from Type-I SNe. All SNe II show a similar rise in luminosity and then a similar decline that is much slower than SNe Ia. A few weeks after peak luminosity, the light curve shape of Type-II SNe can be divided into two classes, Type II-P SN (SNII-P) and Type II-L SN (SNII-L). SNII-L continue the linear decrease in luminosity while SNII-P have a luminosity plateau and then decrease. Figure 1.4 shows the light curve shape of the two different Type-II SN light curves. The linear decrease in SNII-L is caused by the conversion of cobalt-56 into iron-56. The plateau phase in SNII-P is caused by release of energy from the expanding envelope (Doggett & Branch 1985). After the plateau phase, the luminosity decreases and is again powered by the conversion of cobalt-56 into iron-56 and is the same shape as SNII-L. SNII-P are by far the most observed Type-II SNe and it is likely that SNII-L do not show the plateau phase only because their hydrogen envelope is much smaller.

There are additional Type II SNe, Type-IIb SN (SN IIb) and Type-IIIn SN (SN IIIn). An SN IIb initially has a weak hydrogen line, so it is classified as a Type-II SN, but at later times the hydrogen emission lines are undetectable and the spectrum looks like an SN Ib. An SN IIIn has very narrow hydrogen emission lines.

1.2.3 Light Curve Fitting

Once time domain photometry has been collected, the observed data are collected into SN candidate light curves. To compare SN, the light curves need to be flux calibrated and have the same rest-frame bands. K-corrections are used to transform data from one filter to a different filter. To measure the distance from an SN light curve, a model must be used that contains parameters for at least flux, decline rate, and SN color. One way to parameterize the decline rate of SNe Ia is by using Δm_{15} , which measures the difference in magnitude of the SN Ia 15 days after explosion compared to the peak magnitude. A small Δm_{15} is a brighter SN Ia. For SN Ia light curves with many epochs near peak luminosity, a model is not needed because Δm_{15} can be determined by discrete template fitting as was performed when the Δm_{15} relation was discovered (Phillips

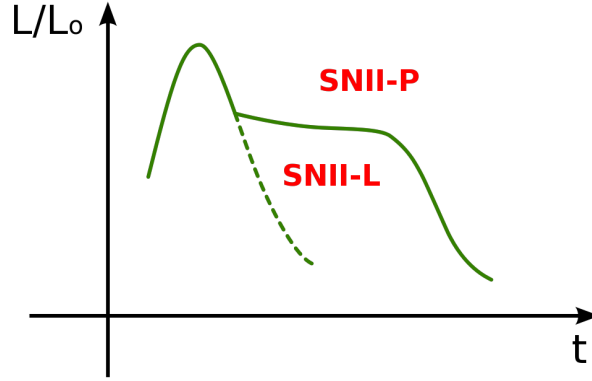


Figure 1.4 The light curve shapes of SNII-P and SNII-L. The distinct plateau shape after peak is apparent in the SNII-P light curve. Credit:Public Domain, (via Wikimedia Commons <http://en.wikipedia.org/wiki/File:SNIIcurva.svg>, User:Paulsmith99)

1993). The light curve of each class of SN has a distinct shape as described in Section 1.2.1.1 and Section 1.2.2. There are several methods used to parametrize SN light curves; two of the more common methods will be described below.

1.2.3.1 SALT2

SALT uses spectral energy distributions (SEDs) at different SN epochs to model SN light curves (Guy et al. 2005). The variability in light curve width is modeled with a stretch parameter. Color variability is modeled as an extinction factor that multiplies the flux. K-corrections are absorbed into the model. The SALT parameters are peak B-band magnitude, a stretch factor, and c , B-V at maximum. Importantly, SALT does not give a distance measurement.

SALT2 updates the SALT models. SALT2 provides an empirical model of the evolution of SNe Ia using both observed light curves and spectra (Guy et al. 2007). The SALT2 model covers the wavelength range 2500-8000Å and again has three parameters: x_1 which is very similar to stretch, a color parameter c , and the time of peak luminosity. The flux can be written as $F(SN, t, \lambda) = x_0 \times [M_0(t, \lambda) + x_1 M_1(t, \lambda) + \dots] \times \exp[c CL(\lambda)]$ where t is the rest-frame time since peak luminosity in B-band, and λ is rest-frame wavelength. The M_i functions describe the average spectral sequence for $i = 0$ and additional components for SNe Ia variability for $i > 0$. x_0 is the SED normalization and x_i are parameters for each SN, x_1 corresponds to stretch. $CL(\lambda)$ is the average color correction law and c is the color offset at peak luminosity. The parameters x_i and c are specific to each SN while M_i and CL are properties of the model and the same for all SNe.

1.2.3.2 MLCS2k2

The Multi Light Curve Shape 2k2 (MLCS2k2) method is used to measure distances to SNe Ia. MLCS2k2 uses K-correction, extinction corrections, and was trained using 100 events and has rest-frame wavelength coverage from 3200-9000Å (Jha et al. 2007). Unlike other models, MLCS2k2 imposes the brighter-slower and brighter-bluer relations. It can also assume an extinction prior. This prior provides a statistical separation of supernova and dust color variations. With a sample of 133 Nearby SNe Ia, MLCS2k2 found an intrinsic dispersion in distance less than 7%.

1.3 SN Cosmology

In 1929 Hubble determined a linear relation between the distance of nearby galaxies and their recessional velocities (Hubble 1929). This was evidence of an expanding universe. Redshift, z , is now used instead of recessional velocity, where redshift is the fractional wavelength change, $z = \lambda_{\text{observed}}/\lambda_{\text{rest}} - 1$. To measure the relation between redshift and distance, it is necessary to have accurate distance measurements for both nearby and distance objects. The homogeneous nature of the peak luminosity of SNe Ia makes them standard candles and very useful for measuring distant objects. The expansion of the universe was determined to be accelerating in the late 1990s using measurements of ~ 50 SNe Ia (Riess et al. 1998; Perlmutter et al. 1999) when the distant SNe Ia were fainter than expected when compared to the nearby SNe Ia.

1.3.1 Cosmology Review

The evolution of the universe is governed by Einstein's general relativity theory. A solution to the field equations of general relativity is the Friedman-Lemaitre-Robertson-Walker (FLRW) metric given in Equation 1.3,

$$ds^2 = dt^2 - a^2(t) \left(\frac{dr^2}{1 - kr^2} + r^2(d\theta^2 + \sin^2\theta d\phi^2) \right) \quad (1.3)$$

where $a(t)$ is the scale factor and k is the sign of the curvature and takes the values $-1, 0$, or 1 . This is known as the Standard Model of present day cosmology. In the FLRW metric, it is assumed that, at large scales, the universe is both isotropic and homogeneous in distribution of matter and radiation and that energy conservation is valid.

The Friedmann equations, shown in Equation 1.4 and Equation 1.5, model this homogeneous, isotropic universe, where $H = \frac{\dot{a}}{a}$ is the Hubble parameter. The scale factor, $a(t)$, is a dimensionless quantity that represents the relative expansion of the universe, relating the proper distance, $d(t)$ between two objects moving with the Hubble flow in an FLRW universe as $d(t) = a(t)d_0$. Unlike the proper distance which changes with time, a quantity called the comoving distance does not change in time by factoring out the expansion of the universe. In comoving coordinates, $ds^2 = dt^2$, as r, θ , and ϕ are constant in time.

$$H^2(z) = \left(\frac{\dot{a}}{a}\right)^2 = \frac{8\pi G}{3}\rho - \frac{k}{a^2(t)} + \frac{\Lambda}{3} \quad (1.4)$$

$$\frac{\ddot{a}}{a} = -\frac{4\pi G}{3}(\rho + 3p) + \frac{\Lambda}{3} \quad (1.5)$$

The shape of the universe is described as open, flat, or closed in reference to negative, zero, or positive curvature, respectively. In a closed universe, the total energy is negative in which case the universe will reach a maximum radius and then collapse. An open universe will continue to expand without limit. In a flat universe, the universe will also forever expand, but the velocity of expansion will approach zero. In addition, Euclidean geometry is valid in a flat universe. Observationally, if our universe is not flat, it is very close to flat based on cosmological measurements of the matter-energy density and spacetime intervals.

An important parameter in cosmology is the density parameter, $\Omega = \frac{\rho}{\rho_c}$, where the density ρ is compared to the critical density ρ_c of the Friedmann universe. In a flat universe, the total density is made of radiation, matter, and vacuum terms and is equal to the critical density. This means that $\rho = \rho_r + \rho_m + \rho_\Lambda \Rightarrow \Omega = \Omega_r + \Omega_m + \Omega_\Lambda$. With the addition of a curvature term, we have $\Omega + \Omega_k = \Omega_k + \Omega_r + \Omega_m + \Omega_\Lambda = 1$. At the current time, assuming a flat cosmology, $\Omega_M = 0.274$, and $\Omega_\Lambda = 0.726$ (White et al. 2011). However, the universe has not always been in this phase. In the next several paragraphs, we will look at stages in the universe when radiation, matter, and Λ were the dominant terms. The equation of state relates the pressure to the energy density of the universe, $w = \frac{p}{\rho}$ with $\rho \propto a^{-3(1+w)}$.

- **Radiation Dominated:** The universe began in a radiation-dominated era, the dynamics of the universe were initially determined by relativistically moving particles, primarily photons and neutrinos. During the radiation-dominated era, $p = \rho/3$ because the pressure is the energy density averaged over the three spacial dimensions. This means that $w = 1/3$ and $\rho \propto a^{-4}$. At this time, $a(t) \propto t^{1/2}$. This lasted for $\sim 50,000$ years, ($z \sim 3600$), when the universe became matter-dominated.

- **Matter Dominated:** The universe still remained optically thick until $z \sim 1100$ when the photons making up the cosmic microwave background radiation (CMB) were last scattered. During the matter-dominated era, ρ is dominated by the rest mass energy while the pressure is proportional to the nonrelativistic velocity so $w = 0$. For a matter-dominated universe, $\rho \propto a^{-3}$ and $a(t) \propto t^{2/3}$.

- **Λ Dominated:** At some point in time, a universe that is matter-dominated should stop expanding and begin to contract under the influence of gravity. However, the discovery of an accelerating universe requires a new source of energy to overcome the gravitational attraction. Einstein introduced a cosmological constant, Λ , in general relativity to create a static universe. Λ represents the energy density of the vacuum of space. When Hubble discovered the expansion of the universe, Einstein abandoned the cosmological constant. With the discovery of acceleration of the universe, the cosmological constant can again be used and is consistent with current observations of dark energy. The dark energy-dominated era began when the cosmological constant term Λ

began to dominate the energy density of the universe. At this stage, in Λ CDM, $p = -\rho$, $w = -1$, and $a(t) \propto e^{\sqrt{\frac{\Lambda}{3}}t}$. However, we do not know the true nature of dark energy and often introduce additional degrees of freedom to describe dark energy. In other models, we allow $w \neq -1$ as a test on the cosmological constant, w CDM, a constant equation-of-state parameter in a flat universe.

1.3.1.1 Luminosity Distance

While the comoving distance is very useful, it is not an observable. The luminosity distance is a measurement between the absolute magnitude, M , and apparent magnitude, m , of an object, $D_L = 10^{\frac{m-M}{5}+1}$. The luminosity distance can also be derived from an objects flux and luminosity as in Equation 1.6. To relate the luminosity and comoving distances, the relationship $D_L = (1+z)D_{comoving}$ is used.

$$F = \frac{L}{4\pi D_L^2} \quad (1.6)$$

$$D_L = \sqrt{\frac{L}{4\pi F}} \quad (1.7)$$

Another way to measure astronomical distances is the distance modulus, $\mu = m - M$. The distance modulus is related to a distance d measured in parsecs by the equation $\mu = 5\log_{10}(d) - 5$.

A Hubble diagram relates the distance to the redshift. The accelerated expansion of the universe was determined using sample of SNe Ia and will be described below. A current Hubble diagram is also described below.

1.3.2 Spectroscopic SN Ia

Historically, SNe Ia have been spectroscopically classified. This requires observing a spectrum when the SN is near peak luminosity. Early identification of possible SNe Ia candidates from imaging is essential to schedule spectroscopic confirmation.

1.3.2.1 1990s

CCD technology in the early 1990s allowed for precision supernova photometry. In 1996, the Calan-Tololo survey obtained photometry and accurate distances for 29 SNe Ia to $z \leq 0.10$ in several optical bands (Hamuy et al. 1996a,b). Two groups were measuring high redshift SNe and obtained a sample of redshifts and distances for ~ 50 SNe Ia to $z \leq 1$. When the high redshift data was analyzed along with the low redshift data, the high redshift SNe were too faint. This led to the conclusion that the expansion of the Universe must be accelerating (Riess et al. 1998; Perlmutter et al. 1999). This is not possible in a matter dominated universe and there must be some force behind this acceleration known as dark energy.

1.3.2.2 2000s

A number of surveys were performed in the first decade of the 21st century to increase both the sample size and the redshift coverage of the spectroscopically-confirmed SNe Ia. The Lick Observatory Supernova Search (LOSS; Filippenko et al. 2001; Ganeshalingam et al. 2010), the Carnegie Supernova Project (CSP; Hamuy et al. 2006), the Harvard-Smithsonian Center for Astrophysics SN group (CfA; Hicken et al. 2009), and the Palomar Transient Factory (PTF; Rau et al. 2009; Law et al. 2009) are each designed with an emphasis on discovery and observation of SNe at redshifts $z \lesssim 0.1$. Similarly, the second generation of the Sloan Digital Sky Survey (SDSS; York et al. 2000) featured a program to study SNe in the southern equatorial stripe (Stripe 82) in the intermediate redshift range $0.1 \lesssim z \lesssim 0.3$ (Frieman et al. 2008; Sako et al. 2008). The Supernova Legacy Survey (SNLS) (Astier et al. 2006; Guy et al. 2010; Conley et al. 2011; Sullivan et al. 2011), and the ESSENCE SN Survey (Miknaitis et al. 2007; Wood-Vasey et al. 2007) target the redshift range $0.3 \lesssim z \lesssim 1.0$ for SNe Ia. Finally, the highest redshift SNe currently used for cosmological constraints, those at $z \gtrsim 1$, are studied using the Hubble Space Telescope (HST) (Riess et al. 2004, 2007; Dawson et al. 2009; Suzuki et al. 2012).

1.3.2.3 2010s and Beyond

The best constraints on dark energy have been derived using a sample of 580 SNe Ia compiled from a number of different surveys. The Hubble diagram for the sample, known as Union2.1, is shown in Figure 1.5. $\Omega_\Lambda = 0.729^{+0.014}_{-0.014}$ for a flat Λ CDM universe (Suzuki et al. 2012). A flat w CDM universe results in the dark energy equation of state parameter $w = -1.013^{+0.068}_{-0.073}$. Figure 1.6 shows the constraints for $\Omega_\Lambda - \Omega_m$ and $w - \Omega_m$ using the SNe Ia sample combined with results from the cosmic microwave background (CMB) and baryon acoustic oscillations (BAO).

Current SN surveys, including the Dark Energy Survey (DES; The Dark Energy Survey Collaboration 2005), and future surveys, including the Large Synoptic Survey Telescope (LSST Science Collaborations et al. 2009), will generate deeper optical images and observe larger volumes of the universe than the current suite of surveys, resulting in hundreds to thousands of high-quality SN Ia light curves each year. A campaign to spectroscopically classify each candidate SNe will require an impractically large allocation of existing or new telescope time. These new surveys will instead require a change in the strategy of SNe observation, transitioning to a new phase in which SNe Ia are classified using only photometric light curves calibrated from a much smaller training set of spectroscopically-confirmed SNe Ia.

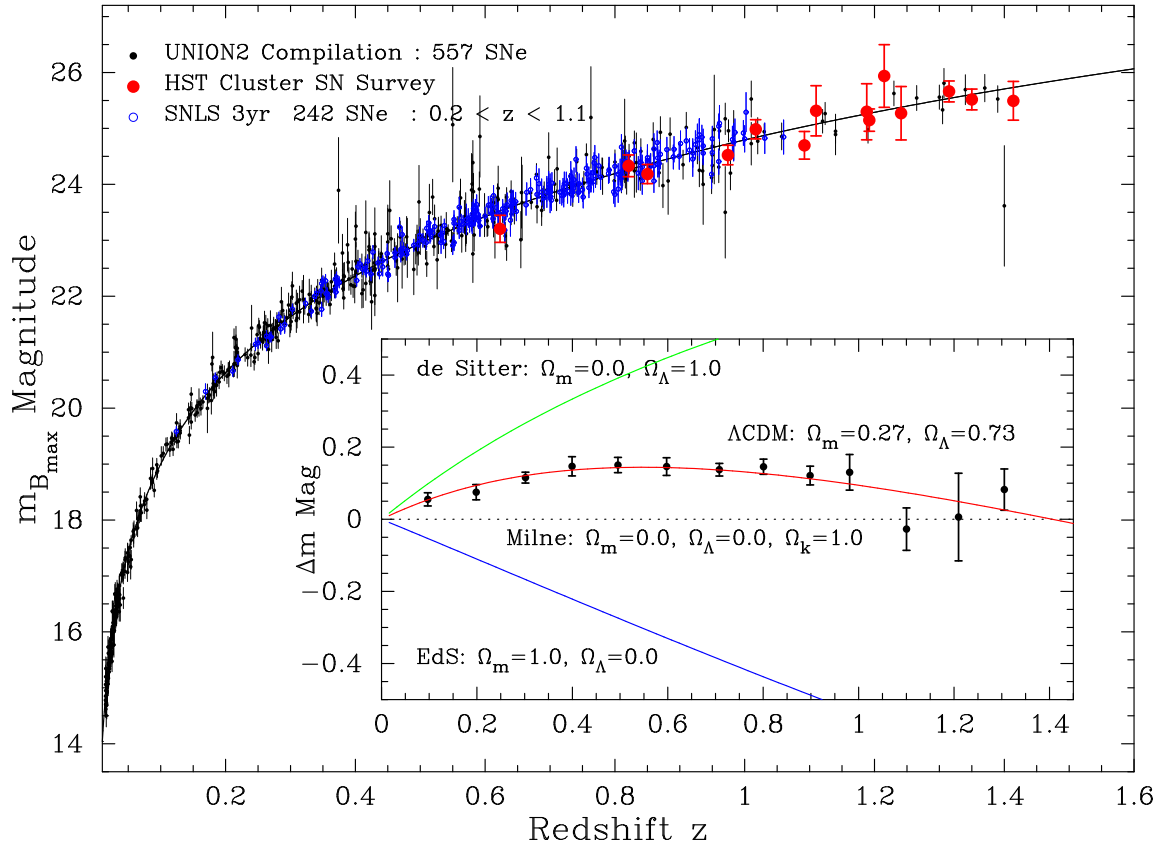


Figure 1.5 Hubble diagram with best fit cosmology for a flat Λ CDM universe using only supernovae. Credit: Figure 5 “The Hubble Space Telescope Cluster Supernova Survey: V. Improving the Dark Energy Constraints above $z > 1$ and Building an Early-Type-Hosted Supernova Sample,” Suzuki, N., et al. 2012, *Astrophys. J.*, 746, 85. Reproduced by permission of the AAS.

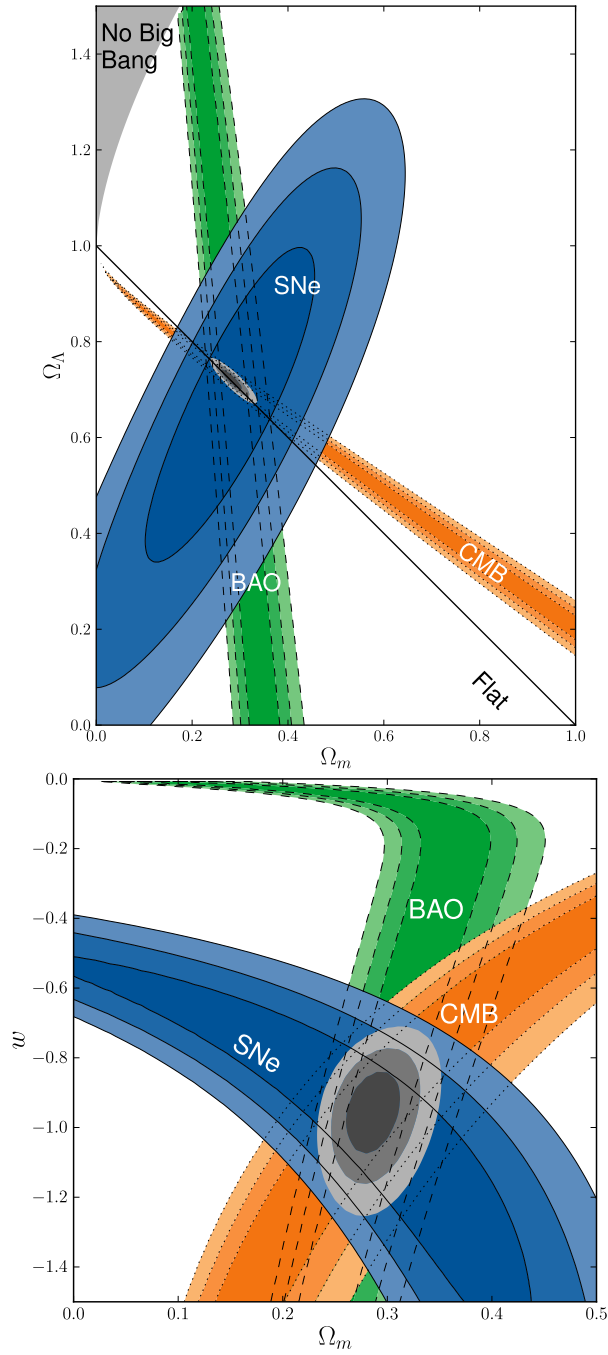


Figure 1.6 Λ CDM model and w CDM model with confidence regions. TOP: Λ CDM model with 68.3 %, 95.4%, and 99.7% confidence regions shown. In Λ CDM, $w = -1$. **BOTTOM:** In w CDM model, w is also a free parameter. Shown is the $\Omega_m - w$ plane with 68.3 %, 95.4%, and 99.7% confidence regions. Credit: Figure 6 “The Hubble Space Telescope Cluster Supernova Survey: V. Improving the Dark Energy Constraints above $z > 1$ and Building an Early-Type-Hosted Supernova Sample,” Suzuki, N., et al. 2012, *Astrophys. J.*, 746, 85. Reproduced by permission of the AAS.

1.3.3 Photometric SN Ia

The multiband light curve data from SN surveys has been used to photometrically type SNe candidates as well as determine redshift and luminosity distance. There have been a few initial studies of cosmology using SNe Ia with only photometry (Barris et al. 2004; Bernstein et al. 2012), and recent work has simulated the effect of using photometric redshifts and SN classifications on large samples of data (Kessler et al. 2010; Rodney & Tonry 2010).

The current generation of surveys, including the SDSS-II SN Survey and SNLS, photometrically-classified SN candidates. Many of these candidates do not have spectroscopic confirmation. For the SDSS-II SN Survey, 753 candidates were photometrically-classified as SNe Ia when their host galaxy spectroscopic redshift was used as prior in the light curve fit. A cosmological analysis was performed using only these photometrically-classified SNe Ia in Campbell et al. (2013) and they found similar results as spectroscopically-confirmed SNe Ia analysis.

1.3.4 Correlations Between SN Ia Properties and Host Galaxy Properties

Galaxies are separated into two categories, early-type and late-type, by the mean age of their stellar populations. Early-type galaxies have little star-formation and are mostly old, evolved stars. Early-type galaxies are generally big, red, elliptical, and passive. Late-type galaxies have ongoing star-formation and are small, blue, and spiral or irregular. Because core-collapse SNe are the end of stellar evolution for massive stars, and massive stars have much shorter lifetimes than less massive stars, core-collapse SN occur only in late-type galaxies. On the other hand, SNe Ia occur in both early-type and late-type galaxies.

The host galaxy type correlates with several SN Ia properties. The rate of SNe Ia is 10 times higher in star-forming galaxies than in passive galaxies (per unit mass). Early-type galaxies are the preferable environment for the fast declining SNe Ia. As fast declining SNe Ia are fainter, SNe Ia are brighter in spiral galaxies and the decline rate of SNe Ia decreases with redshift.

The SN surveys have increased the total sample size to ~ 1000 spectroscopically-confirmed SNe Ia. Across these redshifts, the sample size of SNe Ia has increased to the point where a careful treatment of systematic effects and uncertainties are an increasingly important part of the analysis of cosmological constraints. The systematic errors come from both instrumental effects and astrophysical effects. Examples of astrophysical effects include the correlation between SN Ia properties and host galaxy properties, appearing as a dependence of the rate of SN Ia events on stellar mass and star formation activity of the host galaxies (Sullivan et al. 2006), and the relationship between host-galaxy mass and SN absolute brightness (Gupta et al. 2011; Conley et al. 2011; Meyers et al. 2012).

In addition to constraints on cosmology, the spectroscopically and photometrically identified SNe Ia from the SDSS-II SN Survey have been used to probe SN Ia astrophysics. SN Ia rates to

$z \lesssim 0.3$ (Dilday et al. 2008, 2010b), rates in galaxy clusters (Dilday et al. 2010a), and SN Ia rate as a function of host galaxy property (Smith et al. 2012). Correlations between the metallicity and light curve shape and between the specific star formation rate and the Hubble residuals were found using a sample of spectroscopically-confirmed and photometrically-identified SNe Ia (D’Andrea et al. 2011). Gupta et al. (2011) explored the correlation between the Hubble residuals of 206 SNe Ia and the stellar mass and mass-weighted age of the host galaxies. Lampeitl et al. (2010) demonstrated a correlation between stellar mass and SN properties to high significance using spectroscopically-confirmed and photometric SNe Ia. A sample of nearly 200 spectroscopically-confirmed or photometrically-identified SNe Ia from the SDSS-II SN Survey were used to find relations between distance from the center of the host galaxy and SN properties (Galbany et al. 2012). A sample of spectroscopically-confirmed SNe Ia was used to measure correlations between SNe Ia properties and host galaxy properties including stellar velocity dispersion, age, metallicity, and element abundance ratios (Johansson et al. 2012).

CHAPTER 2

THE SDSS AND BOSS SPECTROGRAPHS

2.1 Introduction

The SDSS-I and the SDSS-II Legacy Survey covered $8,400 \text{ deg}^2$ in five optical bands and obtained spectra of more than 1.2 million objects: the data are described in the Seventh Data Release of the Sloan Digital Sky Survey (DR7; Abazajian et al. 2009). The 2.5 m Sloan Telescope (Gunn et al. 2006) is located at Apache Point Observatory and has a field of view of 7 deg^2 (3° diameter). The imaging survey was conducted using a large mosaic CCD camera (Gunn et al. 1998), leading to 230 million unique objects detected in *ugriz* (Fukugita et al. 1996) and repeated imaging of a 300 deg^2 leading to the SN light curves in the SDSS SN Survey (Frieman et al. 2008). The spectroscopic survey used two double spectrographs, each consisting of 320 optical fibers plugged into aluminum plates with a resolving power $R = \lambda/\text{FWHM} \sim 2000$ from the near ultraviolet to the near infrared (Smee et al. 2013). As mentioned in the introduction, 3,835 candidates from the SDSS SN Survey were hosted by galaxies that were already observed spectroscopically in SDSS before the commencement of the SN program.

SDSS-III (Eisenstein et al. 2011), which operates from 2008-2014, consists of four projects; the Baryon Oscillation Spectroscopic Survey (BOSS) is the extragalactic component designed for cosmology. BOSS will measure the BAO feature using a sample of 1.5 million galaxies (including 150,000 from SDSS-I/II) to $z < 0.7$ and Lyman- α forest absorption using more than 150,000 quasars at $2.15 < z < 3.5$ over $10,000 \text{ deg}^2$. The BOSS targets are more numerous and reach 1–2 magnitudes fainter than the SDSS spectroscopic targets; this improvement is possible due to upgrades to the spectrographs, an increase in the number of fibers from 640 to 1000 (Smee et al. 2013), and targeting quasars and luminous galaxies that are easier to identify from imaging data and spectroscopic confirmation. Here we will discuss the performance of the SDSS and BOSS spectrographs. The work on spectrograph design and predicted performance, summarized in Section 2.2, was performed by Robert Barkhouser and Stephen Smee. I worked on describing the performance of the spectrographs as detailed in Section 2.3.

¹The results reported in this chapter appear in the *Astronomical Journal*. Olmstead is a first-tier author in the refereed publication: “The Multi-object, Fiber-fed Spectrographs for the Sloan Digital Sky Survey and the Baryon Oscillation Spectroscopic Survey”, Smee, S. et al., 2013, *AJ*, 146, 32. Reproduced by permission of the AAS.

2.2 SDSS and BOSS Spectrograph Design and Predicted Optical Performance

The requirements for the SDSS spectrographs were set by its primary scientific goal: the creation of a three-dimensional wide-area map of the universe to reveal its large-scale structure, while the upgrades for the BOSS spectrographs were set by the primary goal of mapping the baryon acoustic peak to $z = 0.7$ and developing a new technique to detect large scale structure in the spectra of distant quasars through the Lyman- α forest.

2.2.1 Resolving Power

To meet the SDSS requirement of obtaining spectroscopic redshifts of galaxies to within 100 to 200 km/s, the resolving power, $\lambda/\delta\lambda$, where $\delta\lambda$ is taken to be the spectral FWHM of the fiber image on the detector in Å, was chosen to be between 1500-3000. This balances the wavelength range, number of photons per pixel per exposure, and the necessity of being able to resolve the absorption lines. The BOSS requirement was chosen to have a resolving power of at least 1400 in the wavelength range $3800 < \lambda < 4900$ Å to fit the Balmer features in calibration stars and to be at least 1000 for the remainder of the wavelength coverage for RMS redshift error of 300 km/s.

The predicted spectral resolving power, was analyzed using the computer program Zemax. A circular source equivalent to a fiber was placed at the location of the slithead and light rays were traced and measured by a simulated detector. The resulting image data was analyzed to determine the FWHM, which is then considered to be the resolution. The predicted resolving power for SDSS and BOSS is plotted in Figure 2.1.

We also present a two-dimensional contour image, Figure 2.2, of the BOSS CCDs showing the RMS width σ_p of the line-spread function in native pixels to demonstrate the predicted variation in resolution over the focal plane. The $\text{FWHM} = 2.35 \times \sigma_p$. Note that the linewidths are moderately degraded at the shortest wavelengths of the blue channel near the ends of the slit.

2.2.2 Throughput and Signal to Noise Ratio

The requirement on SDSS throughput was set by the desire to obtain 1 million spectra over $10,000 \text{ deg}^2$ to a limiting magnitude of $r = 18.15$ in five years, corresponding to roughly 100 deg^{-2} galaxies and average exposure time of one hour per plate. To determine accurate redshifts for the SDSS sample, it was determined that spectra with S/N of at least 15 per Å were required. The corresponding throughput requirement, including atmospheric extinction and the telescope throughput, varies as a function of wavelength; the maximum requirement is about 17% at 7000 Å, with requirements of roughly 10%, 15%, and 10% at 4000 Å, 6000 Å, and 8000 Å, respectively. It was determined from fainter galaxies in SDSS that redshifts can be determined with $\text{S/N} > 3 - 4$ per Å for the faintest galaxies. For BOSS to obtain redshifts for over 1,350,000 luminous galaxies

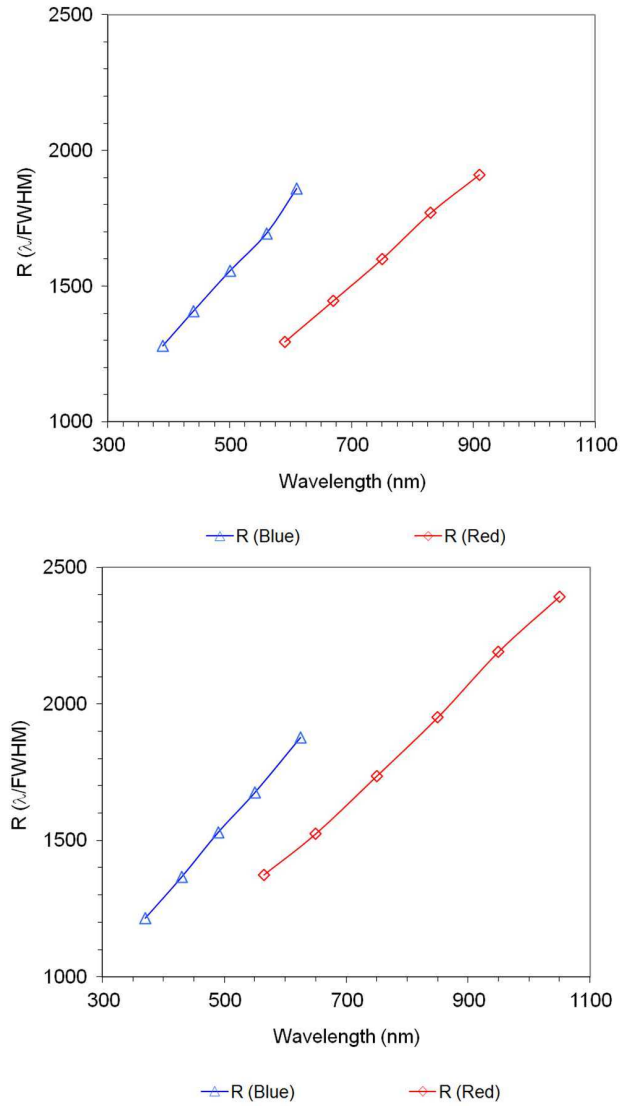


Figure 2.1 Predicted resolving power, R , as a function of wavelength for the SDSS and BOSS spectrographs. Predictions are derived from the FWHM of simulated, uncollapsed images computed using Zemax. In reality, the resolving power of the instrument is determined using collapsed spectra, so the prediction here is on the low side. However, the Zemax analysis assumes perfect optics and alignment. For this reason the predictions have been based on uncollapsed spectra, which is the conservative approach. The expectation is that the actual resolving power will be somewhat better than shown here. Top: Predicted resolving power for SDSS. Bottom: Predicted resolving power for BOSS.

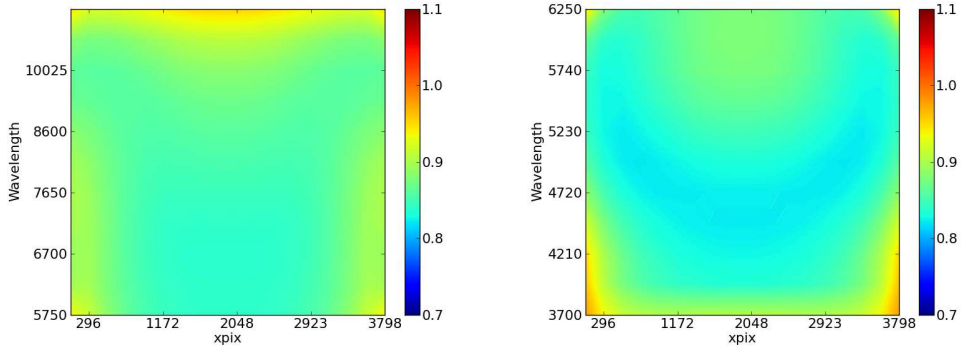


Figure 2.2 Contour image of the BOSS CCDs showing the RMS width σ_p of the line-spread function in native pixels to demonstrate the predicted variation in resolution over the focal plane. The $\text{FWHM} = 2.35 \times \sigma_p$; red CCD (left) and the blue CCD (right). The wavelength decreases from top to bottom.

in five years with similar exposure times, it was determined that the peak throughput would need to improve by a factor of two.

The total throughput, on-sky, for the SDSS and BOSS spectrographs was predicted from an end-to-end component model as a function of wavelength. Included in the model were: atmospheric extinction, seeing (slit) losses, telescope, fibers, collimator, dichroic, grism, camera, and CCD. Figure 2.3 shows the individual component efficiencies used for this model along with the total expected throughput. Peak efficiencies in the blue and red channels are 17% and 22%, respectively.

2.2.3 Flexure

As the telescope tracks the sky, the direction of the gravitational vector changes with respect to the spectrographs. This causes motion of the spectra on the detector during an exposure which can degrade resolution. A goal was set to limit flexure to 0.3 pixels in one hour, or 15° on the sky. The 0.3 pixels translates to, roughly, 0.3 Å in the blue camera, or roughly 20 km/s in redshift. Since galaxy internal velocity dispersions are on the order of 200 km/s, a galaxy absorption line would be three or four Å wide and just resolvable by the spectrograph. Therefore, flexing 0.3 pixels would just barely be detectable in a single galaxy absorption line. Details on flexure performance can be found in Section 2.3.3.

2.2.4 BOSS Detector Read Noise and Dark Current

To maintain Poisson-limited statistics in the $z = 2.2$ region of the Lyman- α forest, the BOSS blue channel detector must have a read noise less than $3.0 e^-/\text{pixel}$ RMS. The requirement for the red channel is less stringent because the spectra are sky-dominated for most of the red channel

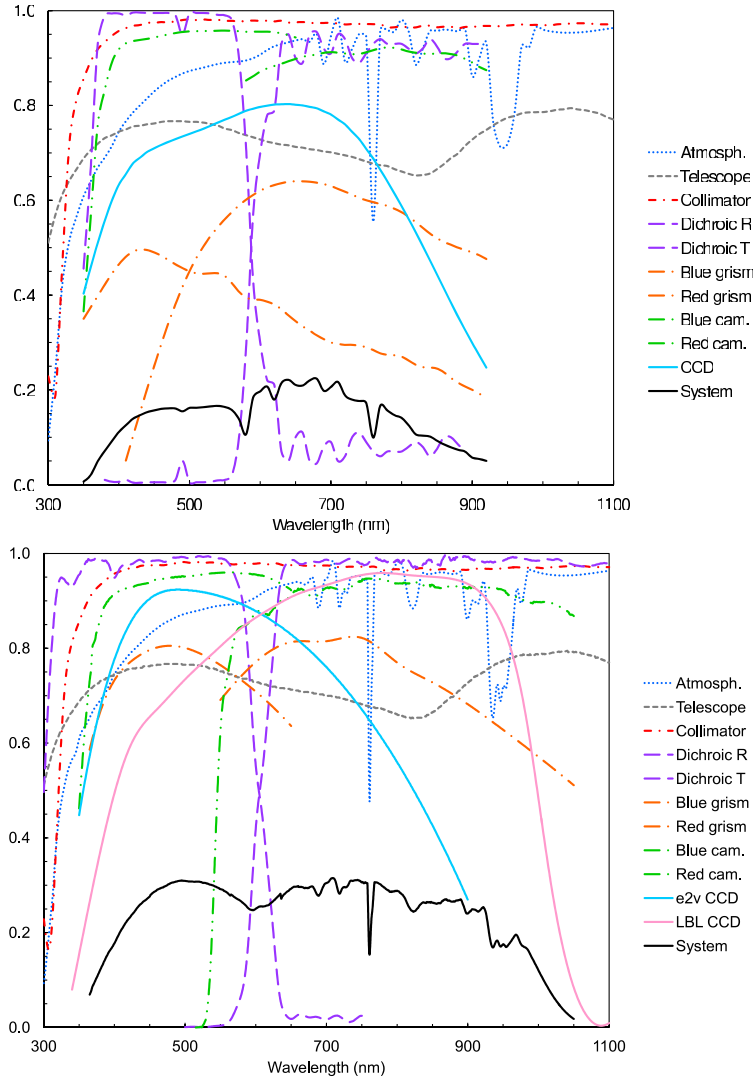


Figure 2.3 Expected throughput for the SDSS and BOSS spectrographs. The plot shows all contributors to the throughput model having a wavelength dependence. Not shown are those contributors with an essentially flat response across the bandpass: fiber transmission including Fresnel losses at the two faces (0.85), focal ratio degradation overfilling the collimator stop (0.97), and “slit” losses for 1'' FWHM seeing conditions modeled with a double Gaussian PSF (0.94). Not included in the model are losses due to centering and guiding errors. Top: Overall system throughput for SDSS, shown by the solid black curve, is expected to peak at about 17% in the blue channel and 22% in the red channel. Bottom: Overall system throughput for BOSS, shown by the solid black curve, is expected to peak at about 31% in both the blue and red channels, a significant gain over the original SDSS spectrographs.

wavelength range. The read noise for the red detector is required to be less than $5.0\ e^-/\text{pixel}$ RMS. To prevent significant noise contributions during an integration, a dark current that is less than $1.0\ e^-$ for the blue CCDs and less than $2.0\ e^-$ for the red CCDs during a 15 minute exposure is required. All of these requirements for detector performance were enabled by improvements in CCD technology.

2.3 SDSS and BOSS Spectrograph Performance

Here we describe the methods for determining the instrument performance for SDSS and BOSS in relation to the predictions summarized in Section 2.1. A summary of the design predictions and measured performance is presented in Table 2.1. Instrument characterization is presented in three parts: the spectroscopic pipeline, the spectrograph performance, and CCD performance. Data found in DR8 (Aihara et al. 2011) are used in the characterization of the SDSS spectrograph and data in DR9 (Ahn et al. 2012) are used in the characterization of BOSS.

2.3.1 Spectroscopic Pipeline

The spectroscopic redshifts and classification for SDSS and BOSS are based on the data reduction pipeline **idlspec2d**. A brief explanation of the routines for SDSS is found in Adelman-McCarthy et al. (2008) and Aihara et al. (2011). SDSS data were processed using **idlspec2d v5.3.12**, which is the same version of the software used in DR8. The pipeline was modified for BOSS to account for the increase in wavelength coverage, number of fibers, and other changes discussed in Section 2.2. For a brief description of the BOSS software reductions, see Dawson et al. (2013) and for a full description of the automated classification, see Bolton et al. (2012). BOSS data were processed using **v5.4.31**, a somewhat earlier version of the **v5.4.45** software used for DR9 (Ahn et al. 2012). There are minor changes between these two versions, but the differences do not change the conclusions of the work presented here. The intermediate data products produced by the **idlspec2d** pipeline are used to characterize the instrument performance; we include a brief explanation of the relevant functions here.

SDSS and BOSS observations of each plate follow the sequence: mount cartridge, slew to field, focus spectrograph, take exposure with calibration arc lamps and flat field lamps, and obtain a series of 15 minute science exposures. In the first step of the data reduction, the read noise and bias level from the raw images are determined from the overscan of the image. Next, raw images are bias-subtracted and counts are converted into electrons using CCD amplifier gains specific to each quadrant of each detector. Cosmic rays are then identified using a filter to discriminate between the sharp edges of cosmic ray trails and the smoother profile of optical sources. The noise of each

²Current and development versions of the software are found at <http://www.sdss3.org/dr9/software/products.php>

Table 2.1 Design Predictions and Measured Performance for SDSS and BOSS

Quantity	(SDSS)		(BOSS)	
	Design	Measured	Design	Measured
Spectrograph 1				
Wavelength Range	3900–9100	3800–9220 Å	3560–10,400	3560–10,400 Å
Resolving Power ($\lambda < 3800$ Å)	N/A	N/A	1000	1220–1480
Resolving Power ($3800 < \lambda < 4900$ Å)	1500	1500–1900	1400	1200–1900
Resolving Power ($\lambda > 4900$ Å)	1500	1900–2600	1000	1550–2550
Total Throughput (4000 Å)	0.11	0.08	0.18	0.15
Total Throughput (6000 Å)	0.20	0.17	0.25	0.21
Total Throughput (8000 Å)	0.14	0.13	0.29	0.25
Total Throughput (10,000 Å)	N/A	N/A	0.12	0.10
Flexure: Blue Channel	0.3	0.33	0.5	0.40
Spectral (pixels per 15° on the sky)				
Flexure: Blue Channel	0.3	0.18	0.5	0.11
Spatial (pixels per 15° on the sky)				
Flexure: Red Channel	0.3	0.30	0.5	0.41
Spectral (pixels per 15° on the sky)				
Flexure: Red Channel	0.3	0.21	0.5	0.18
Spatial (pixels per 15° on the sky)				
Spectrograph 2				
Wavelength Range	3900–9100	3800–9220 Å	3560–10,400	3560–10,400 Å
Resolving Power ($\lambda < 3800$ Å)	N/A	N/A	1000	1300
Resolving Power ($3800 < \lambda < 4900$ Å)	1000	1700–2200	1400	1350–1950
Resolving Power ($\lambda > 4900$ Å)	1000	1850–2650	1000	1700–2600
Total Throughput (4000 Å)	0.11	0.09	0.18	0.14
Total Throughput (6000 Å)	0.20	0.18	0.25	0.24
Total Throughput (8000 Å)	0.14	0.12	0.29	0.25
Total Throughput (10,000 Å)	N/A	N/A	0.12	0.10
Flexure: Blue Channel	0.3	0.30	0.5	0.43
Spectral (pixels per 15° on the sky)				
Flexure: Blue Channel	0.3	0.31	0.5	0.07
Spatial (pixels per 15° on the sky)				
Flexure: Red Channel	0.3	0.27	0.5	0.44
Spectral (pixels per 15° on the sky)				
Flexure: Red Channel	0.3	0.25	0.5	0.15
Spatial (pixels per 15° on the sky)				

pixel is determined by taking the Poisson noise from the electron counts in quadrature with the measured read noise. Finally, a flat-field image is used to correct the pixel-to-pixel response in the CCD.

Each fiber projects a spectrum onto the CCD with an RMS in the spatial direction of roughly one pixel and a spectral dispersion of roughly one pixel RMS in the direction of the parallel clocking. The data from the flat field exposures are used to model the profile of each fiber on the CCD and also to normalize fiber-to-fiber throughput variations. The data from the arc exposures are used to determine the wavelength solution for each fiber.

Figure 2.4 shows an example of the arc lines obtained in a BOSS exposure. The top left panel is taken near the edge of the blue CCD and shows a slight tilt in the wavelength direction due to optical distortion. This image also demonstrates the bundling of 20 fibers separated by a gap on either side. The top right panel demonstrates a dropped fiber near the right edge of the first bundle. The bottom left image from a red camera is taken near the center of the CCD and shows the amplifier gain between two quadrants at a different background count. The lower right panel shows several cosmic rays interacting with the CCD on a red camera. The bottom right image also shows an offset in the wavelength direction between the central bundle and the surrounding bundles due to imperfections in the slithead assembly. The top two images are more representative of the SDSS CCDs because the red BOSS CCDs are much thicker and lead to more pronounced cosmic ray trails. We use the wavelength solution and line spread function derived from the arc exposures to determine wavelength coverage and resolution.

Each two-dimensional science image is collapsed into a series of one-dimensional spectra using the fitted profile and wavelength solution from the calibration exposures for each fiber. At this point, the “SKY” fibers (fibers assigned to areas with no detected objects) are used to model the background as a function of position on the detector. The model sky background is subtracted from the one-dimensional spectra. These one-dimensional spectra contain all of the information

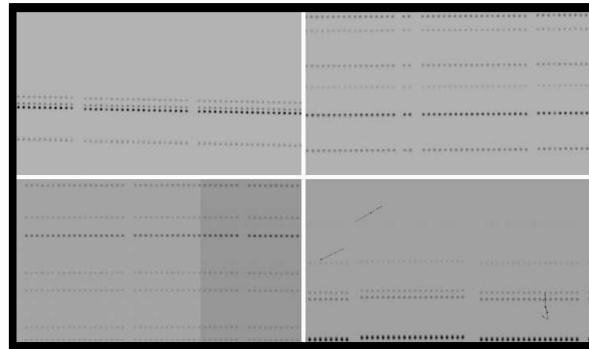


Figure 2.4 Raw arc image taken with the BOSS spectrograph. Top Left: 3650 – 3850 Å on blue CCD; Top Right: 5050 – 5250 Å on blue CCD; Bottom Left: 6000 – 6250 Å on red CCD; Bottom Right: 8850 – 9100 Å on red CCD. Each panel covers roughly 50 spectra.

required to characterize the instrument performance. For science applications, the spectrum from each fiber is resampled to a pixel size of 69 km/s and combined with the spectra from the same fiber for each exposure in the sequence to generate a high signal-to-noise spectrum. Redshifts and object classification are determined from these co-added spectra as is described in Bolton et al. (2012).

The data reduction pipeline also compensates for spectral shifts due to mechanical flexure. Shifts between exposures in the spatial direction are compensated by iteratively recentering the traces of all fibers starting from the positions determined from flat-field exposures, and adopting the median spatial shift as a global value for each exposure. For this process to converge properly, the accumulated spatial shift between flat and science frames must be significantly less than one-half the typical fiber-to-fiber spatial separation, a condition that is satisfied for any reasonable number of science exposures in sequence. Shifts between exposures in the spectral direction are compensated by measuring the positions of known bright sky emission lines and fitting a shift-plus-scale for each fiber and each exposure relative to the wavelength solution determined from arc-lamp calibration frames. The ultimate validation of the combined hardware–software system for flexure control is the $\sim 1\%$ level of systematic residual errors in near-infrared sky subtraction achieved for BOSS (Bolton et al. 2012).

2.3.2 Spectrograph Performance

2.3.2.1 Wavelength Coverage

The SDSS spectrographs have excellent wavelength calibration between the Hg I arc line at 3901.87 Å and the Ne I arc line at 9148.67 Å. The BOSS spectrographs have excellent wavelength calibration between the Cd I arc line at 3610.51 Å and the Hg arc line at 10140 Å. In between these detected arc lines for SDSS (3902 Å – 9149 Å) and BOSS (3611 Å – 10140 Å), the wavelength solutions are typically accurate to 3 km/s. Beyond those wavelengths the solutions are extrapolated and the accuracy has not been evaluated.

Including the extrapolation beyond the prominent arc lines, the wavelength range included in data reductions for the SDSS spectrographs is 3800–9220 Å. This is slightly broader than the design wavelength range of 3900–9100 Å. The BOSS spectrographs have useful data in the 3560 to 10,400 Å wavelength range that are included in all data releases. Although the detectors see light beyond this wavelength range, it is discarded in the reductions since the throughput is very low and the longer wavelengths suffer from second-order light.

Both the SDSS and BOSS blue limits ensure the CaII H and K lines are detected at zero redshift. The BOSS blue limit provides extended coverage of the Lyman- α forest for quasars at $z > 2.2$. The BOSS red limit measures the Mg b 5175 Å and the Na D 5893 Å absorption features for galaxies redshifted to $z < 0.72$. The wavelength coverage for SDSS and BOSS leads to detection of at least

31 common astrophysical emission lines, as detailed in Table 5 of Bolton et al. (2012).

2.3.2.2 Spectral Resolution

The spectral resolution is measured from calibration arc images taken before each set of science exposures. The one-dimensional arc image is first masked to include only pixels within 12 pixels of the center of each arc line on each fiber. A Gaussian of width σ_λ is fit to each spectral profile using the 25 unmasked pixels. A fourth order Legendre polynomial model is fit to the derived σ_λ as a function of wavelength to model the dispersion over the full wavelength range. The resolving power for SDSS and BOSS is then formally defined as $R = \frac{\lambda}{2.35 \times \sigma_\lambda}$. The resolution is the FWHM of the Gaussian, $2.35 \times \sigma_\lambda$.

We measured the resolving power as a function of wavelength from a sample of 100 SDSS plates and 100 BOSS plates. For each plate and each camera, we computed the mean R as a function of wavelength. Figure 2.5 shows a comparison of the SDSS resolving power to that for BOSS.

The extended coverage at long wavelengths from the new BOSS CCDs is evident redward of 9200 Å, while the extended coverage at short wavelengths is more subtle, but also shown in the figure. The presence of a dichroic for SDSS and BOSS is also revealed near 6000 Å where the resolving power no longer increases monotonically with wavelength. The apparent transition around the dichroic is due to the fact that both the red and blue channels contribute to this region, each with different dispersive elements. In the regions where we count flux from both cameras, we simply determine the resolving power by a mean weighted by the relative throughput of the two cameras. The BOSS requirements and measured resolving power are presented in Figure 2.6.

For BOSS, the position of the fiber on the CCD impacts the resolution due to optical distortion over the larger detectors. The resolving power of the middle fiber is representative of $\sim 80\%$ of the BOSS fibers, 100% of the SDSS fibers, and clearly exceeds specifications at all wavelengths for the first spectrograph. However, the fibers near the edge of the first spectrograph have a resolving power that is degraded by up to 20–25% relative to the central fibers. Also shown in the figure, the two blue channels show quite different patterns of image quality, with most fibers in the second spectrograph missing the requirement for resolving power around 380 nm. The variations in resolution around 4000–5000 Å are likely due to slight differences in the alignment of the detectors or optics, affects that tend to be amplified at blue wavelengths. A fraction ($\lesssim 25\%$) of the BOSS fibers therefore do not meet specifications for spectral resolving power in the wavelength range $3800 < \lambda < 4900$ Å.

In addition to the resolving power as a function of wavelength, we have also determined the RMS width σ_p of the line-spread function in native pixels to demonstrate the spatially varying resolution over the focal plane. Figure 2.7 shows the measured RMS pixel resolution of the illuminated region for each of the four BOSS CCDs. For the blue cameras, the spectra near the edges of the detector

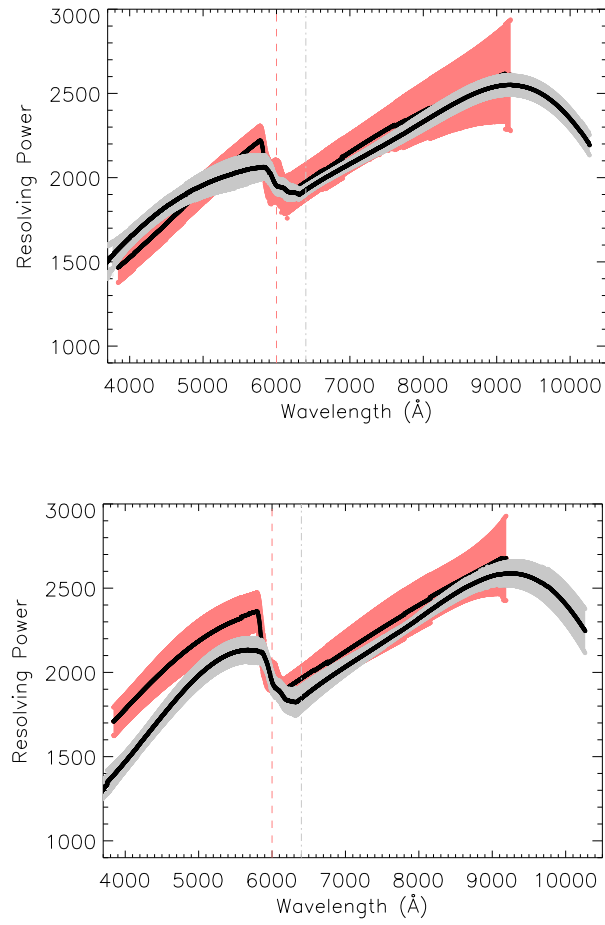


Figure 2.5 The resolving power for BOSS (gray) and SDSS (red). The shaded regions correspond to the regions that contain 68% of the plates in the measurement. The top panel shows the results for Spectrograph 1 and the bottom panel shows the results for Spectrograph 2.

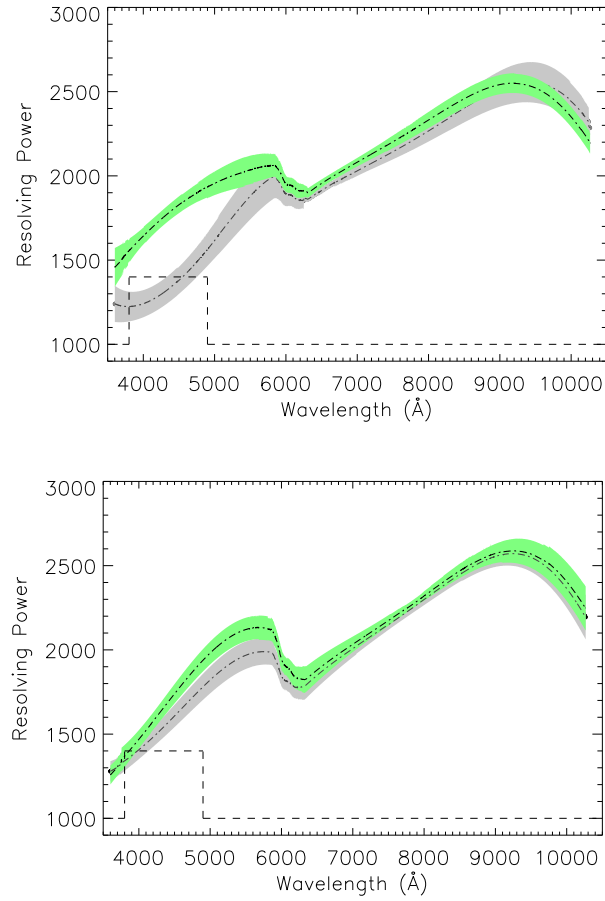


Figure 2.6 The requirements and the measured resolving power for the two BOSS spectrographs. The results for Spectrograph 1 are shown in the top panel. Results for Spectrograph 2 are shown in the bottom panel. The dashed black curve is the requirement for the resolving power. The green curve is the 68% confidence limit about the mean of the resolving power for the central fiber and is representative of $\sim 80\%$ of the fibers. The gray curve is the 68% confidence limit about the mean of the resolving power for a representative fiber near the edge of the spectrograph slit.

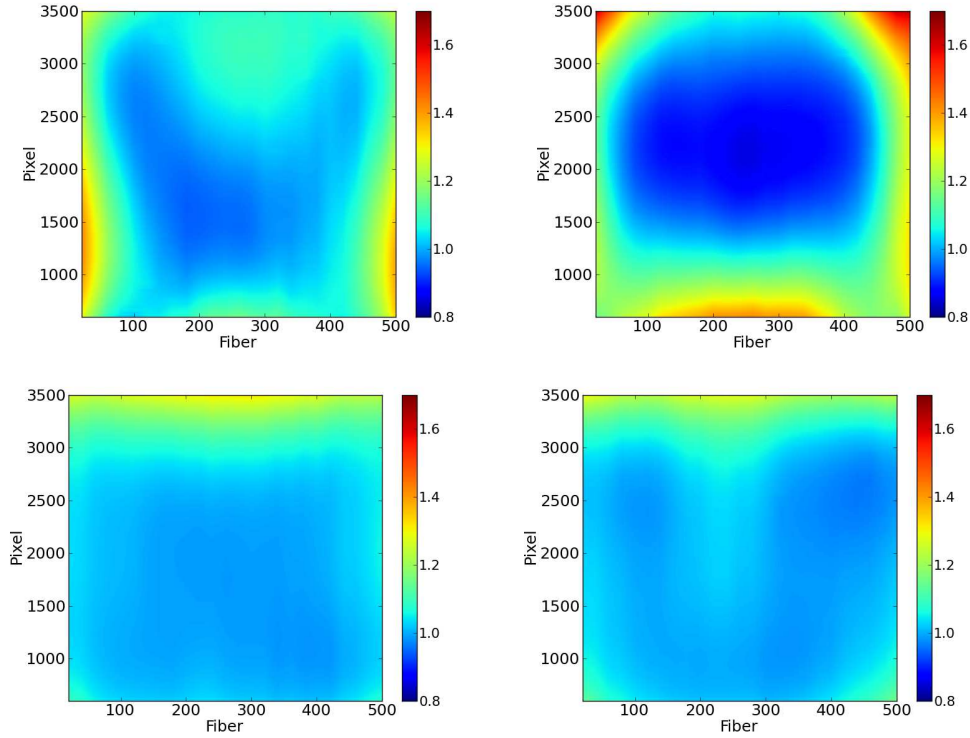


Figure 2.7 The RMS width in pixels in the wavelength direction for each of the four BOSS CCDs. The top panels represent the two blue cameras while the bottom panels represent the two red cameras. In all cases, the wavelength increases from the bottom of the image to the top of the image. The SDSS images have similar characteristics and are not shown here.

have a higher σ_p , reflecting the lower optical quality and deviations from flatness of the focal plane at large field angles. The optics project a saddle-shaped focal plane which contributes to this poorer resolution, an effect that is broadly consistent with predictions in Section 2.2.1. The two red cameras display increased RMS width between $9500 < \lambda < 10,200 \text{ \AA}$, mostly as a consequence of the increased path length of longer wavelength light in the silicon.

2.3.2.3 Throughput

The primary motivation for rebuilding the spectrographs for BOSS was to increase the instrument throughput. We define the throughput as the ratio of the measured flux for a point source relative to the incoming flux outside the atmosphere. A higher throughput is important for the fainter objects targeted by BOSS, particularly the highest redshift galaxies and the quasars near the magnitude limit of the survey. The throughput described here is the throughput of the entire instrument.

The throughput is measured from the spectrophotometric standard stars on the plate during

science exposures. For each standard star, raw photon counts are measured using a 3-pixel radius boxcar extraction on the calibrated, two-dimensional science frame before flux calibration. The aperture is centered on the spectral trace using the fiber flat-fields from the calibration sequence. The photon counts from the source are estimated at each pixel using the observed magnitudes from the SDSS imaging survey and the synthetic spectral template derived from spectrum. The synthetic spectrum is converted to photons per pixel using the wavelength solution, the effective collecting area of the obstructed primary mirror, and the time of each exposure. The throughput at each pixel is calculated by taking the ratio of the measured raw counts to the number of photons per pixel as predicted by the model.

The throughput for SDSS was measured by averaging the throughput from 84 different standard stars observed under photometric conditions at an airmass of ~ 1.0 and seeing $\leq 1.15''$. Because BOSS has smaller fibers, the measured throughput on the BOSS spectrographs is more susceptible to guiding errors. We attempt to mitigate this effect by averaging the throughput over the four stars that produce the highest throughput on each camera. The throughput for BOSS was measured by averaging the throughput of 24 stars over three plates, split evenly between the two spectrographs. As with SDSS, we selected standard stars observed under photometric conditions at an airmass of ~ 1.0 and seeing $\leq 1.15''$. In both SDSS and BOSS measurements, we correct small differences in seeing by normalizing the observed flux to a double Gaussian PSF (as described in Section 2.2) with FWHM of $1''$ integrated over an aperture that corresponds to the area of the $2''$ or $3''$ fiber. The throughput curves have been flat-field corrected to account for fiber-to-fiber variations, thereby normalizing each fiber to the median for each plate.

As shown in Figure 2.8, the throughput after the BOSS upgrades has been significantly improved. The ratio of BOSS to SDSS throughput is also shown in Figure 2.9. Not demonstrated here is a fiber dependent variation in the throughput. As in the resolution measurements, fibers near the edge of the BOSS detectors have a slightly lower throughput than fibers near the middle of each spectrograph. For BOSS, there is an additional $\sim 10\%$ RMS variation on the average throughput curve (particularly at short wavelengths) between standard stars. This variation in BOSS is likely caused by scale changes in the telescope over the course of an observation and possible guiding errors (BOSS is more sensitive to guiding because of the smaller fibers). The effect is probably present in the SDSS data as well, but is amplified in BOSS due to the decrease in fiber diameter.

Overall, the SDSS spectrographs delivered on-sky throughput that was consistent between the two instruments to within approximately 10% across all wavelengths, fell short of design predictions by roughly 10–25% depending on wavelength, and met the requirements set forth in Section 2.2.2 except at the bluest wavelengths where the 8% and 9% delivered throughputs at 4000 Å, for Spectrographs 1 and 2, respectively, is compared to the requirement of 10%. The throughput predictions were based on a combination of measured, published, and modeled efficiency curves for a large number of system components, and the agreement with measured throughput to 10–15%

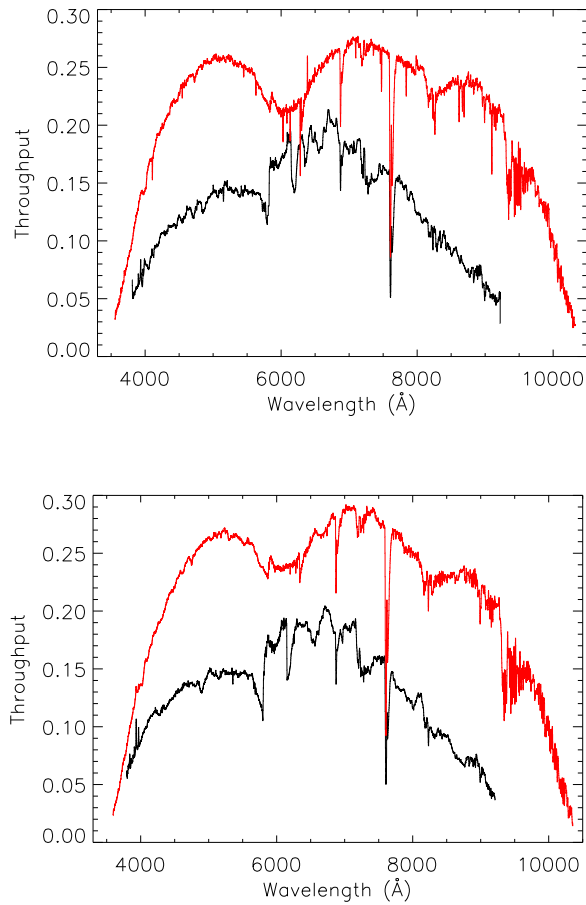


Figure 2.8 Throughput curves for SDSS (black) and BOSS (red). The results for Spectrograph 1 are displayed in the top panel. The results for Spectrograph 2 in the bottom panel. Note the telluric absorption features.

over the majority of the bandpass is satisfying, as is the agreement in overall spectral shape. The largest uncertainty in the throughput prediction is the telescope, which is not well characterized and continually changes with exposure to the environment and periodic cleaning of optical surfaces. The telescope contains two skyward looking surfaces, the primary mirror and the first surface of the dual element wide field corrector. These surfaces, in addition to the secondary mirror, are periodically cleaned with CO₂ snow, which deals with much of the dust but not *stickier* contaminants such as pollen. This contamination undoubtedly degrades the UV throughput of the telescope more than the longer wavelengths but again, is not well characterized. In addition, the efficiency of several other system components in the UV is rolling off precipitously; thus, the wider discrepancy between predicted and measured throughput in the UV is not unexpected.

The BOSS spectrographs exhibit somewhat more variation in throughput between the two instruments, but not to any degree of surprise or concern; the greatest variation is about 15% in

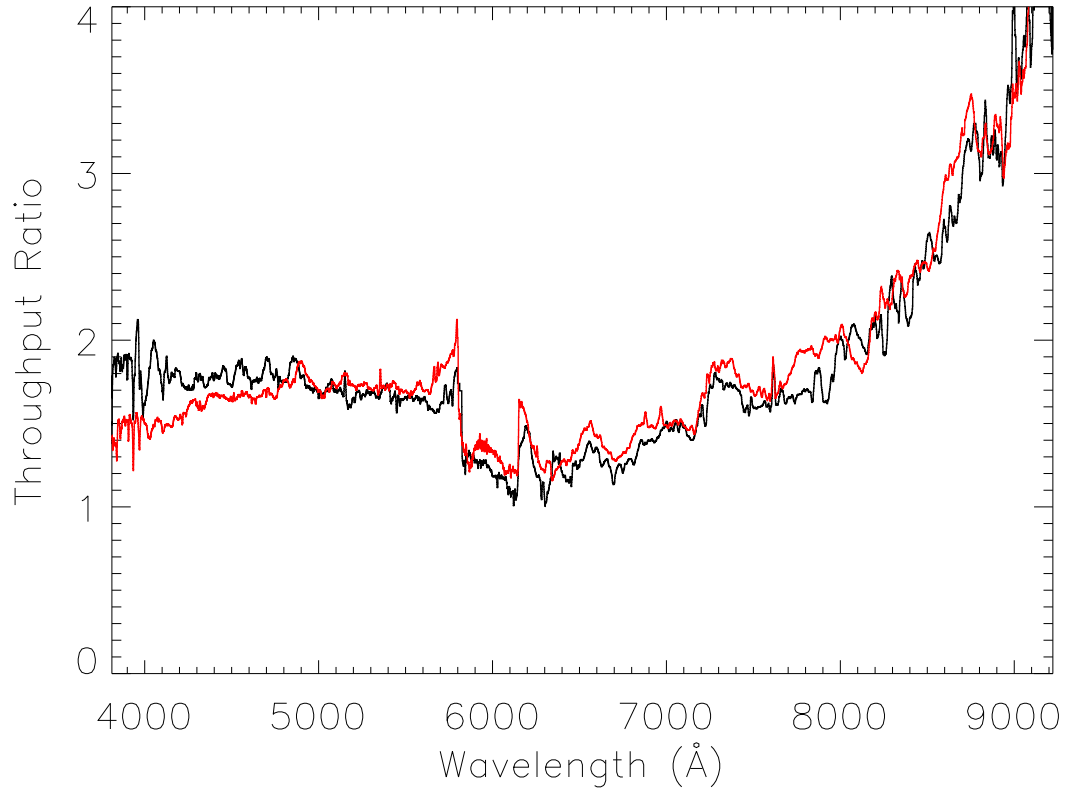


Figure 2.9 Ratio of throughput (BOSS/SDSS) after applying a median smoothing kernel of width 100 pixels. The figure displays results for Spectrograph 1 (black) and Spectrograph 2 (red).

the dichroic crossover region near 6000 Å, while the difference in peak throughput is only 5%. The discrepancy between predicted and measured throughput is flatter across the bandpass than was the case for SDSS, with an average shortfall in measured throughput of roughly 15%. The discrepancy is highest at both ends of the bandpass, but not dramatically so and this may exonerate the telescope throughput model somewhat as a major suspect in the UV discrepancy for SDSS. Again, many component efficiencies are rolling off in the UV and at the other end for BOSS, at 10,000 Å the CCD efficiency is falling steeply.

The requirement on BOSS throughput from Section 2.3.2.3 is a factor of two increase in peak throughput relative to SDSS. While the actual peak throughput was increased by only about 40%, from 21% to 29%, the throughput was nearly doubled over much of the blue bandpass, and was more than doubled longward of 8000 Å.

2.3.3 Flexure

Flexure was characterized for both SDSS spectrographs in 1999. Measurements were taken with the telescope near the horizon at a zenith angle of 72° . A sparsely populated plate was illuminated with Ne and HgCd arc lamps to provide an array of spots at mostly random positions on the CCDs. Data were taken approximately every 45° over the entire 360° range of the rotator. The sign convention is such that positive rotator angles represent a counterclockwise rotation of the rotator as viewed from behind the rotator. Positive values in the spectral direction represent motion of the spots toward longer wavelengths, and positive values in the spatial direction represent motion of the spectra toward a higher column number on the CCD. For reference, a photograph of the spectrographs on the back of the rotator is shown in Figure 2.10. As shown, the rotator is at the zero degree orientation, and the telescope is at a zenith angle of 60° .

Figure 2.11 shows image motion as a function of rotator angle for both the spectral and spatial directions in Spectrograph 1. Results for Spectrograph 2 are comparable and a summary can be found in Table 2.1. At $24\ \mu\text{m}$ per pixel, flexure in the spectral direction was measured to be ~ 0.3 pixels in the worst case in the red channel and ~ 0.33 pixels in the worst case in the blue channel over a 15° rotation. Total flexure in the spectral direction, over the 360° rotator range, was

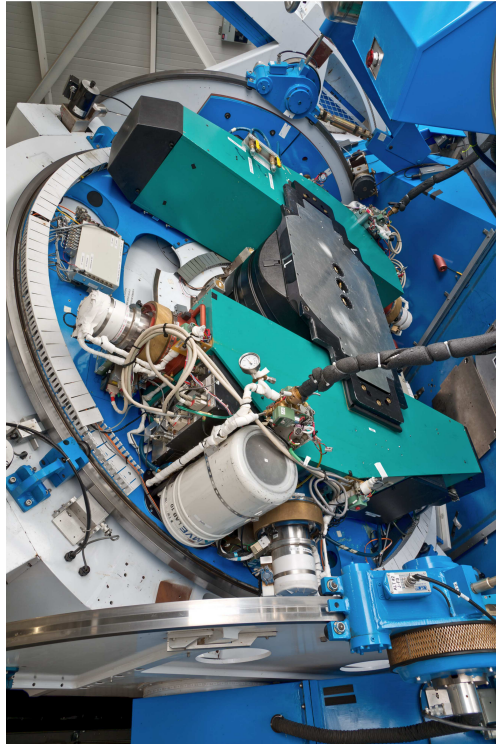


Figure 2.10 Photograph of the spectrographs mounted to the Cassegrain rotator. Spectrograph 1 is on the right. Spectrograph 2 is on the left. In this orientation the rotator is at zero degrees. Positive rotation is defined as counterclockwise motion as viewed from behind the rotator. Here, the telescope is at a zenith angle of 60° .

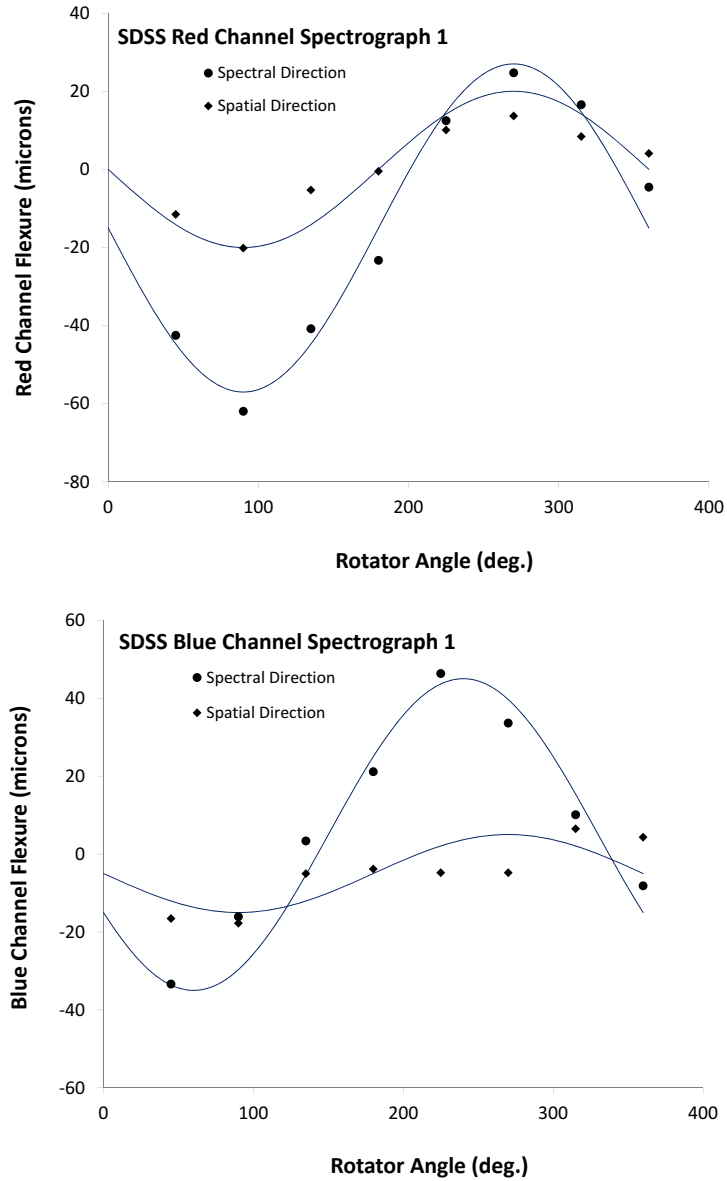


Figure 2.11 Gravity induced image motion in SDSS Spectrograph 1 as a function of rotator angle for a zenith angle of 72° . Twenty-four microns represents one pixel. The top and bottom plots show flexure in the red and blue channels, respectively. Flexure in the spectral direction is greater than in the spatial direction due to compliance in the collimator mount; a natural consequence of a tall mirror.

measured to be ~ 3.6 pixels peak-to-valley in the red channel and ~ 3.3 pixels peak-to-valley in the blue channel. In the spatial direction the flexure was lower, about 0.2 pixels in both channels over 15° . Total flexure in the spatial direction was measured to be ~ 1.4 pixels and ~ 1.1 pixels peak-to-valley in the red and blue channels, respectively. It should be noted that these results are near worst case since most fields observed are much further from the horizon, and flexure is at a maximum at the horizon. Flexure scales as the sine of the zenith angle for instruments on a Cassegrain rotator.

These results are in-line with the performance goal of 0.3 pixels for 15° on the sky that was discussed in Section 2.2.3. A noteworthy observation from the results is that the flexure is much worse in the spectral direction, a surprise that should have been anticipated given the collimator mount design. The tall rectangular collimator is supported by a thin membrane fastened to the rear face of the collimator. Having the support behind the center of gravity, combined with the fact that the tip/tilt/piston actuators are not infinitely rigid, allows the mirror to tilt slightly as the gravity vector changes. Considering the contact points of the actuators, the collimator tilts considerably more in the narrow (spectral) direction than in the tall (spatial) direction.

Not long into SDSS operations a subtle problem appeared in the blue channel of one of the spectrographs. It was discovered that the blue camera on Spectrograph 1 (b1) would go out of focus more often than the other cameras. This sudden defocus would tend to happen over a particular range of rotator angle ($90^\circ - 135^\circ$), sometimes requiring a refocus of the collimator. Measurements in 2004 indicated the CCD tilted approximately $35 \mu\text{m}$ (corner-to-corner) over a small range of rotator motion but the location of the spectra did not change. In the early phases of BOSS, the problem suddenly got worse, probably due to the increased mass of the BOSS dewars. It was discovered that the focus locking mechanism, by design, did not lock-out the backlash in the focus ring threads. The locking mechanism was redesigned and the problem was finally solved.

With the implementation of upgraded cameras and a redesigned focus locking mechanism, flexure was recharacterized for BOSS. Figure 2.12 shows image motion as a function of rotator angle for both channels of Spectrograph 1. Measurements were taken with the telescope zenith angle at 60° , then scaled to a zenith angle of 72° for comparison with the results for the SDSS spectrographs. From Figures 2.11 and 2.12 it is clear that the new focus locking mechanism reduced flexure overall. Total flexure in the spectral direction, in microns, was reduced from $\sim 85 \mu\text{m}$ peak-to-valley in the red channel of SDSS Spectrograph 1 to $\sim 52 \mu\text{m}$ peak-to-valley in BOSS. Similarly, flexure in the blue channel was reduced from $\sim 80 \mu\text{m}$ peak-to-valley to $\sim 47 \mu\text{m}$ peak-to-valley in the spectral direction. However, given the smaller, $15 \mu\text{m}$ pixel CCDs used in BOSS, the results are comparable to SDSS in units of pixels. For 15° on the sky, the spectral shift is 0.41 pixels (worst case) in both channels of BOSS Spectrograph 1, modestly lower than the design expectation of 0.5 pixels; Spectrograph 2 is 0.44 pixels in the worst case. In the spatial direction, the worst case flexure is 0.18 pixels in Spectrograph 1, and 0.15 pixels in Spectrograph 2. Again, see Table 2.1 for

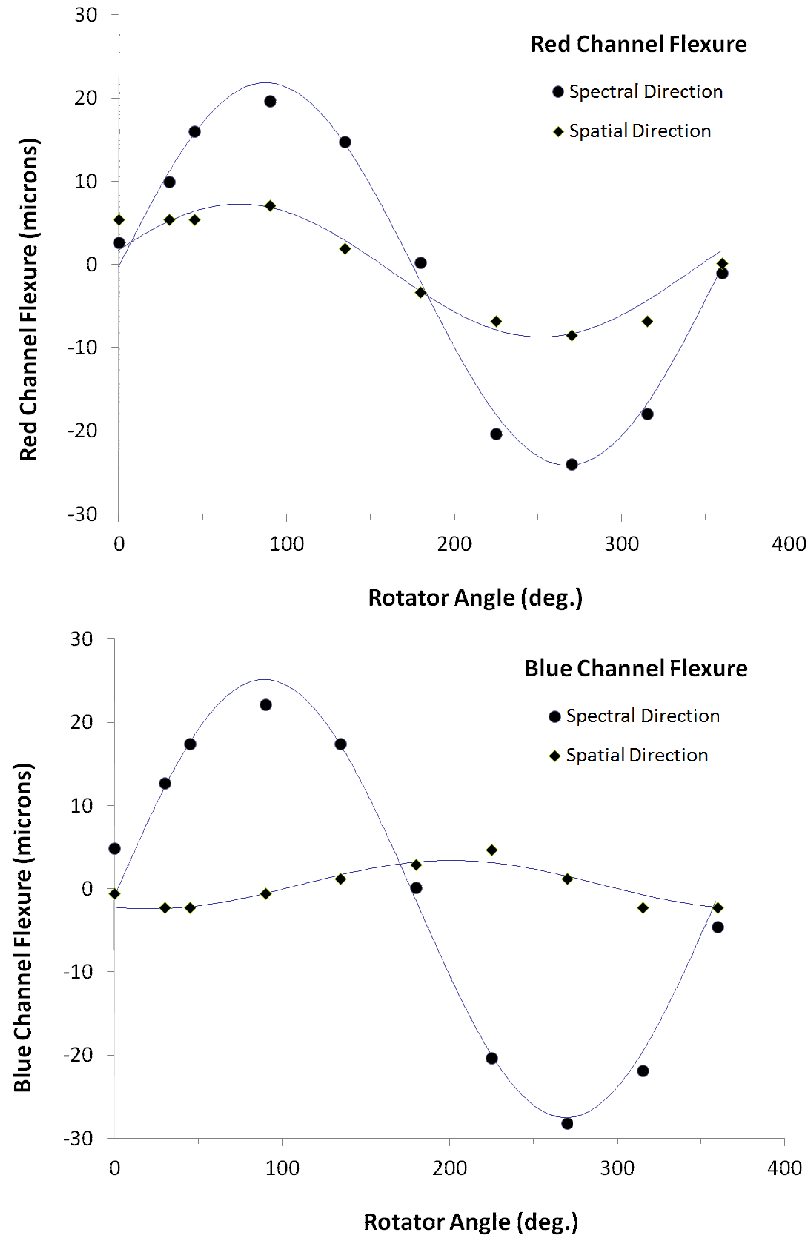


Figure 2.12 Gravity induced image motion in BOSS Spectrograph 1 as a function of rotator angle for a zenith angle of 72° . Fifteen microns represents one pixel. The top and bottom plots show flexure in the red and blue channels, respectively.

a summary of the results.

2.3.4 CCD and Electronics Performance

We measured the CCD and electronics performance for SDSS and BOSS and report the performance in Table 2.2. Because the detectors are divided into multiple quadrants, we report the range of each measurement between the lowest value and highest value obtained in the quadrants of each detector. While only a few aspects of detector performance were specified during the design of the surveys, we describe the results of the detector performance below. When detector performance was specified, the CCDs exceeded specifications in all cases except for small regions on the r2 camera which slightly exceed the design goal of $2\ e^-/\text{pix}/15\ \text{min}$ of dark current.

First, the CCD images were checked for cosmetic defects such as saturated hot pixels, pixels with a large deviation from neighbors, blocked columns at low flux levels, and other bad pixels. These bad pixels are masked during the data processing. The hot pixels are recorded by identifying any pixel greater than 15,000 ADU in the bias exposures. Hot columns are identified in bias exposures as regions of connected pixels that lie above the background, in the direction of parallel clock transfer, by an amount equal to five times the read noise. For SDSS, pixel-to-pixel variation was mapped using the flat field dither technique. For BOSS, pixel-to-pixel variation is mapped using the images taken with the lossy-fiber. Blocked columns and defective pixels are identified in these images as clustering of pixels that lie 50% below the mean background. The flat fields from these tests are also applied at the same time as the bad pixel masks in the data processing. Other bad pixels are found from a combination of flats, biases, and dark frames.

In addition to cosmetic defects, the read noise, dark current and gain of the CCDs were measured. The read noise was measured in a series of zero second exposures; bias frames that were obtained throughout the surveys. A series of 15 minute exposures is averaged pixel-by-pixel to determine the dark current in each pixel. We include any light source detected by the CCDs that does not originate from the fibers, including light leaks, in our measurement of dark current. The dark current in each quadrant of a CCD is averaged, and we report the minimum and maximum values of dark current in the four quadrants. Gain is determined for each quadrant from photon statistics in a series of flat field exposures.

For BOSS, we use measurements in the detector lab at LBNL to determine full-well depth for the red CCDs. We refer to documentation from e2v for these measurements on the blue CCDs. The full-well depth exceeds the maximum number of electrons expected ($65,000\ e^-/\text{pixel}$) in a science exposure for all cameras. The charge transfer efficiency (CTE) records the fraction of electrons that are successfully transferred during each clock cycle during readout. CTE for the red CCDs was measured using an ^{55}Fe source (as described in Bebek et al. 2002; Dawson et al. 2008) in the LBNL detector lab for the red CCDs and recorded from the e2v documentation for the blue CCDs.

Table 2.2 CCD Performance for SDSS and BOSS

	read noise (e^-)	dark current ($e^-/\text{pix}/15 \text{ min}$)	gain (e^-/ADU)	number of bad columns	fraction of bad pixels
SDSS					
b1	2.8–3.8	1.05–1.10	1.05–1.10	4	
b2	3.2–3.9	1.23–1.26	1.23–1.26	4	
r1	3.5–4.1	1.00–1.09	1.00–1.09	14	
r2	3.6–4.4	1.04–1.05	1.05	10	
Start of BOSS					
b1	1.79–1.98	0.64–0.68	1.01–1.05	0	2.0e-05
b2	1.74–2.04	0.61–0.65	0.99–1.04	2	2.1e-04
r1	2.36–2.72	0.88–1.10	1.54–1.97	5	1.4e-04
r2	2.42–2.99	0.95–1.97	1.54–1.96	3	1.8e-04
MJD 55300 (r2 replaced)					
b1	1.83–2.01	0.51–0.53	1.01–1.05	0	2.1e-05
b2	1.87–2.03	0.53–0.56	0.99–1.04	2	2.1e-04
r1	2.43–2.73	0.63–0.80	1.54–1.97	5	3.3e-04
r2	2.73–2.89	1.19–2.27	1.59–1.66	11	4.4e-04
MJD 55800 (r1 replaced)					
b1	1.77–2.02	0.46–0.49	1.01–1.05	0	2.1e-05
b2	1.86–2.01	0.56–0.59	0.99–1.04	2	2.1e-04
r1	2.45–2.82	0.57–0.82	1.47–1.93	1	3.3e-04
r2	2.85–2.88	1.30–1.56	1.59–1.66	11	2.5e-04

The details are shown in Table 2.2

All detectors exceed the CTE requirement of 0.99999 in both serial transfer and parallel transfer. Finally, to meet our goal for overall observing efficiency, a maximum of 70 seconds can be used for the CCD pre-exposure flush time and end-of-exposure readout time. The readout time of the BOSS CCDs has been measured to be 55.6 seconds as described above. This requirement means that not more than 10% of the observing time is used for the CCD flush and readout for two calibration exposures and four 900 second science exposures. Because the detectors have been replaced by newer technologies, we do not report values for full-well depth, CTE, or readout time for the SDSS detectors.

CHAPTER 3

SUPERNOVA HOST GALAXY TARGET SELECTIONS

The improved sensitivity and expanded wavelength coverage of the BOSS spectrographs relative to SDSS motivated a decision to increase the sample size of SDSS-II host galaxy spectra. The host galaxy spectroscopy from SDSS-I and BOSS is used in this analysis to determine redshift estimates for the SN candidates, assess the photometric classification using the spectroscopic redshift as a prior (Chapter 4), determine galaxy properties using photometry and spectroscopy (Chapter 5), and assess the SN light curve properties with the addition of host galaxy redshifts (Chapter 6).

3.1 Imaging and Light curves

The SDSS-II SN Survey occurred over the three Fall seasons of 2005-2007 following a commissioning period in Fall 2004. The survey observed the five SDSS filters (*ugriz*) to obtain imaging over the 300 deg² southern equatorial region known as Stripe 82 ($-60^\circ < \alpha < 60^\circ$, $-1.25^\circ < \delta < 1.25^\circ$). Stripe 82 was observed repeatedly with a cadence of roughly four days from September 1–November 30 in each season except near full moon (see Frieman et al. (2008)). Of the five filters, *gri* were used in the SN detection algorithms.

During the survey, the data were processed daily to allow rapid response spectroscopy on as many SN Ia candidates as possible. Each image was compared to an image template derived from earlier observing seasons and the subtracted frames were searched for variable objects (Sako et al. 2008). Variations of at least three standard deviations above background in at least two contiguous pixels were considered possible variable objects in the first stage of analysis. Regions of stars and known variability such as active galactic nuclei (AGN) were masked and not included in the search for possible SN candidates. A visual screening process was performed on these candidates to reject artifacts and objects that were not SNe.

³The results reported in this chapter have been submitted to the Astronomical Journal, referenced as “Host Galaxy Spectra and Consequences for SN Typing From The SDSS SN Survey,” Olmstead, M.D. et al., 2013, submitted to AJ, arXiv:6818.

Objects selected by the visual screening are designated “candidates” and are stored in a database. The database contains 21,787 transient candidates on Stripe 82. SN Ia and core-collapse SN light curve templates were fit to the time series photometry from each candidate and interesting candidates were again visually inspected. Spectroscopy was performed on highly probable active SN Ia candidates, leading to 518 spectroscopically-confirmed SNe Ia using the same techniques as in the first year of the survey (Zheng et al. 2008). Other types of SNe were also identified during the classification and visual inspection. A small number of these non-SN Ia objects were spectroscopically classified from this spectroscopic program: 7 SNe Ib, 11 SNe Ic and 67 SNe II. The initial sample of 21,787 transients was filtered so that only candidates with light curves constructed from scene model photometry (SMP) are used (Holtzman et al. 2008). SMP uses a stack of images without convolution or spatial resampling to determine the brightness of the time-varying SN. This sample includes all candidates that were detected on at least two dates, thereby eliminating most artifacts. The filtered sample contains 10,468 candidates that are likely astrophysical in nature. It is this sample that is described in detail in S13 and made available in the public database.

Although considerable resources and time were used for spectroscopic investigation of these candidates, many candidates were never observed spectroscopically. While spectroscopic confirmation is no longer possible for these SNe, spectra of the host galaxies allows for improved cosmology and other studies requiring a precise redshift. It also increases the sample of higher redshift SNe and can be obtained in a much more efficient manner.

3.2 Photometric Classification

The sample of 10,468 candidates was further decomposed into likely transients and likely SNe based on the classification method Photometric SN IDentification (PSNID) of Sako et al. (2008, 2011). To be photometrically classified as an SN, a candidate must show variability in only one observing season. When this restriction is applied, the number of valid candidates is reduced to 6697.

In PSNID, a χ^2 value is calculated for each candidate by comparing the observed photometry against a set of SNe Ia and core-collapse SN light curve templates. The best matching SN type and parameters are recorded for each object without using redshift information as a prior.

The technique was improved in Sako et al. (2011) to include a calculation of the Bayesian probabilities that a candidate is a Type Ia, Ib/c, or II, denoted P_{Ia} , P_{Ibc} , and P_{II} respectively. Empirical model errors were folded into the Bayesian probabilities, additional core-collapse templates were added, and a Markov Chain Monte Carlo simulation was used to estimate the posterior probability distribution for the five parameters in the Bayesian classification. A total of 33 candidates with variability in only one year fail to converge on a solution in PSNID and do not have well-defined Bayesian probabilities. Full details of the photometric typing are found in S13.

The sample of 6,664 is divided into objects of varying PSNID probability, χ^2 value, and quality of light curve coverage. The cuts placed on the entire sample of 10468 candidates is shown in Table 3.1. The details of the initial target ranking for host galaxy spectroscopy are described below and summarized in Table 3.2.

- **High Probability SNe Ia:** Using the same criteria as Sako et al. (2011) for the photometric SNe Ia, the highest priority candidates for host spectroscopy have a Bayesian probability P_{Ia} greater than 0.9, a χ^2 per degree of freedom less than 1.8, and a well-sampled light curve. In this case, we define a well-sampled light curve as one with at least two measurements that constrain peak and fall time; one measurement must be within five days (rest-frame) of peak luminosity of the best fit SN Ia template and one measurement must be between five and 15 days (rest-frame) after peak luminosity of the best fit SN Ia template. A total of 1574 candidates meet these criteria.

- **Possible SNe Ia:** We increase the number of possible SNe Ia candidates by loosening the restrictions from the high-probability photometric SNe Ia sample. For the next priority in host galaxy observations, we require that candidates meet two of the three above conditions and have χ^2 per degree of freedom less than 2.0. There are a total of 706 possible SNe Ia candidates.

- **Low Probability SNe Ia:** The remaining candidates that have Bayesian probability P_{Ia} greater than P_{Ibc} and P_{Ia} greater than P_{II} are designated low probability SNe Ia. There are 1718 low probability SNe Ia candidates.

- **Core-Collapse:** A large sample of possible core-collapse SNe was identified during the SDSS-II SN Survey. A candidate is classified as likely core-collapse when the best fit Type Ibc or II Bayesian probability is greater than the SNe Ia Bayesian probability; 2666 candidates are identified as core-collapse candidates and assigned fourth priority for host galaxy spectroscopy.

- **Remainder Sample:** All 3804 remaining candidates are denoted members of the “remainder sample.” This sample includes candidates that show variation in more than one year, and candidates where the classification did not converge in the light curve fits. These remainder sample host galaxies are given lowest priority in target selection and chosen to examine possible incompleteness in the SDSS SN sample.

The likely host galaxy of each of the 10,468 variable candidates was initially identified from DR7 photometry. The SDSS spectral database was examined for existing host galaxy spectra: 3810 host galaxy spectra existed in the database and are categorized according to spectroscopic prioritization in Table 3.2. The redshifts from SDSS can be used to assess the SN classification of these candidates by using the host galaxy redshift as a prior. The remaining candidates were prioritized for spectroscopy with BOSS.

Table 3.1. Sample Selection

Selection	Remaining Candidates For Host Spectroscopy
All Candidates	10,468
Variation only one year	6,697
Have Bayesian SN Probability	6,664
No SDSS spectra	5,574

Table 3.2. Target Priority

Selection Method	# Meeting Criteria	# SDSS Redshifts	# BOSS Redshifts	Median r -band fiber2magnitude	Max r -band fiber2magnitude
High Probability SNe Ia	1574	132	807	21.33	23.67
Possible SNe Ia	706	148	222	20.50	22.52
Low Probability SNe Ia	1718	203	1050	20.59	23.94
Core-Collapse	2666	421	672	20.67	23.45
Remainder Sample	3804	3008	319	19.45	23.66

3.3 BOSS Target Selection

A majority of fibers ($\sim 80\%$) in BOSS observations are dedicated to BAO galaxy or quasar targets; some of the remaining fibers were made available to diversify the spectroscopic sample by observing other objects in the BOSS footprint. Dubbed ancillary programs, these additional fibers were assigned to smaller programs proposed by members of SDSS-III, as explained in the appendix of Dawson et al. (2013). An ancillary program was proposed to obtain spectroscopy of all host galaxies of transients from the SDSS-II SN Survey.

Candidates for host galaxy spectroscopy were chosen from the reduced sample of 10,468 variable objects in the 220 deg^2 region $\alpha_{J2000}=[-42.9^\circ, 44.9^\circ]$, $\delta_{J2000}=[-1.26^\circ, 1.26^\circ]$ that was covered by BOSS. A total of 3375 objects were selected using the broad approach of targeting host galaxies of likely SN first, denoted as Algorithm One in C13, and assigning additional fibers to non-SN, denoted as Algorithm Two in C13.

A restriction on r -band **fibermagnitude** was imposed, where **fibermagnitude** is determined from the integrated flux inside a $3''$ diameter aperture predicted from SDSS imaging. BOSS targeting priority was given to those objects with r -band **fibermagnitude** < 21.25 while an additional restriction was loosely imposed by rejecting targets fainter than r -band **fibermagnitude** of 22. The targets were visually inspected from the SDSS DR7 images to determine the most likely host galaxy of the candidate. The three nearest galaxies were examined and in most cases the nearest galaxy was considered the most likely host. Occasionally the second nearest galaxy (4%) or the third nearest galaxy (1%) was determined to be the most likely host. These galaxies were assigned **ANCILLARY_TARGET1** flags 36, 37, 38, respectively, where **ANCILLARY_TARGET1** denotes the target flag for BOSS ancillary programs on Stripe 82 (Dawson et al. 2013). Selection of the second or third nearest galaxy generally occurred if the nearest galaxy was either a misclassification, bright star or artifact, or a clear background object.

For most of the targets, the center of the host galaxy was selected as the position of the fiber. Additionally, 282 candidates occurred in a host galaxy for which there is already existing SDSS spectra. In these cases the location of the original variability was assigned as the location of the fiber to study the local environment of the candidate. These objects are assigned a BOSS **ANCILLARY_TARGET1** value equal to 39. A sample of 52 active SNe Ia were found in SDSS galaxy spectra (Krughoff et al. 2011); two of these host galaxies were selected to be re-observed with BOSS and were given BOSS **ANCILLARY_TARGET1** equal to 40. The remainder sample discussed in Section 3.2 was selected at random from the parent sample with a loose restriction of $r < 21.5$ to quantify selection and contamination biases. These targets were also visually inspected to select the most likely host from the nearest three galaxies.

3.4 BOSS Observations

In total 4,777 targets were requested for fiber assignment as part of the SDSS SN ancillary science program. Due to restrictions and priorities of BOSS fiber assignments (primarily from a finite number of available fibers and collisions with higher priority targets) only 3761 unique candidates were observed. These targets were distributed over 78 BOSS plates in Stripe 82 and 33 BOSS plates that border Stripe 82. Figure 3.1 shows the footprint of the plates that contained SN host galaxy targets relative to the overall BOSS footprint in the South Galactic Cap, the full BOSS footprint is found in Figure 1 of Dawson et al. (2013).

The host galaxy spectroscopy occurred in 2009 and 2010 in a series of 15 minute exposures until a certain depth was reached for each plate. Observations ceased when a real time reduction pipeline yielded a signal-to-noise ratio (S/N), such that $(S/N)^2/\text{pixel} \geq 26$ over a synthetic i filter for objects with $i = 21$ and $(S/N)^2/\text{pixel} \geq 16$ at $g=22$ using `fiber2magnitudes` corrected for Galactic extinction (Schlegel et al. 1998). As with `fibermagnitude`, `fiber2magnitude` is determined from the integrated flux inside a $2''$ diameter aperture predicted from SDSS imaging. The observations typically consisted of between four and eight 15 minute exposures. The exposures sometimes extended over multiple nights, depending on various factors including weather conditions, visibility of targets, and time of first exposure.

BOSS first observed Stripe 82 during the commissioning period in Fall 2009 and included 10 plates containing SN targets. Full survey observations of Stripe 82 continued into Spring 2010, producing another 795 targets with a confident redshift. In Fall 2010 the entire Stripe 82 region

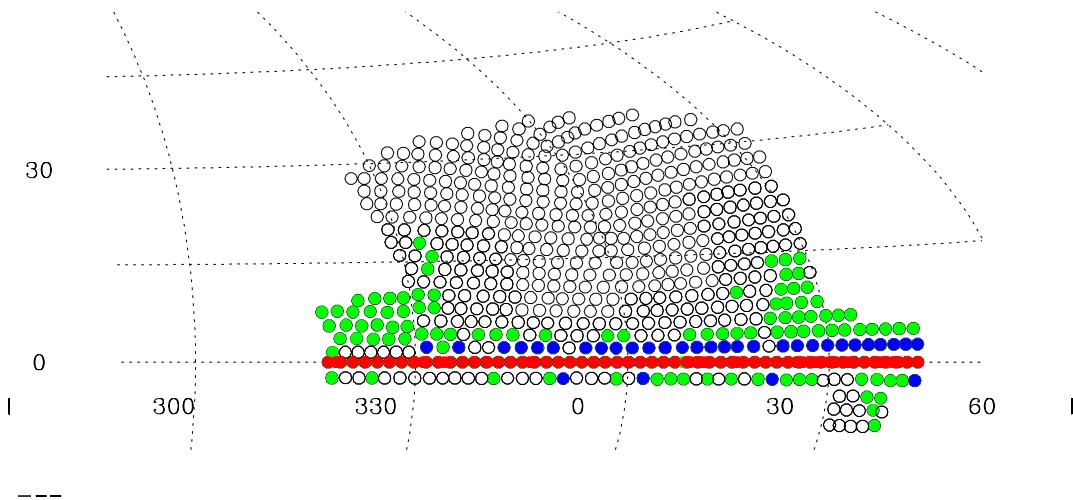


Figure 3.1 The projected five year coverage of BOSS in the South Galactic Cap in equatorial coordinates. The BOSS plates on Stripe 82 used for the SN host galaxy candidates are shown in red. Plates bordering Stripe 82 that contain SN host galaxy candidates have a smaller number of targets per plate and are shown in blue. Regions included in DR9 are shown in green and regions to be observed in the final three years are shown as open circles.

was retiled and the remaining targets were either observed for the first time or re-observed if there was not a reliable redshift from the first year observation, see Section 3.6 for details on redshift reliability. When a target was observed during both commissioning and regular operation, the later observation is considered the primary spectrum for this analysis.

3.5 Photometric Classification and Host Galaxy Differences Between C13 and the SDSS-II SN Data Release

A cosmological study was performed using the photometrically-classified SNe Ia from the SDSS-II SN Survey in C13. These SNe Ia candidates were classified using spectroscopic redshifts determined by SDSS and BOSS. While the host galaxies described here and in C13 are the same, the SN classifications without galaxy redshifts changed somewhat between C13 and the SDSS-II SN Data Release. In addition, the host galaxy associations for a number of candidates are different. We describe the differences here.

The target selection for BOSS spectroscopy of SNe host galaxies consisted of two separate philosophies: observe the host galaxies of as many likely SNe as possible, assigning fibers to likely SNe Ia with the highest prioritization; and gather spectra for other interesting transients with the allotted fibers. In defining the original SN Ia and bias samples, C13 uses the SN classification that was available in 2009. The target classification described in Section 3.2 uses a newer photometric-only SN classification that will be released in S13. We choose the updated classification in this dissertation because that is the classification scheme that best matches future SN campaigns. This is also the sample that can be recreated using the information in the SDSS-II SN Data Release.

The main difference between the target classification here and C13 is in the number of objects assigned to the likely SNe Ia class and the remainder class. In evaluating the original sample, C13 find 2364 objects classified as high probability, possible, or low probability SNe Ia. C13 identifies 417 objects in their core-collapse sample and 980 objects in their unbiased sample. On the other hand, with the new classification of transients without spectroscopic redshifts, we identify samples of 2079 SNe Ia, 672 core-collapse SN, and 319 remainder sample objects. The decrease in sample size in this dissertation is described in Section 4.1. Objects typed as SN Ia in the final Hubble Diagram of the SN cosmology analysis (Campbell et al. 2013) are flagged with the keyword *Campbell2013* in the SDSS-II SN Data Release.

As discussed in Section 3.3, the original identification of host galaxies was derived from visual inspections of DR7 images. Occasionally, galaxies other than the nearest to the transient event were selected as the likely host galaxy. C13 used the host galaxies from the initial BOSS target selection. The host galaxy identification was updated for the SDSS-II SN Data Release using deeper imaging from SDSS DR8 (Aihara et al. 2011). All primary objects within $30''$ of the SN candidate position were selected as possible host galaxies. The primary object nearest to the SN candidate in terms of light radius was selected as the host galaxy. The primary benefit of using this automated

method with DR8 is that some likely host galaxies were not visible during visual inspection of DR7. Automated matching sometimes misses candidate host galaxies in which the light radius parameters were not able to be determined (primarily faint galaxies). The automated matching also fails to identify the correct host galaxy in the case of extended objects which are deblended into several discrete galaxies.

Host galaxy association changed between C13 and the SDSS-II SN Data Release for nearly one-tenth of the objects. Three hundred and seventy one of these objects were observed in the BOSS sample. From the sample of 3354 objects selected as the nearest galaxy (BOSS `ANCILLARY_TARGET1` 36), 360 were no longer identified as the likely host galaxy. Of the 123 targets initially selected as the second or third nearest host galaxy (BOSS `ANCILLARY_TARGET1` 37 and 38), 11 were removed from the final list of likely host galaxies used for the SN classification in this dissertation and in S13.

We have continued to improve the sample and data reductions since C13. Although this has changed the sample, that does not mean the conclusions of C13 are no longer valid. We have found similar results to C13 as described in Section 6.1 and Section 6.2.

3.6 Spectroscopic Data Reduction and Redshift Determination

The BOSS data were reduced in the pipeline referred to as `idlspec2d` described in Dawson et al. (2013)⁴. The two-dimensional images are bias subtracted, flat-field corrected, and masked for pixels with known defects or affected by cosmic rays. The two-dimensional image is then transformed into a one-dimensional image using a flat-field exposure to both determine the profile of each fiber projected onto the CCD and to normalize fiber-to-fiber throughput variations. The wavelength solution is determined from an arc exposure. The arc exposure is performed using a mercury-cadmium lamp for emission in the blue and a neon (neon-argon upgrade for BOSS) for emission at the red end of the spectrum. A sky model is created from the spectra of fibers assigned to locations on the sky in which no objects were detected in the original SDSS imaging. This sky model depends on the fiber position and is subtracted from each one-dimensional spectra. The collection of one-dimensional spectra for each object on the plate is then combined into the coadded spectrum found in DR9.

A sample of spectra from the BOSS SN ancillary program is shown in Figure 3.2. These spectra were chosen to demonstrate the range of S/N, magnitude and redshift of the target sample, as detailed in Table 3.3. Figure 3 of C13 highlights additional spectra chosen to demonstrate the range of S/N of the continuum and two higher redshift SNe Ia host galaxies.

A redshift and galaxy classification is performed by fitting a set of principle component analysis (PCA) templates derived from BOSS data to each coadded spectrum (Bolton et al. 2012). Warnings

⁴The analysis of SNe host galaxy spectra obtained by BOSS in determining redshifts was performed during early stages of the BOSS pipeline development, primarily using v5.4.14 and v5.4.31 of `idlspec2d`.

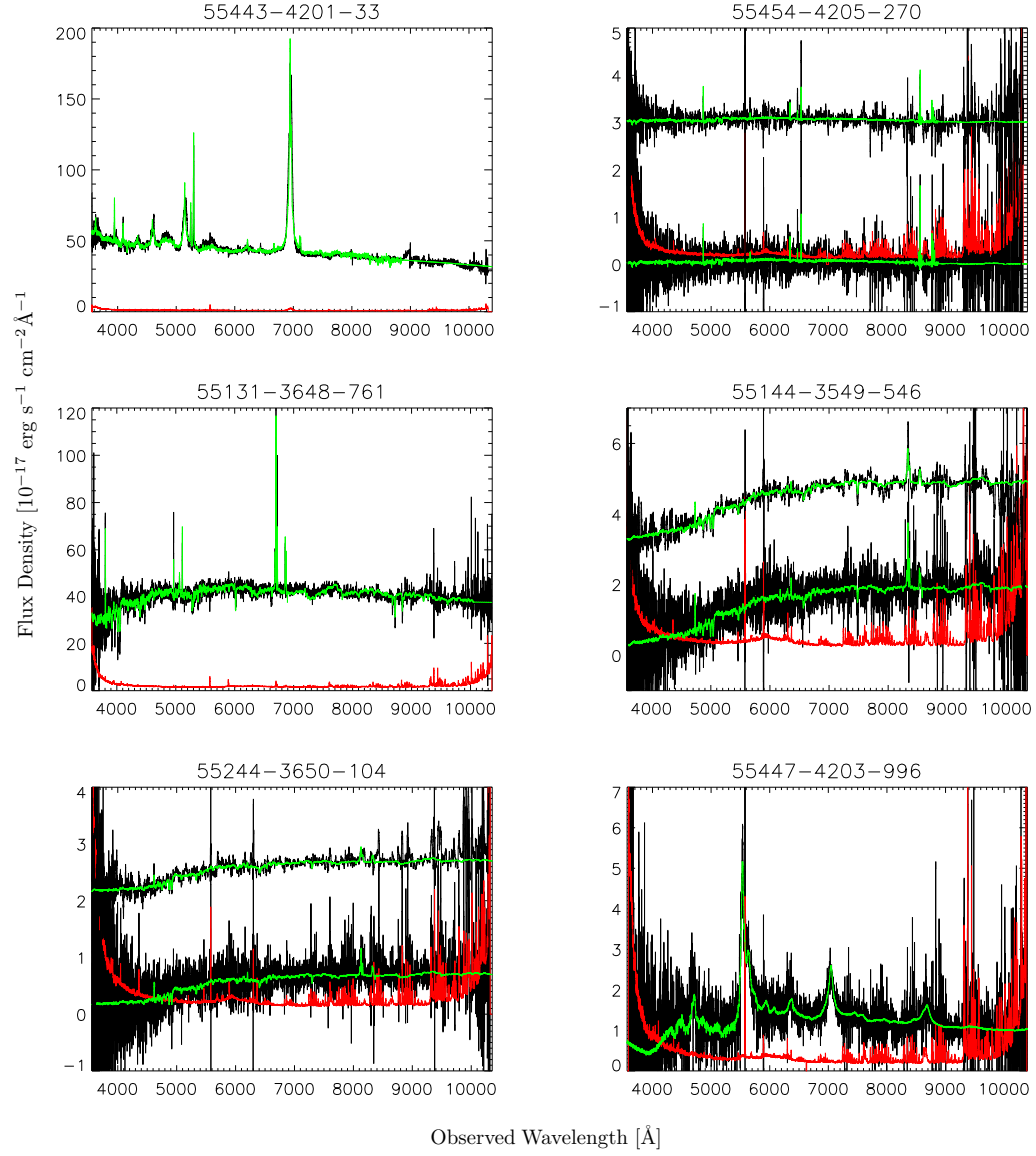


Figure 3.2 A selection of BOSS spectra with secure redshift from the observed SN host galaxy sample. The observed flux is shown in black, the best-fit template in green and the error in red. For the three plots with two spectra shown, the top spectrum is the observed flux with a five-pixel smoothing and offset by $10 \times 10^{-17} \text{ erg s}^{-1} \text{ cm}^{-2} \text{ Å}^{-1}$. Upper Left: One of the highest S/N spectra of a broadline QSO at $z=0.0580$. The variability appeared at $0.20''$ from the center so this candidate was potentially selected by AGN activity. Upper Right: One of the lowest S/N spectra of a galaxy at $z=0.305$. Middle Left: One of the brightest objects (r-band cmodelmag 14.062) of a starforming galaxy at $z=0.02073$. Middle Right: A faint galaxy (r-band magnitude 24.80) at $z=0.238$. Lower Left: A galaxy near median S/N, redshift, and magnitude. Lower Right: The highest secure redshift in our sample, a broadline QSO at $z=3.55$. Table 3.3 presents details on the six spectra.

Table 3.3. Properties of Figure 3.2 Spectra

Objid	Corresponding CID	Redshift	cmodelmag (r)	r-band S/N	Distance to Center(")	SN Type
1237663543148675172	20259	0.0580	17.8	50.4	0.13	Ia
*	20953	0.305		0.27	0.22	Ia
1237663784750940246	13195	0.0207	17.8	24.3	6.04	Ibc
1237678595929931869	17414	0.270	21.1		0.84	II
1237657584950379205	20768	0.239	22.0	2.8	2.0	Ia
1237663479261495791	3562	3.55	21.3	5.1	0.1	II

^a Properties for the spectra in Figure 3.2. The SN type here is based from initial Bayesian probability assuming a flat prior used for target selection. OBJID is the identification number used for matching spectra in DR9. CID is the SN candidate identification used in the SDSS-II SN Data Release. * This galaxy does not have an OBJID and can be matched on plate, fiberid, and mjd in DR9.

for suspect spectra are encoded in the parameter `ZWARNING` found in each data release. The pipeline had a confident redshift (`ZWARNING` = 0) for 91.6% of the targets. The most common redshift failure (`ZWARNING`=4) occurs when there are at least two different redshifts with templates of similar values of χ^2 per degree of freedom; 91.4% of the failed redshifts were assigned `ZWARNING`=4 flags.

The galaxy templates for BOSS have been chosen for optimal redshift performance for the luminous galaxy sample used to constrain BAO in BOSS. The pipeline templates therefore cover a relatively small parameter space in terms of galaxy properties. For galaxy targets in the primary BOSS sample of color-selected massive galaxies, the pipeline has a success rate of 98.7% (Bolton et al. 2012). The SN host galaxy sample, on the other hand, consists of a much more heterogeneous galaxy population and the pipeline efficiency might be suspect. We verified with a visual inspection the pipeline redshifts for this SN host galaxy sample as described below.

Another redshifting routine was made available to BOSS by the WiggleZ Survey (Drinkwater et al. 2010) called RUNZ⁵, allowing us to perform manual redshift estimates. RUNZ is a modified version of the code used for the Two Degree Field Galaxy Redshift Survey (2dFGRS; Colless et al. 2001) and the 2dF-SDSS LRG and QSO Survey (2SLAQ; Cannon et al. 2006) which includes a total of 17 templates; these templates cover the classes of star, galaxy, emission line galaxy, and quasar. Redshifts are determined through a cross-correlation fit between the spectrum and each template. RUNZ also determines a best match to emission line features as a second redshift estimate. The graphical interface is very convenient for manual redshifting because it allows one to assign redshifts to specific spectral features and then identifies the location of additional lines at that redshift. A template at any given redshift can also be displayed as an overlay with each spectrum for easy comparison. A redshift was given high manual confidence when there were at least two spectral features identifiable by visual inspection at that redshift.

We then compared the visual redshift with the `idlspec2d` pipeline redshift. All objects that had no `ZWARNING` flags, good manual confidence, and in which the redshifts agreed were considered robust (3363 objects).

There were 398 targets with disagreement between the `idlspec2d` pipeline and visual redshift, where the `ZWARNING` flag was not zero, or where there was low confidence in the original visual inspection; these were all visually inspected again. In this second manual inspection, two co-authors examined the best fits using the `idlspec2d` pipeline templates and the RUNZ graphical interface. If the two inspectors agreed on the redshift, it was declared confident during the second inspection.

After the second manual inspection, 3520 of the 3761 observed objects were determined to have a secure redshift. Table 3.4 shows the efficiency for obtaining a secure redshift as a function of target magnitude and other observational properties. These objects are found in the online table with `mwarning` equal zero, where `mwarning` is a flag that denotes the quality of the manual inspection. In total, 80 of the final redshifts used in this analysis do not come from the `idlspec2d` pipeline

⁵Maintained by Scott Croom.

Table 3.4. BOSS Target Properties

m _r Bin	# of Objects with secure z	Median Redshift	RMS Redshift	Secure Redshift	Median S/N per pixel	RMS S/N per pixel
17.00-17.50	3	0.0441	0.0264	1.000	52.5	33.5
17.50-18.00	54	0.0554	0.0177	1.000	51.0	16.4
18.00-18.50	10	0.0662	0.0454	1.000	40.3	9.1
18.50-19.00	34	0.0966	0.0486	1.000	28.6	7.2
19.00-19.50	98	0.120	0.0664	1.000	21.3	8.3
19.50-20.00	275	0.176	0.0889	0.996	16.8	6.2
20.00-20.50	399	0.220	0.100	0.998	11.9	4.3
20.50-21.00	540	0.265	0.120	0.987	8.3	3.1
21.00-21.50	609	0.312	0.147	0.990	5.8	2.3
21.50-22.00	522	0.351	0.161	0.987	3.9	1.5
22.00-22.50	359	0.340	0.160	0.932	2.6	1.1
22.50-23.00	143	0.347	0.154	0.872	1.7	0.6
23.00-23.50	56	0.392	0.187	0.727	1.0	0.7
23.50-24.00	8	0.536	0.163	0.364	0.86	0.16
24.00-24.50	1	-0.000324		0.50	0.28	

with `ZWARNING` equal zero, but from a combination of `RUNZ` and additional manual redshifting.

There are 351 spectra from the BOSS commissioning period in which we have confident redshifts. The plates containing these 351 spectra are marked as bad in DR9 and are not contained in the `spAll` summary file. The reduced data for these plates exists in the individual plate directories, but only contain data for one of the spectrographs. For this dissertation, these objects were reduced using an earlier version of `idlSpec2d` including both spectrographs and therefore, will be used only to provide host galaxy redshifts and will not be used in further analysis requiring calibrated spectra. The raw data were released in DR9, but are not recommended for further analysis due to calibration uncertainty associated with commissioning data. Objects with redshifts from the commissioning data are identified with column `spectra_commission` in the public release of SDSS SN light curves described in S13.

As described in Section 3.5, there were 371 objects with confident redshifts observed as part of this BOSS ancillary project that later had a change in host galaxy association. Each of these galaxy spectra were examined as described above with the original BOSS `ANCILLARY_TARGET1` bit and included in DR9 and in the public database. They are marked in the public database in column `bad_host`. Using only BOSS spectra assigned to the correct final host galaxy reduces the sample size with confident redshift to 3083 objects. From the final inspection, BOSS spectra were observed with a confident redshift for 2764 host galaxies of candidate SNe and 319 host galaxies from the remainder sample.

While the actual targets described here and in C13 are the same, we have redefined the remainder sample due to the change in classification schemes and host galaxy identification criteria as described in Section 3.5.

The redshift and the apparent magnitude distributions of these objects are shown in Figure 3.3. The target distribution and redshift statistics binned by r -band apparent magnitude are presented in Table 3.4. A scatter plot demonstrating S/N and redshift range is shown in Figure 3.4.

3.7 SDSS Spectroscopy of SN Host Galaxies

In addition to the BOSS spectroscopic sample described in Section 3.6, there are 3879 candidates with SDSS host galaxy spectra⁶. These galaxies were coincidentally observed as part of the original SDSS program. These SDSS galaxy spectra have higher S/N and lie primarily at a lower redshift than the BOSS sample. The SDSS pipeline was optimized for analysis of this class of objects and is expected to perform effectively in determining redshift estimates of these galaxies.

We performed a brief test of the SDSS pipeline performance by choosing a random subset of 100 spectra from the 3879 host galaxies. We required only that objects were classified with `ZWARNING` equal to zero. This subsample was manually inspected following the same procedure as

⁶The spectra can be found at <http://data.sdss3.org/sas/dr9/sdss/spectro/plates/26/2010-05-23/>

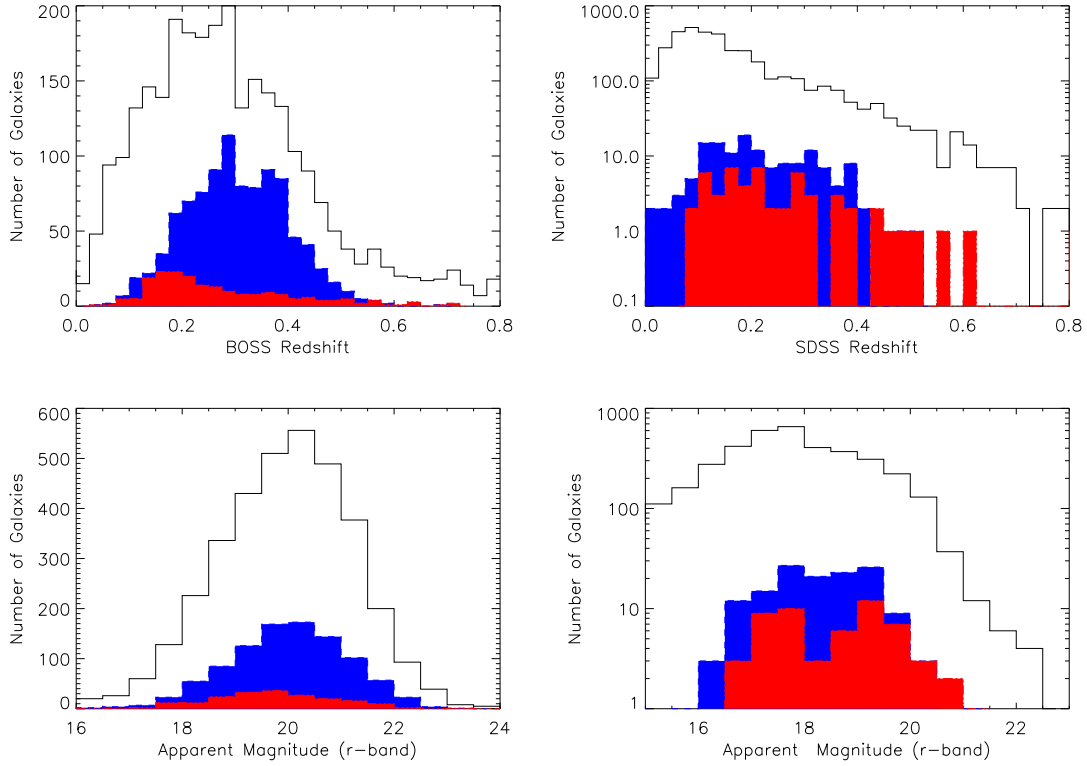


Figure 3.3 The distribution of redshifts and r -band cmodel magnitude of the observed SDSS and BOSS samples. **Top Left:** The distribution of redshifts (for redshifts < 1) of the observed BOSS sample. The entire BOSS sample is represented by the solid line, the dashed line shows the distribution of SNe Ia and the dot-dash line the distribution of core-collapse SNe. **Top Right:** The distribution of redshifts (for redshifts < 1) of the observed SDSS SN host sample with the same line scheme as the top panel. The SDSS sample is put on a logarithmic scale because the number of candidates is dominated by the remainder sample. **Bottom Left:** A histogram of the r -band cmodel magnitude for the BOSS sample with the same line scheme as before. **Bottom Right:** A histogram of the r -band cmodel magnitude for the SDSS SN host sample with the same line scheme as before.

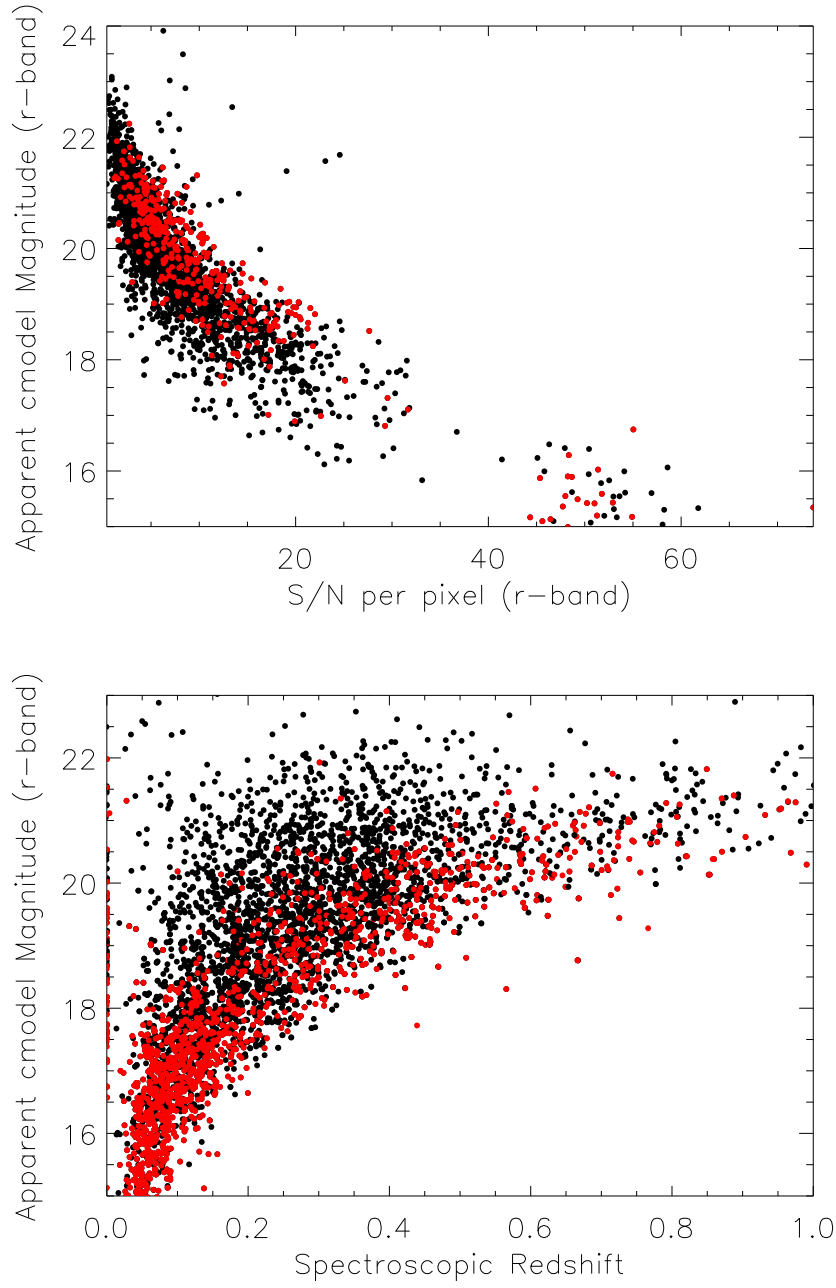


Figure 3.4 Apparent magnitude as function of S/N and redshift. **Top:** The r -band apparent magnitude (cmodelmag) as a function of synthetic r -band S/N per pixel for the BOSS spectroscopic sample. The remainder sample is shown in red. **Bottom:** The r -band apparent magnitude (cmodelmag) vs redshift for the entire spectroscopic sample with the remainder sample in red.

described in Section 3.6; all visual redshifts were found to be in agreement with the automated classification. There were 65 objects with `ZWARNING` not equal to zero in the sample of 3879 objects. Manual inspection of these objects revealed that the SDSS pipeline redshift estimates were correct for 21 objects even though the `ZWARNING` flag had been set; these spectra were also included in the sample for a total of 3835 objects. Some objects were observed spectroscopically in both SDSS and BOSS. In these cases of repeat observations, we refer to the BOSS spectrum as the primary redshift if the fiber was positioned at the center of the galaxy due to the larger wavelength coverage of BOSS. There were 282 objects that were observed with both surveys in which the BOSS `ANCILLARY_TARGET1` was set to 39, indicating that the fiber was positioned at the location of variability. In these cases, we use the SDSS spectrum to determine the host galaxy redshift. For the final sample of 457 candidates with redshifts obtained by both BOSS and SDSS, there is only one candidate with redshift disagreement, defined as $|(z_{BOSS} - z_{SDSS})/(1 + z_{BOSS})| > 0.005$, as shown in Figure 3.5 further demonstrating confidence in the SDSS redshifts.

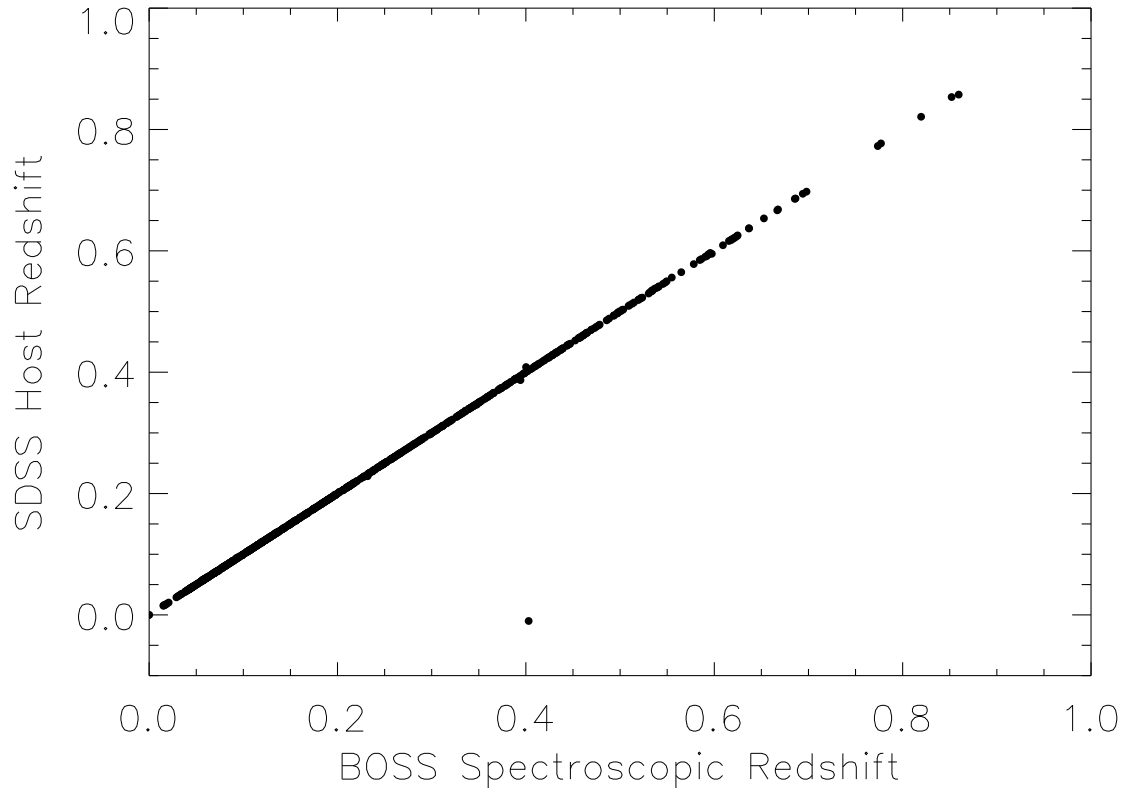


Figure 3.5 A comparison between the BOSS spectroscopic redshift and the SDSS spectroscopic redshift.

3.8 Host Galaxy Ambiguity

Even with both methods of host galaxy selection described in Section 3.5, there are always cases of host galaxy ambiguity. These cases can be identified when both the SN and associated host galaxy have discrepant spectroscopic redshifts. Because of the difficulty in obtaining conclusive redshifts independently for the host galaxy and SN, there is only one instance of such a discrepancy in this sample. We show the imaging and spectrum of SN 2005ey (CID 2308) in Figure 3.6 as the sole confirmed discrepancy. The same object shown in the red box was determined as the host galaxy of SN 2005ey from the visual inspection of DR7 and an automated method using DR8. The SN candidate has a redshift of 0.148 from the SN spectrum and the host galaxy of this candidate has a redshift 0.272. While this SN appears to visually be hosted by this galaxy, the redshift difference between the SN spectrum and the galaxy spectrum indicate that it is a background galaxy. While

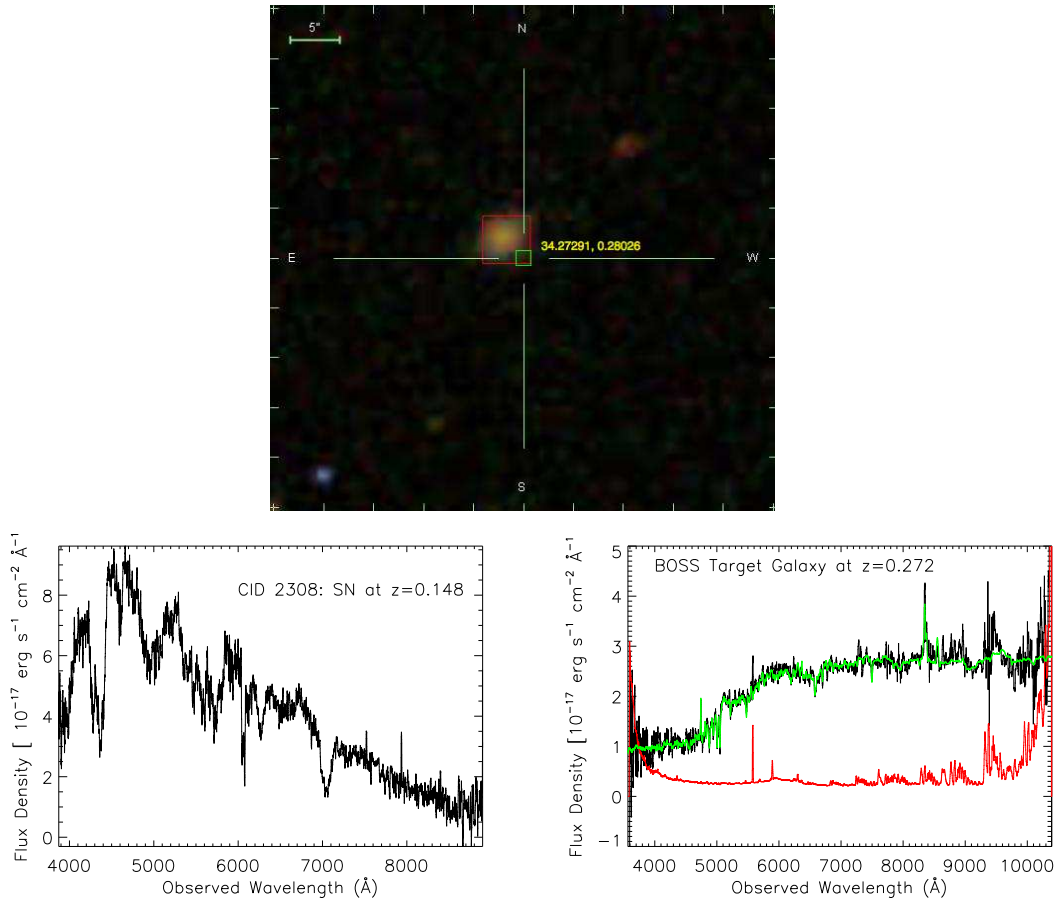


Figure 3.6 Example of a misidentified host galaxy. Top: DR9 image at the location of CID 2308, showing the SN location marked by cross-hairs and boxed in green along with the BOSS targeted galaxy boxed in red. Middle: The SN spectrum for 2308 with redshift 0.148. Bottom: The host galaxy spectrum for 2308 with a template spectrum of redshift 0.272 shown in green and the error spectrum shown in red, all with 10 pixel smoothing.

we can not quantify the full effect, we point out that the problem is not only present in ground based data, but also exists in HST data. In a survey of galaxy clusters, a SN with redshift $z = 0.98$ was discovered in the foreground of a large spiral galaxy at $z = 1.09$ that was mistakenly identified as the host. Further examination of the deep HST images revealed a very faint galaxy that was not deblended from the background spiral. While no redshift was ever determined for the faint galaxy, it is believed to be the true host of SCP06C1 (Barbary et al. 2012a).

CHAPTER 4

PERFORMANCE OF PHOTOMETRIC SN CLASSIFICATION

The SDSS imaging on Stripe 82 led to precise photometry in *ugriz* and photometric redshift estimates of the SDSS SN host galaxies released as part of DR8 (Aihara et al. 2011). The redshifts were determined using the DR7 photometric redshift code `PHOTOZ` which uses the approach of Csabai et al. (2007). In `PHOTOZ`, the 100 nearest neighbors of each galaxy are examined in a color-color space populated by the 900,000 spectroscopically confirmed SDSS galaxies. The redshift is estimated by evaluating the position of the photometric galaxy on the best-fit four color-redshift hyperplane derived from the 100 nearest neighbors. In Figure 4.1, we compare the photometric redshift estimates of SDSS-II SN host galaxies with spectroscopic redshifts from BOSS. The RMS (defined as $\sigma/1+z$) between the spectroscopic and photometric redshift estimates using host galaxy photometry is 0.034 after removing 194 objects (8%) that have redshift differences $> 3\sigma$ and are characterized as catastrophic failures. In what follows, all SDSS and BOSS spectroscopic redshifts are used, regardless of whether the photometric redshift was a catastrophic failure.

With precise spectroscopic host galaxy redshifts, we are able to simultaneously assess the photometric typing of SNe and determine the properties of the host galaxies. Objects typed as SN Ia in the final Hubble Diagram of the SN cosmology analysis (Campbell et al. 2013) are flagged with the keyword *Campbell2012* in the SDSS-II SN Data Release. In this section, we update the SN photometric typing as reported in the SDSS-II SN Data Release. We type each SN using the spectroscopic redshift as a prior, compare the performance of three different classification techniques, and assess performance of photometric classification with varying data quality.

⁷The results reported in this chapter have been submitted to the Astronomical Journal, referenced as “Host Galaxy Spectra and Consequences for SN Typing From The SDSS SN Survey,” Olmstead, M.D. et al., 2013, submitted to AJ, arXiv:6818.

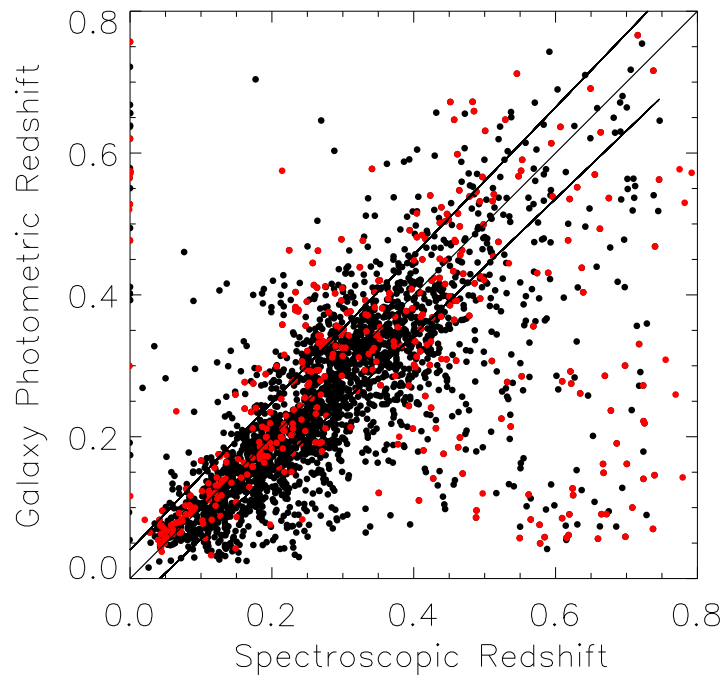


Figure 4.1 A comparison between the BOSS spectroscopic redshift and the galaxy photometric redshift. The red points are from the remainder sample. The solid lines are $z \pm \sigma/(1+z)$.

4.1 Photometric Typing with SDSS and BOSS Redshifts

In Section 3.2, a flat redshift distribution was used as a prior for the photometric typing of SN light curves; here we use the host galaxy spectroscopic redshift as a prior to provide new photometric typing of the candidates. As before, we use PSNID to perform Bayesian photometric classification. In comparing the typing of SN light curves using a flat redshift prior to the results using a spectroscopic redshift, we use the following notation. Using only photometric information and a flat redshift prior, a Bayesian probability of the candidate being a SNe Ia is reported as P_{Ia} , similarly for Type Ib/c (P_{Ibc}) and Type II (P_{II}). The same method is performed while using the spectroscopic redshift and recorded as PZ_{Ia} , PZ_{Ibc} , and PZ_{II} , respectively.

The updated PSNID probability for each transient identified as either a SN Ia or core-collapse in Table 3.2 is found in the online tables; the typing of a representative subsample is shown in Table 4.1 for the six candidates displayed in Figure 3.2. As shown in Figure 4.2, the probability values for the entire sample computed by PSNID tend to cluster around the most likely SN type. For this reason, we initially classify a SN based on the highest P value; for example, an object is considered a SN Ia if the probability of being Ia is higher than both the probability of being Ib/c and core-collapse. When using a flat redshift prior, there are 2492 candidates that have $P_{Ia} > P_{Ibc}$ and $P_{Ia} > P_{II}$; these candidates are denoted “B Ia.” When using a spectroscopic redshift prior, there are 2696 candidates that have $PZ_{Ia} > PZ_{Ibc}$ and $PZ_{Ia} > PZ_{II}$; these candidates are denoted “BZ Ia.”

We also test two additional classification techniques. The first of these is the nearest neighbor (NN) approach of S13. In this method, the candidates are compared to a simulated training set in multidimensional SN parameter space that includes extinction, light curve shape, and redshift. Different SN types cluster in different sections of this parameter space. A candidate is given a probability of being a SN Ia (P_{NN-Ia} or P_{NNZ-Ia} for flat and spectroscopic redshift priors, respectively) by counting the number of SNe Ia within a certain distance in this parameter space normalized by the total number of SNe within that distance in parameter space. There are 1090 likely SNe Ia (NN Ia) and 1056 likely SNe Ia (NNZ Ia) when using redshift priors and flat redshift priors, respectively. The total number of likely SN Ia is fewer than half those included in the PSNID case; this apparent discrepancy is due to the stringent requirements on light curve coverage and on the quality of fit.

In the third classification technique, we categorize the objects as likely Type Ia, Ib/c or II SNe using the same criteria as S13 and refer to this selection as the full photometric classification. A full photometric SNe Ia is subject to the nearest neighbor classification with additional light curve quality restrictions. A full photometric SN Ia must have variability in only one year, $PZ_{Ia} > PZ_{Ibc}$, $PZ_{Ia} > PZ_{II}$, $PZ_{NN-Ia} > PZ_{NN-Ibc}$, $PZ_{NN-Ia} > PZ_{NN-II}$, at least 10 nearest neighbors in parameter space, a χ^2 fit probability ≥ 0.01 , a light curve containing at least one epoch within five days rest-frame of peak, and at least one epoch between five and 15 days rest-frame after peak.

Table 4.1. SN Classification

CID	PZ_{Ia}	PZ_{Ibc}	PZ_{II}	P_{Ia}	P_{Ibc}	P_{II}
20259	0.999	0.000	0.0003	1.00	0.00	0.00
20953	0.998	0.0007	0.0017	0.956	0.0385	0.0067
13195	0.000	1.00	0.000	0.000	1.00	0.000
17414	0.954	0.046	0.000	0.536	0.465	0.000
20768	0.993	0.007	0.000	0.967	0.033	0.0001
3562	1.00	0.000	0.000	0.000	0.000	1.00

^aSN probabilities for the six spectra in Figure 3.2.

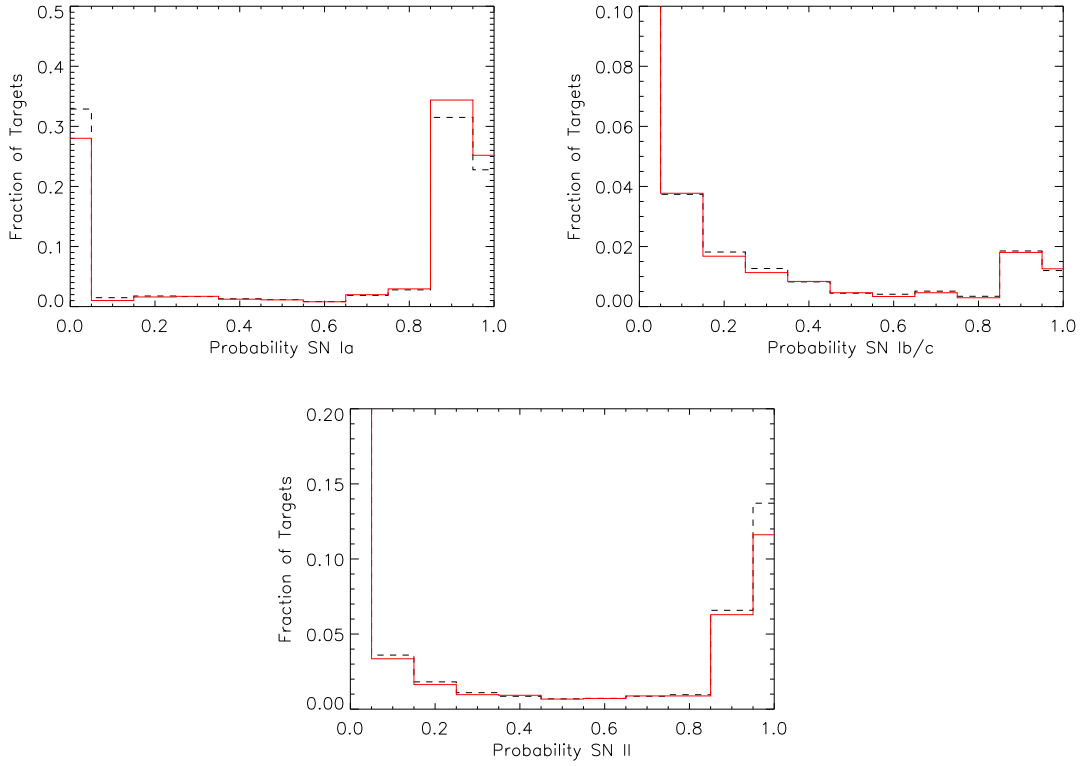


Figure 4.2 Distribution of Bayesian probability of being a SN Ia (core-collapse SN) using the host galaxy redshift as a prior. The black (dashed line) is the entire observed sample including the remainder targets and red (solid) is for the observed sample excluding the remainder sample. As expected, when the remainder sample is not used, there is a higher probability of a candidate being a SNe Ia.

Similarly, a full photometric core-collapse SNe must have variability in only one year, $PZ_{Ibc} > PZ_{Ia}$ or $PZ_{II} > PZ_{Ia}$, $PZ_{NN-Ibc} > PZ_{NN-Ia}$ or $PZ_{NN-II} > PZ_{NN-Ia}$, and at least 10 nearest neighbors in parameter space. Unlike the first two classification techniques, we do not report probabilities associated with each classification here. Instead, we simply refer to the final classification as “photometric Ia” or “photometric CC” for typing without redshifts. When adding a redshift, we report the classification as “photometric Z Ia” and “photometric Z CC.” Employing the photometric classification technique, we find 1038 photometric SNe Ia and 1021 photometric Z SNe Ia.

Of the 518 spectroscopically-confirmed SNe Ia from SDSS-II, 320 objects have SDSS or BOSS host galaxy spectra; 83.4%, 54.4%, and 53.1% are classified as SNe Ia using each BZ IA, NNZ IA, and the full photometric classification. While at first these numbers appear low, this result is not surprising because many SNe candidates were targeted for spectroscopic confirmation at the beginning or end of each season and had poor light curve coverage for photometric typing. When one examines spectroscopically-confirmed SNe Ia with at least three epochs of $S/N > 3$ in *gri* and $S/N > 5$ for at least one epoch in *gri*, 10 spectroscopically-confirmed SNe Ia are removed from the sample of 320. Using the remaining 310, the three techniques classify 82.9%, 54.8%, and 53.5% of the spectroscopically-confirmed SNe Ia as SNe Ia, respectively.

Finally, we examine AGN activity in the SDSS and BOSS spectra of the photometric Z SN Ia hosts. We find that 22 of these host galaxies are classified in `idlspec2d` as as likely AGN, likely due to broadline emission features such as MgII or H β . Of these, nine were identified in Table 3.2 as high probability SNe Ia, six as low probability SNe Ia, and seven from the remainder sample. Of these, nine high or low probability SN Ia and three from the remainder sample were within 0.3'' of the center of the host. We conclude that the variation is most likely due to AGN activity rather than SN. There are five SNe Ia hosted in quasars that are separated by more than 1.0'' from the center of the host. These numbers are small compared to the overall sample.

4.2 Comparison of Classification Techniques

As shown in Table 4.2, each SN candidate has been assigned a type using three different classification schemes. While it is not possible to do a full analysis of purity or completeness on each of these classification schemes due to the lack of complete spectroscopic classification, we evaluate the performance of each by comparing the results with and without spectroscopic redshifts. One may consider the most robust technique to be the one that produces consistent typing with and without using redshift priors. We search for signs of contamination in each classification scheme by examining the number of objects classified as a SN Ia without redshift and classified as a core-collapse with redshift. We search for signs of completeness by examining the number of objects classified as a SN Ia with redshift that were not identified as a SN Ia without redshift. The comparison performed here can be considered a recipe to filter samples into higher purity for any classification scheme that may be used in the future.

Table 4.2. Classification Statistics

Class	Number
B Ia	2492
B IBC	175
B II	918
NN Ia	1090
NN Ibc	103
NN II	1078
Photometric Ia	1038
Photometric CC	1077
BZ Ia	2696
BZ Ibc	153
BZ II	665
NNZ Ia	1056
NNZ Ibc	138
NNZ II	763
Photometric Z Ia	1021
Photometric Z CC	215

In the PSNID sample, 2272 objects were consistently classified as B Ia and BZ Ia, while 2696 objects were classified as BZ Ia. We therefore define the completeness as 84.3%. The completeness for the nearest neighbor and full classification are 90.5% and 91.0%, respectively.

The consistency of classification for each technique relative to the total number of SNe Ia classified with redshift as a prior are shown in Table 4.3. In the PSNID approach, we count 220 objects that were classified as B Ia that were later classified as BZ Ibc or BZ II. In total, 2492 transients were classified B Ia, corresponding to a contamination of 8.8%. As shown in Table 4.3, the same analysis reveals 12.3% and 12.1% contamination in the nearest neighbor and full classification results, respectively.

The contamination in the PSNID approach appears to be the lowest of the three techniques. As described in Section 4.1, this result should be guarded with caution because the total number of B Ia and BZ Ia appears artificially increased due to the more stringent requirements on the light curve quality and on the fit-probability placed on the other two classification schemes. The nearest neighbor approach performs comparably to the full photometric classification. However, the full photometric classification approach has the higher percentage of completeness, the lower level of contamination, and the smaller number of SN Ia. For these reasons, the full photometric technique appears to be more restrictive and will be used for the remainder of the dissertation.

Table 4.2 demonstrates the significance of redshift on photometric classification. The redshift decreases the number of core-collapse SN, 918 B II objects and only 665 BZ II objects. While the photometric Ia and photometric Z Ia samples are nearly the same size, 1038 and 1021 objects respectively, the photometric CC and photometric Z CC samples are significantly different, 1077 and 215 objects, respectively. The addition of spectroscopic redshift helps control the contamination.

Figure 4.3 demonstrates the increase in total number of SNe Ia using the full photometric classification relative to the spectroscopically-confirmed sample. The photometric Ia sample used here includes only those candidates that are photometric Z Ia. At low redshift ($0 < z < 0.1$), the photometric Z Ia sample is 61.6% larger than the photometric Ia sample. At higher redshifts ($0.2 < z < 0.4$), the sample of photometric Z Ia sample is 14.4% larger.

4.3 Effects of Data Quality on Contamination and Completeness

We examine contamination and completeness of the full photometric classification technique as a function of data quality. We evaluate the performance on subsets of data selected on the minimum S/N, total number of data points on the light curve, and light curve coverage relative to maximum SNe Ia luminosity. In the first series of tests, we require that at least one exposure meet minimum S/N measurements in each of *gri*. We refer to this restriction as the “S/N” cut. In the second series of tests, we require a minimum number of epochs to meet the condition $S/N > 3$ in each of *gri*. We refer to these subsamples as “Number of epochs.” In the final series of tests, we

Table 4.3. Typing Approach Contamination and Completeness

	PSNID	Nearest Neighbor	Full Classification
Contamination	220 8.2%	134 12.3%	126 12.1%
Completeness	2696 84.3%	1056 90.5%	1002 91.0%

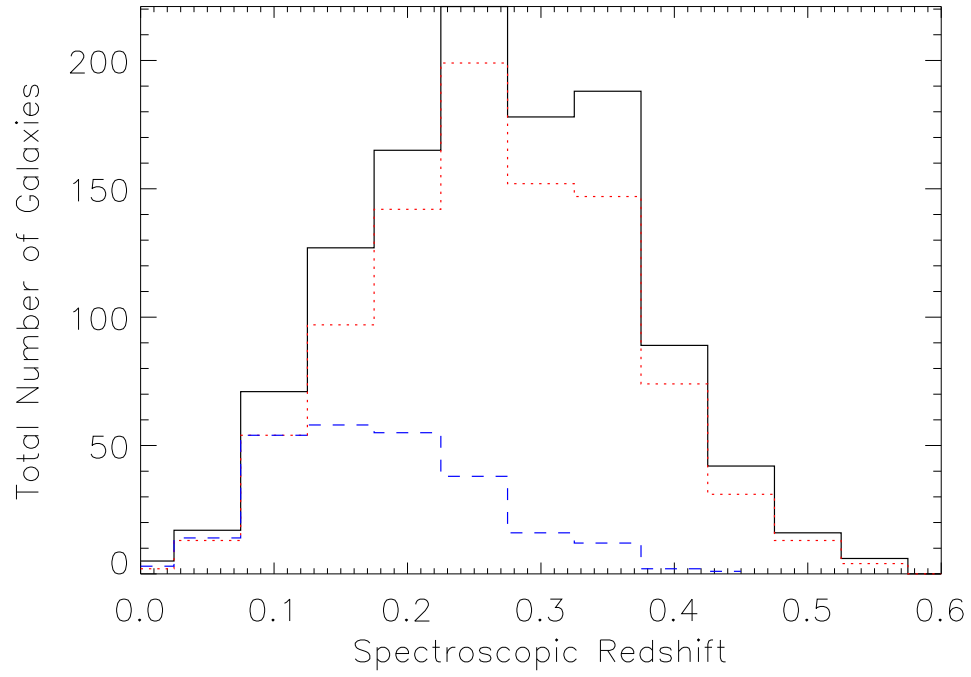


Figure 4.3 The redshift distribution of galaxies hosting SNe Ia in redshift bins of 0.05. The black (solid) curve is for candidates typed as SNe Ia with spectroscopic redshift, the red curve (dotted) is for photometric SNe Ia and the blue (dashed) curve is for the spectroscopically confirmed sample of SNe Ia.

examine the number of SNe Ia in which at least one $S/N > 3$ epoch is separated by a finite amount of time from maximum light. We refer to these as “ Δt .”

The contamination and completeness fraction for each of these data quality cuts are shown in Table 4.4. The contamination decreases from 0.126 to 0.108 when imposing the most restrictive cuts on S/N . As shown in the final row of Table 4.4, the contamination decreases from 0.121 to 0.095 when requiring that a SN light curve have both early time coverage and late time coverage. Requiring additional epochs with $S/N > 3$ appears to have the largest impact, reducing contamination from 0.126 to 0.090. Similarly, requiring 10 epochs leads to the largest improvement in completeness, although at a cost of sacrificing 85% of the total sample. One may argue the best compromise requires early and late time coverage, leading to the second best statistics on contamination and completeness while only losing half of the SNe Ia.

Somewhat surprisingly, even SNe that meet the most restrictive conditions outlined in Table 4.4 can be misclassified. An example is CID 15486 as shown in Figure 4.4. This SN has 11 epochs at $S/N > 3$, coverage as early as 14 days before peak luminosity and as late as 18 days after peak luminosity. The SN is classified photometric Ia and photometric Z CC, likely due to redshift uncertainty. The photometric estimate of the best-fit SN Ia redshift is $z = 0.350$ while the host galaxy spectrum revealed a redshift of $z = 0.116$. This large discrepancy in typing is another example of the importance of host galaxy redshift.

Table 4.4. Data Quality Effects of Full Photometric Classification

	Contamination	Total Number in photometric classified sample	Completeness	Total Number in redshift classified sample
No additional quality cuts	0.121	1038	0.910	1002
S/N > 3	0.116	983	0.910	955
S/N > 5	0.114	874	0.920	841
S/N > 10	0.108	370	0.940	351
3 epochs	0.111	941	0.930	804
5 epochs	0.0105	589	0.947	556
7 epochs	0.097	359	0.956	339
10 epochs	0.090	156	0.979	145
$\Delta t < -5$ d	0.100	683	0.958	642
$\Delta t > 15$ d	0.099	667	0.960	626
$\Delta t < -5$ d, and not $\Delta t > 15$ d	0.116	138	0.931	131
$\Delta t > 15$ d, and not $\Delta t < -5$	0.115	122	0.939	115
$\Delta t < -5$ d and $\Delta t > 15$ d	0.095	545	0.965	511

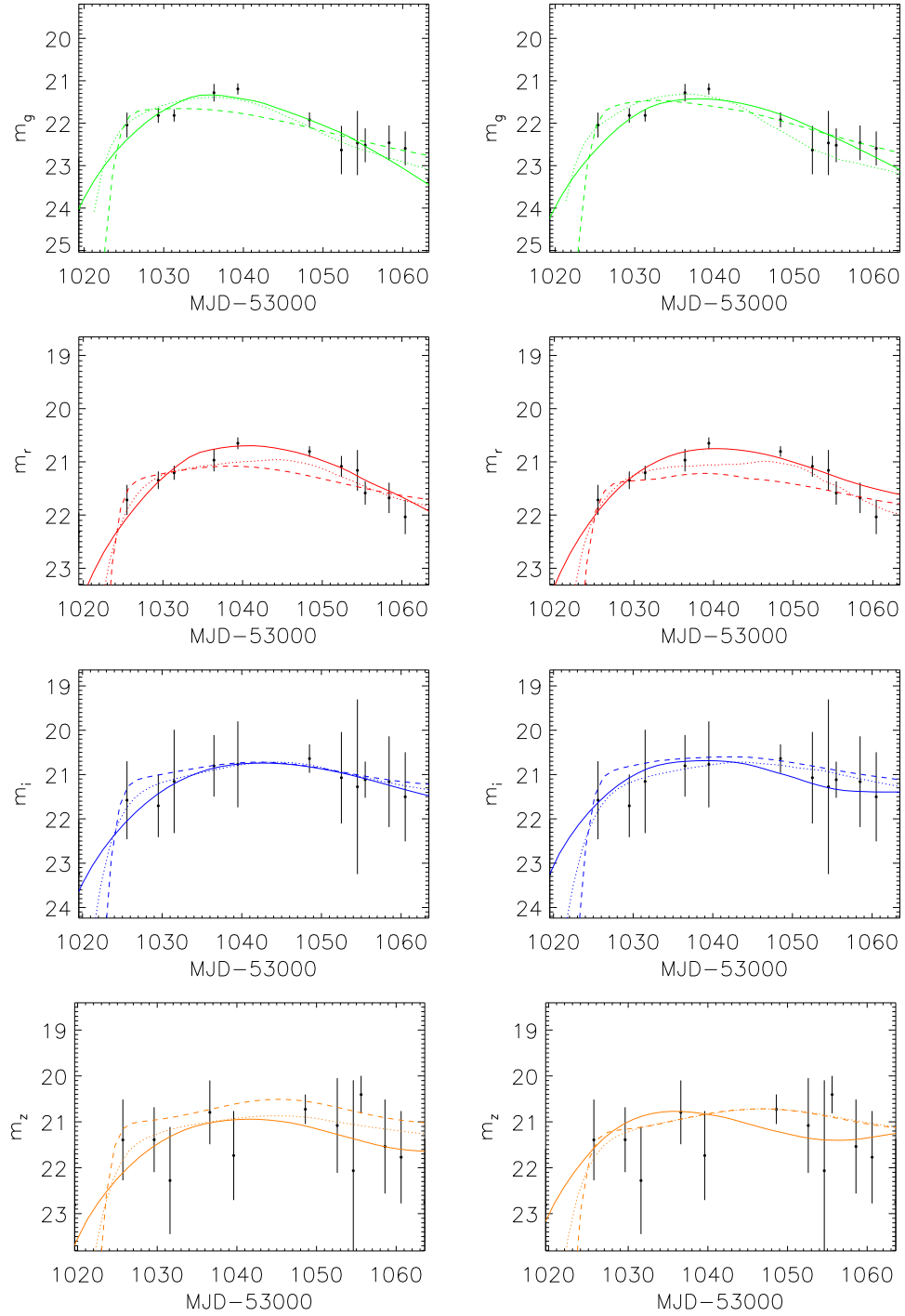


Figure 4.4 Example of the light curves for one SN candidate at $z_{\text{spec}} = 0.116$ that is in the contamination sample when there are at least 10 epochs. The solid line shows the best fit SNe Ia template, the dotted line shows the best fit Ibc template, and the dashed line shows the best fit SNe II template. The left four plots show best fit templates when using a flat redshift prior and the right four plots when the spectroscopic redshift is used as part of the classification.

CHAPTER 5

GALAXY PROPERTIES

In this section, we present the statistics of the host galaxies divided into two categories, SNe Ia and core-collapse, based on final photometric typing using the full photometric nearest neighbor technique. The redshift and apparent `cmodel` magnitude distribution of host galaxies of likely Type Ia and likely core-collapse SNe are shown in Figure 3.3. The median redshift of the galaxies of the combined SN Ia sample of SDSS and BOSS is 0.29. The median redshift of the core-collapse sample is 0.21. Similarly, the apparent `cmodel` magnitude distributions have a median of 20.6 for the host galaxies of the SN Ia sample and 20.2 for the core-collapse sample. With photometry, redshifts, and spectra, we report the stellar mass, star formation, absolute magnitudes, velocity dispersion, and $H\beta$ equivalent linewidths for all host galaxies. With this information, one can perform analysis of the correlation between SN light curve properties and host galaxy properties. We conclude the section by performing simplified analysis of these correlations as a demonstration of the power of the data.

5.1 Photometric Galaxy Properties with SDSS and BOSS Redshifts

We examine the stellar mass and specific star formation rates (sSFR) of all photometric Z Ia and all photometric Z CC host galaxies using the spectroscopic redshift and the SDSS imaging photometry. To determine the galaxy properties using only photometry and spectroscopic redshift, we have chosen to use the “Granada FSPS” product (Montero-Dorta et al. in preparation). These fits are based on the publicly available Flexible Stellar Population Synthesis (FSPS) code (Conroy et al. 2009) and were computed for several models of stellar formation history, dust attenuation, and initial mass function (IMF). The Granada FSPS fits to all galaxies in SDSS and BOSS will be released as part of DR10 in Summer 2013. At that time, these data may be found in the galaxy product⁹ at

⁸The results reported in this chapter have been submitted to the *Astronomical Journal*, referenced as “Host Galaxy Spectra and Consequences for SN Typing From The SDSS SN Survey,” Olmstead, M.D. et al., 2013, submitted to *AJ*, arXiv:6818.

⁹<http://data.sdss3.org/sas/dr10/boos/spectro/redux/galaxy>

the SDSS-III Science Archive Server (SAS). The best fits to the BOSS data will be recorded in the file named “v1.0/v5.5.12/granada_fsps_krou.wideform_nodust-v5.5.12.fits.gz” and the best fits to the SDSS data will be recorded in the file named “v1.0/dr8/granada_fsps_krou.wideform_nodust-26.fits.gz.” One can match the results of Granada FSPS to the SDSS-II SN Data Release by matching on the keywords plate, fiberid, and mjd, or by matching on SPECOBJID.

The Granada FSPS stellar masses reported in this dissertation for the host galaxies were obtained assuming no dust and the Kroupa (2001) IMF. The computation was performed using an extensive grid of models, with varying formation times, e-folding times (τ) and metallicities. In addition, we report absolute magnitudes (K+E corrected to $z = 0.55$) and estimated values for other stellar population properties, such as sSFR. Table 5.1 provides a summary of stellar mass, sSFR, and r -band absolute magnitude for the sample described in this dissertation.

In Figure 5.1, we present the distribution of the stellar mass and sSFR for the photometric Z Ia and photometric Z CC host galaxy samples. The SNe Ia have host galaxies with a mean $\log(\text{mass})$ equal to 10.7 ± 0.6 and the core-collapse sample has mean 10.4 ± 0.6 . For this analysis, we consider all galaxies with $\text{sSFR} < -3(-6) \log(\text{Gyr}^{-1})$ to be likely nonstar forming galaxies. By this definition, 49.6% (21.2%) of SNe Ia are found in a nonstar forming galaxy and 32.3% (13.7%) of core-collapse are found in a nonstar forming galaxy.

Figure 5.2 shows the distribution of the r -band absolute magnitude between galaxies hosting SNe Ia and core-collapse SNe. The distribution of galaxies hosting SNe Ia has median r -band absolute magnitude of -20.1 and RMS of 0.9. The distribution of galaxies hosting core-collapse has median r -band absolute magnitude of -19.9 and RMS of 1.1. Figure 5.3 shows the absolute magnitude of the host galaxies as a function of redshift.

5.2 Galaxy Properties from SDSS and BOSS Spectra

The SDSS and BOSS spectroscopy offers us the opportunity to derive galaxy properties directly from the host galaxy spectra. This information is provided for the first time in DR9 for BOSS data using two different algorithms.

The first algorithm is the Portsmouth Stellar Kinematics and Emission Line Fluxes [hereafter T12; Thomas et al. (2012)]. The second algorithm is the Wisconsin PCA method (Chen et al. 2012). In DR10, both the Portsmouth Stellar Kinematics and Emission Line Fluxes and the Wisconsin PCA computations will be applied to SDSS spectra to provide a consistent catalog of spectroscopic galaxy properties across SDSS-I, -II, and -III.

T12 derive emission line properties using stellar kinematics based on the Gas and Absorption Line Fitting code (GANDALF v1.5; Sarzi et al. 2006). T12 simultaneously fit a stellar population model [hereafter M11; Maraston & Strömbäck (2011)] and Gaussian emission line templates to the galaxy spectrum to separate stellar continuum and absorption lines from the ionized gas emission.

Table 5.1. Summary of SN Ia Host Galaxy Properties

Redshift Range	#	Median Mass	RMS Mass	Median sSFR	Median M_r	RMS M_r	Median Velocity Dispersion (km s ⁻¹)	RMS Velocity Dispersion (km s ⁻¹)	Median H β Equivalent Linewidth (Å)
		(log(M))	(log(M))	log(Gyr ⁻¹)					
0.00–0.05	10	10.7	0.7	-4.6	-19.1	1.1	113.9	51.1	1.0
0.05–0.10	33	10.4	0.5	-1.7	-19.0	1.2	82.1	47.2	4.4
0.10–0.15	60	10.7	0.7	-1.7	-19.5	1.2	102.7	63.7	3.1
0.15–0.20	82	10.6	0.6	-1.6	-19.4	1.0	100.3	66.6	4.4
0.20–0.25	106	10.6	0.7	-1.4	-19.7	1.0	110.6	76.4	3.9
0.25–0.30	170	10.6	0.6	-1.4	-19.8	0.9	112.2	75.0	2.9
0.30–0.35	139	10.8	0.6	-1.6	-20.1	0.8	129.8	71.5	2.4
0.35–0.40	137	10.8	0.5	-1.6	-20.3	0.8	115.4	68.8	2.1
0.40–0.45	77	10.9	0.6	-1.3	-20.4	0.8	135.3	86.7	4.6
0.45–0.50	34	10.9	0.5	-1.4	-20.6	0.7	146.1	90.3	2.3
0.50–0.55	15	11.0	0.6	-4.2	-20.5	0.7	208.3	97.4	1.0
0.55–0.60	2	10.7	0.6	-3.9	-20.9	0.5	482.6	429.0	1.4

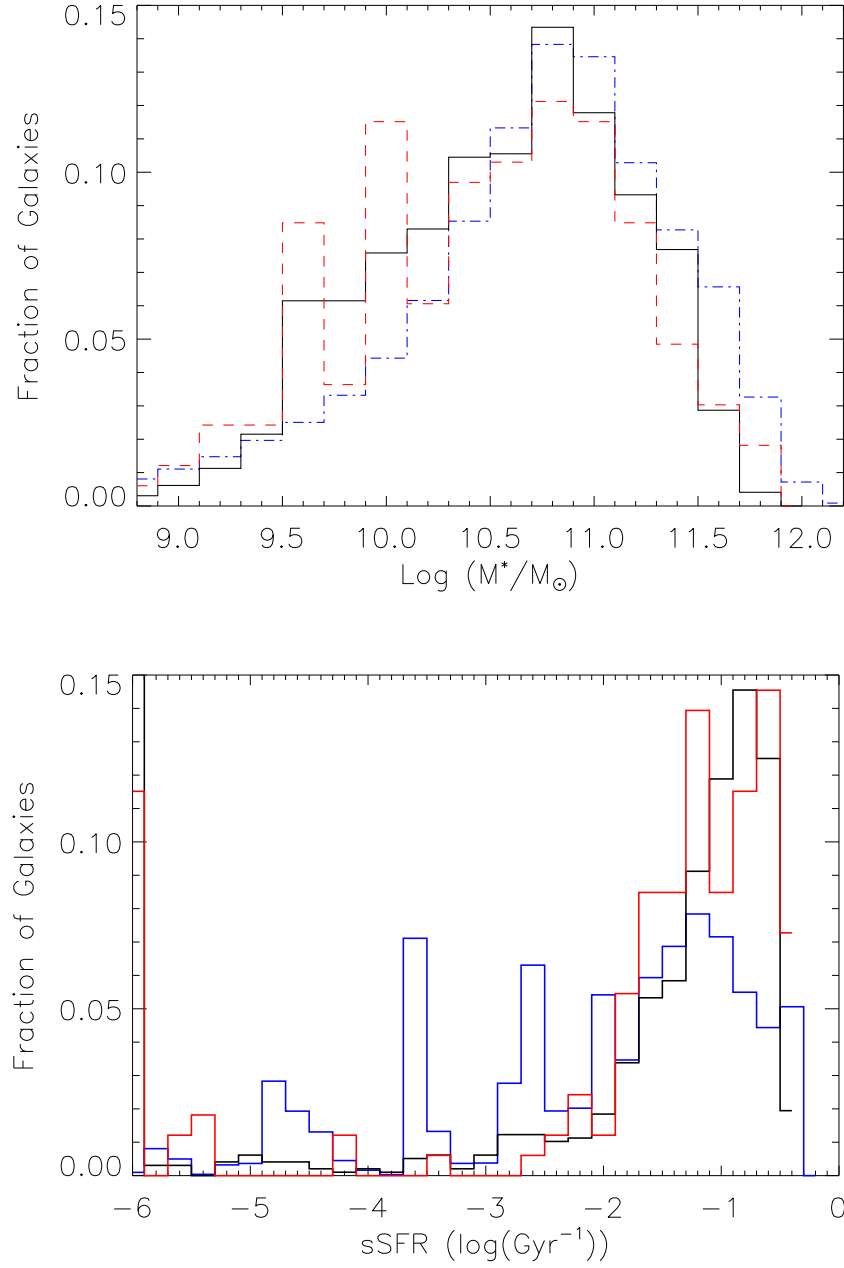


Figure 5.1 Distribution of stellar mass and sSFR for the SNe Ia and core-collapse samples. **Top:** The stellar mass distribution of galaxies hosting SNe Ia in solid and core-collapse in dashed using spectroscopic redshift priors. The entire SDSS DR8 galaxy sample is shown in blue. **Bottom:** The distribution of the sSFR for the galaxies that hosted SNe Ia (solid) and core-collapse (dashed) SNe. The entire SDSS DR8 galaxy sample is shown in blue. The grouping of galaxies shown with sSFR = -6 are simply galaxies in which the fit was not allowed to go to smaller values of sSFR.

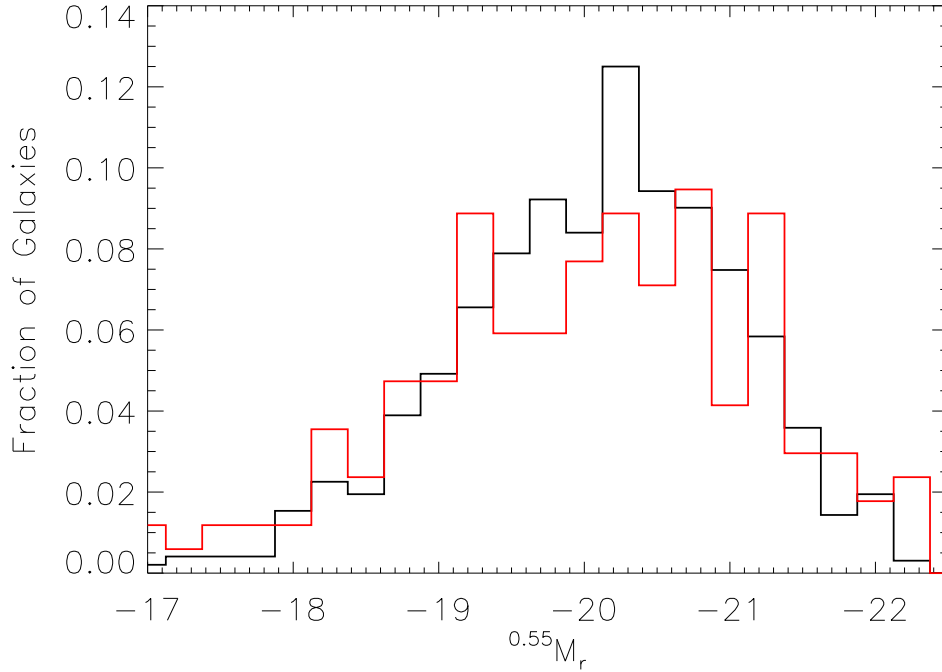


Figure 5.2 The r -band absolute magnitude (derived from `cmodelmag`) distribution for galaxies hosting SN Ia (solid) and core-collapse SN (red, dashed). The information in DR10 is sufficient for one to generate similar figures for $ugiz$.

The line-of-sight velocity distribution is fit using the Penalized PiXel Fitting code (pPXF; Cappellari & Emsellem 2004) code.

The Wisconsin PCA method decomposes each galaxy spectrum into best-fit PCA components derived from a library of model spectra based on the stellar population models of Bruzual & Charlot (2003). A probability distribution function is built from the composite PCA fit to estimate stellar masses and velocity dispersions for each galaxy. In DR10, the Wisconsin PCA code will be extended to include the M11 population models.

While both the Wisconsin PCA and T12 algorithms provide a characterization of the galaxy spectra for each SN host galaxy in our sample, we report only the T12 estimates here. We choose the T12 approach because it provides a more empirical measure of galaxy properties through characterization of emission lines and velocity dispersion. The Wisconsin PCA models were derived from specific models of stellar evolution and tested primarily on the more homogeneous galaxy samples in BOSS (Chen et al. 2012; Dawson et al. 2013) and may not be appropriate for the diverse population of galaxies presented here. The DR10 T12 fits will be found in the BOSS galaxy product in the file named “v1.0/v5.5.12/portsmouth_emlinekin_full-v5.5.12.fits.gz.” The fits to the SDSS data will be found in the file “v1.0/dr8/portsmouth_emlinekin_full-26.fits.gz.” As described

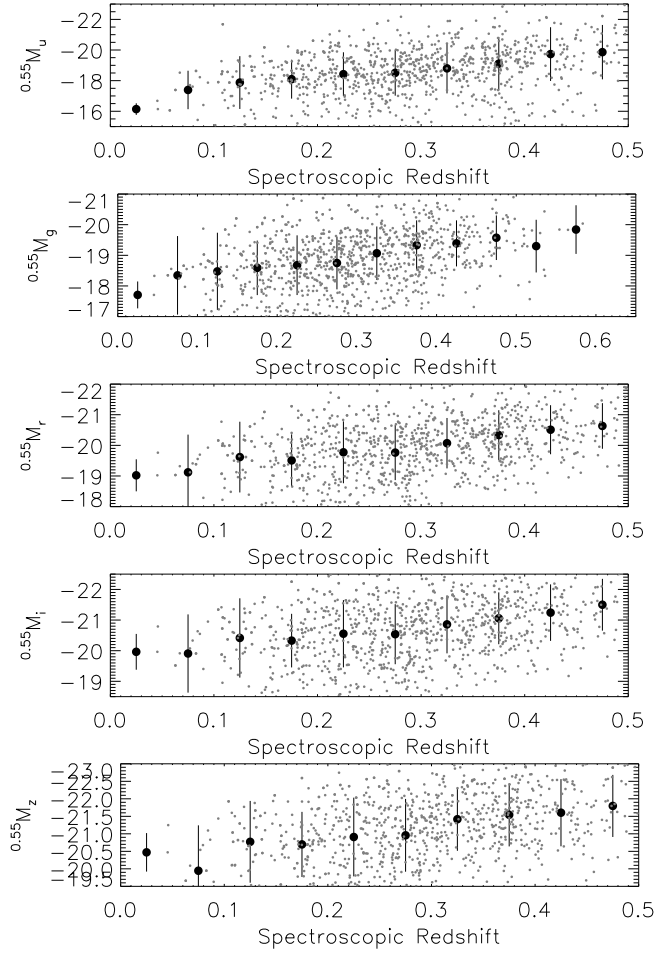


Figure 5.3 The absolute magnitudes of the SN Ia host galaxy sample by filter. The scatter plot consisting of small dots describes each galaxy in the sample. The median value binned by redshift (intervals of $\Delta z = 0.05$) is shown by large filled circles with error bars representing the RMS within the bin.

in Section 5.1, the sample from the SN database can be matched to these files through use of the plate, fiberid, and mjd, or by matching on SPEC OBJID.

As before, we present a comparison of some statistics from the T12 fits for the photometric Z Ia and photometric Z CC host galaxy samples. Estimates of velocity dispersion and $H\beta$ equivalent linewidth can be used as proxies for galaxy mass and star formation history, respectively. We also present the distribution of stellar velocity dispersion and rest frame $H\beta$ equivalent linewidths for the entire sample of SN host galaxies in Figure 5.4 and Figure 5.5. The mean of $H\beta$ is 5.1 \AA with an RMS of 4.2 \AA . The velocity dispersion has mean 122 km s^{-1} with an RMS of 74 km s^{-1} . As before, we present the results of the SNe Ia and core-collapse populations separately using the final photometric classification. A summary of the SNe Ia host galaxy spectroscopic properties is included in Table 5.1.

5.3 Correlating SN Properties With Galaxy Properties

This large SN host galaxy sample can be used for a number of investigations of possible relationships between SN Ia light curve properties and host galaxy properties. Many previous studies have searched for a dependence of SN Ia rate and light curve properties on host galaxy mass and metallicity. Here we show general examples of how these investigations can be enhanced with this new sample of well-characterized SN Ia light curves and host galaxies.

The rate of SN Ia events per cosmological volume element has been shown to depend on both mass and star formation history (Scannapieco & Bildsten 2005). Studies of SN Ia rates have been performed at all redshifts with samples of various sizes and completeness (e.g., Dilday et al. 2010b; Barbary et al. 2012b). Recent analysis have been performed using the subsample of spectroscopically confirmed SDSS-II SNe combined with mass determined by photometry (342 total SNe Ia; Smith et al. 2012) and spectroscopy (53 total SNe Ia; Gao & J. 2013). In the top panel of Figure 5.1, we compare the distribution of 935 photometric Z Ia host galaxy masses to the nearly magnitude-limited sample of SDSS galaxy masses. Similarly, in the bottom panel of Figure 5.1, we compare the distribution of sSFR in those same 935 SN Ia host galaxies the sSFR in SDSS galaxies. While a detailed analysis requires a full reconstruction of the SDSS-II SN detection efficiency, one clearly sees trends towards production of SN in galaxies with lower mass and higher sSFR. The sheer increase in sample size relative to previous studies highlights the potential of using these results for improved rates analysis.

We next use the galaxy properties found in Sections 5.1 and 5.2 to examine the potential for future analysis on the relationship between host galaxy metallicity and SN Ia light curve properties. Previous analysis has been performed on smaller SN Ia samples using $H\beta$ and iron absorption strengths (Gallagher et al. 2008; Johansson et al. 2012; Hayden et al. 2013). The T12 algorithm produces estimates of emission line strengths for hydrogen, helium, nitrogen, oxygen, neon, sulfur, and argon, but does not fit absorption lines such as iron. However, the various line fits do allow

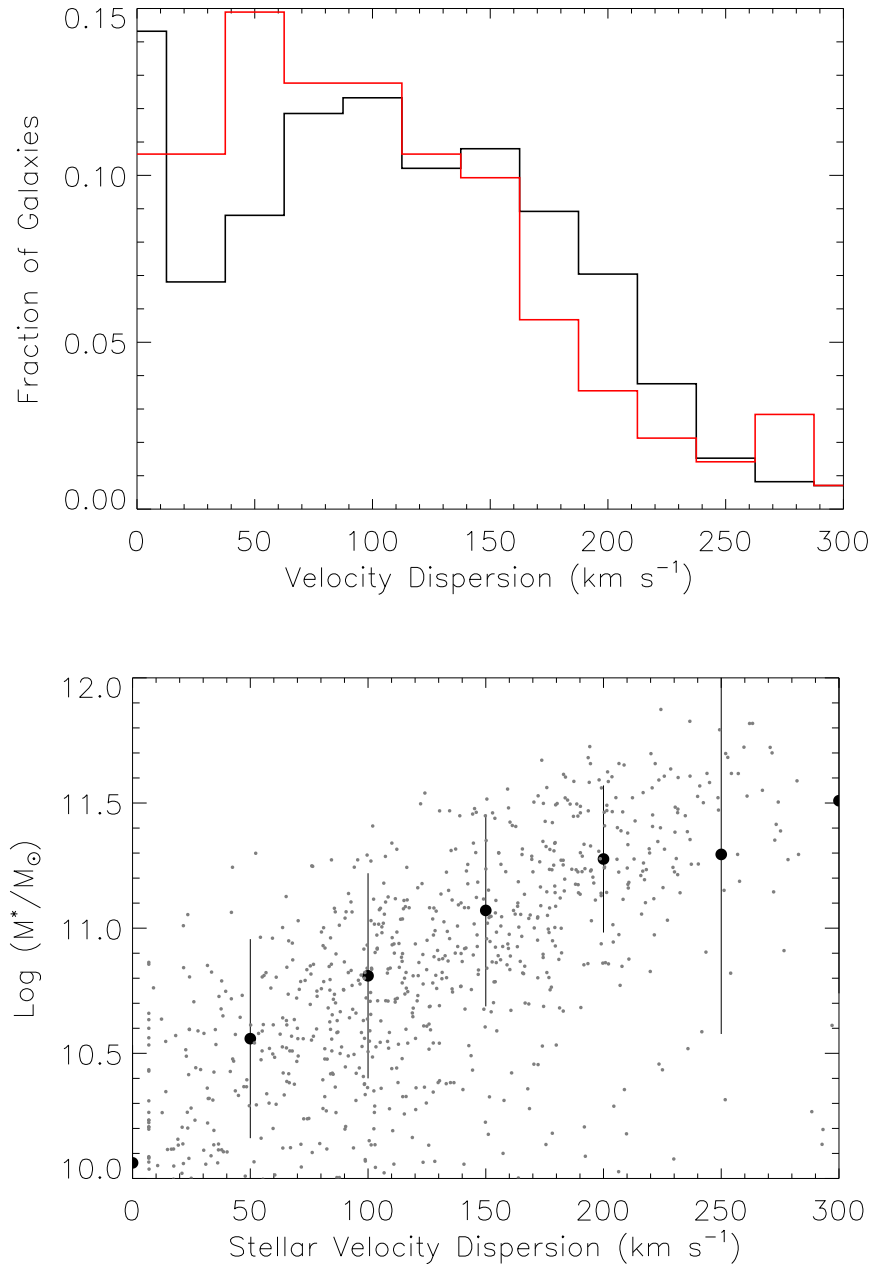


Figure 5.4 Stellar velocity dispersion distribution and photometric stellar mass estimates as a function of velocity dispersion. **Top:** The distribution of stellar velocity dispersion for galaxies hosting SNe Ia shown in solid black and those hosting core-collapse in dashed red. **Bottom:** The photometric stellar mass estimates as a function of velocity dispersion estimates for the sample of 842 likely SN Ia host galaxies. The median value binned by velocity dispersion (intervals of $\Delta\sigma = 50 \text{ km s}^{-1}$) is shown by large filled circles with error bars representing the RMS within the bin.

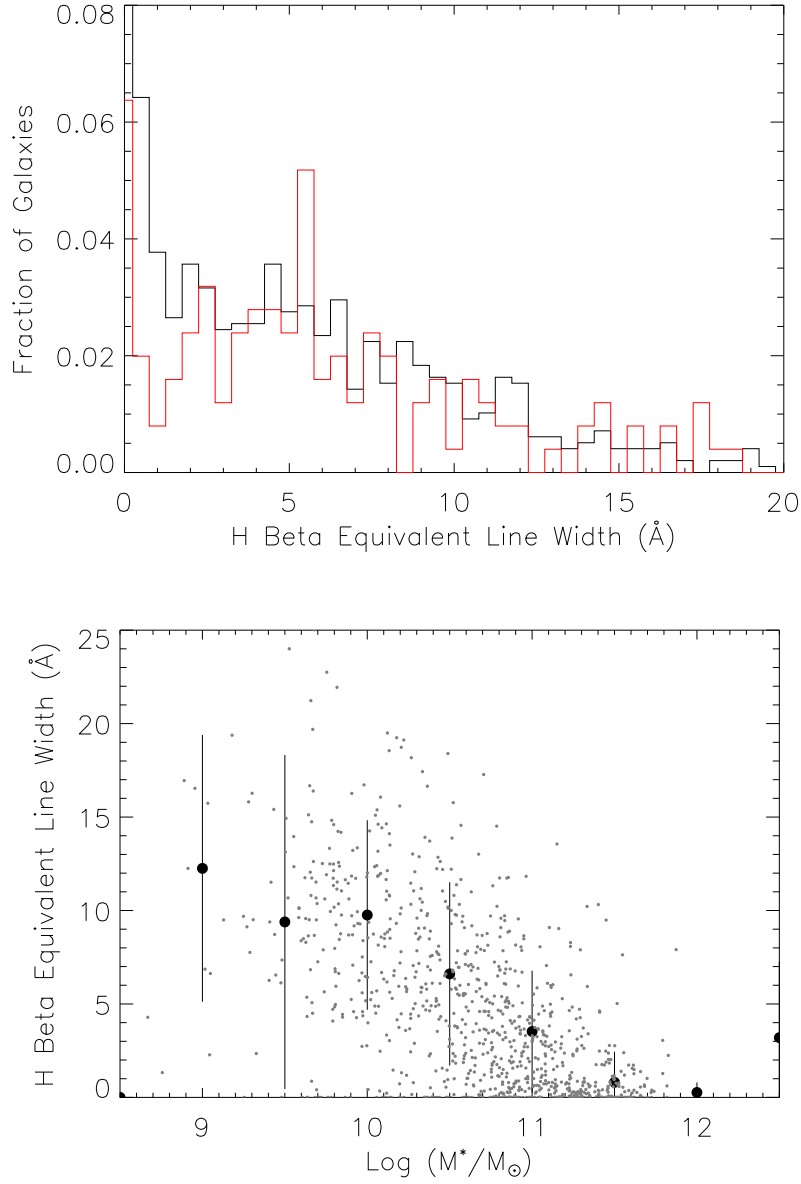


Figure 5.5 H β equivalent width distribution and H β equivalent width as a function of photometric stellar mass. **Top:** The distribution of H β equivalent width estimates for galaxies hosting SNe Ia shown in solid black and those hosting core-collapse in dashed red. **Bottom:** The spectroscopic H β equivalent width estimates as a function of photometric stellar mass estimates for the likely SN Ia host galaxies. The median value binned by stellar mass (intervals of $\Delta \log(m) = 0.5$) is shown by large filled circles with error bars representing the RMS within the bin.

computation of various proxies for gas phase metallicity. As an example, we here report an estimate of metallicity using one of the proxies derived from oxygen-nitrogen provided in Foster et al. (2012). We selected the method of Pettini & Pagel (2004) to determine the O3N2 ratio defined as

$$O3N2 \equiv \log \left(\frac{[OIII]\lambda 5006/H\beta}{[NII]\lambda 6583/H\alpha} \right). \quad (5.1)$$

This proxy is empirically calibrated to an O/H estimate of metallicity according the the following relation

$$\log(O/H) + 12 = 8.73 - 0.32 \times O3N2. \quad (5.2)$$

Using this relation, we present the metallicity as a function of stellar mass of the SNe Ia host galaxy sample in Figure 5.6. In the top panel, we present the overall distribution of metallicity in the SN Ia sample; the mean metallicity is 8.63 and the RMS dispersion is 0.15. In the bottom panel, we see a degeneracy between host galaxy metallicity and stellar mass; more massive galaxies also appear to have higher metallicity. This degeneracy will need to be taken into account in detailed analysis of the effects of host galaxy metallicity on SN Ia light curves.

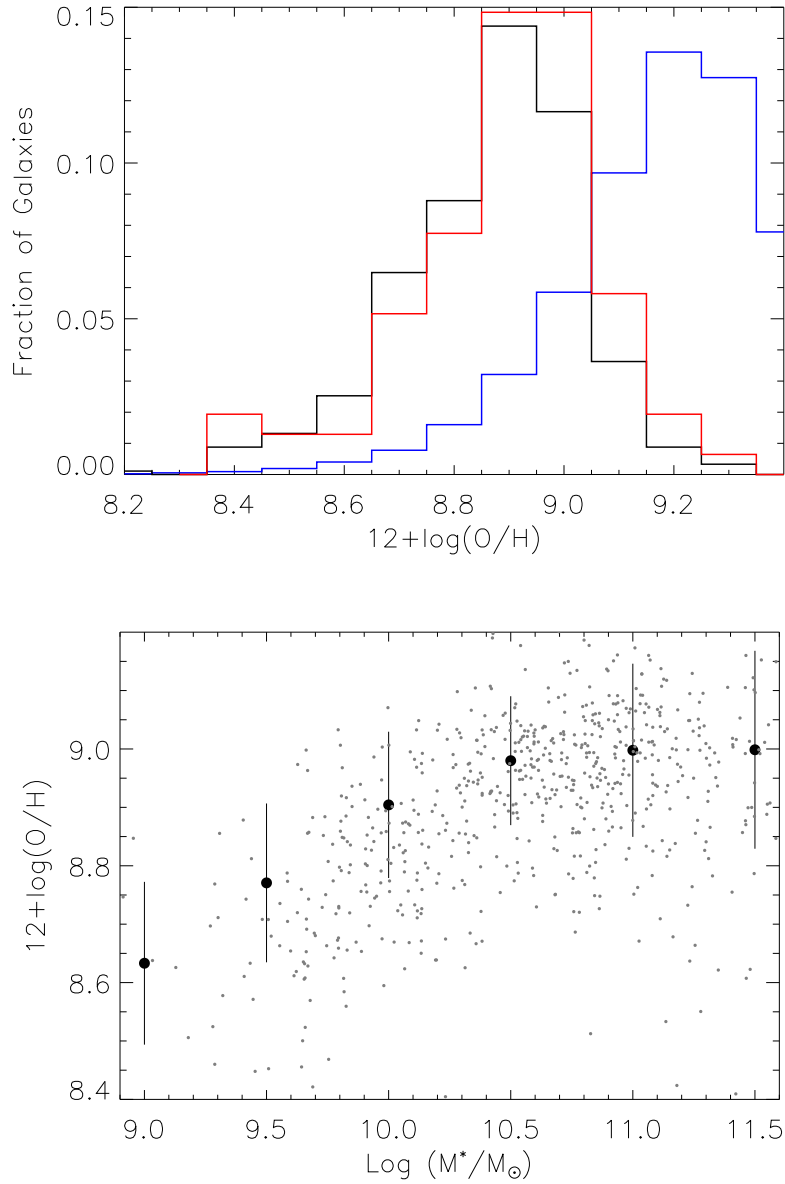


Figure 5.6 Metallicity as a function of stellar mass and distribution of metallicity. **Top:** The metallicity as a function of stellar mass estimates for the likely SN Ia host galaxy sample. The median value binned by stellar mass (intervals of $\Delta \log(m) = 0.5$) is shown by large filled circles with error bars representing the RMS within the bin. **Bottom:** The metallicity distribution of galaxies hosting SNe Ia in solid and core-collapse in dashed using spectroscopic redshift priors. In addition, the entire magnitude limited SDSS DR8 galaxy sample is shown in blue.

CHAPTER 6

SN IA LIGHT CURVE PROPERTIES

Using the full photometric classification method from Section 4.2, we examine properties of the sample based on the actual light curves. We use the SALT2 (Guy et al. 2007) approach to fit all of the candidate light curves, with a flat redshift prior and a spectroscopic redshift. We determine the light curve shape parameter x_1 , the color parameter c , and, in the case of a flat redshift prior, the best fit redshift. As in Section 4.3, we examine trends in contamination and completeness with the position of each transient in x_1 , c , and redshift space. We also report surprising behavior of the SALT2 fitter to underestimate redshifts in cases of poor data quality, leading to biases in interpretation of SN properties without spectroscopic redshifts of the host galaxies.

6.1 Effects of Light Curve Parameters on Contamination and Completeness

Here we estimate the rates of contamination and completeness in a purely photometric SN survey as a function of light curve parameters. As a baseline, we use the sample of 1128 transients that were classified as either photometric Ia or photometric Z Ia. For each of these transients, we then fit SALT2 light curves to the time domain photometry, assuming no redshift information. We use these fits to derive estimates of the x_1 parameter, the color c , and the photometric redshift derived from the light curve. In 337 cases, the light curve fits do not converge. These failures appear to be caused by low S/N data points and can not be used in this analysis. The resulting sample of 791 possible SN Ia is now examined for contamination and completeness after performing various cuts on the distributions of x_1 , c , and z parameters. As before, we define contamination as the fraction of events classified as photometric Ia that were not classified as a photometric Z Ia. Similarly, completeness is defined as the fraction of events classified both as a photometric Ia and photometric Z Ia relative to the sample of photometric Z Ia.

We evaluate the performance on various subsets of this sample selected on photometric z , x_1 , c , and an ellipse in $x_1 - c$ space. The contamination and completeness fractions for each subset are

¹⁰The results reported in this chapter have been submitted to the Astronomical Journal, referenced as “Host Galaxy Spectra and Consequences for SN Typing From The SDSS SN Survey,” Olmstead, M.D. et al., 2013, submitted to AJ, arXiv:6818.

shown in Table 6.1. Imposing a restriction on the best fit photometric redshift does little to change the contamination or completeness except when requiring $z < 0.2$. Surprisingly, the contamination increases at these low redshifts, possibly due to higher likelihood of observing core-collapse SNe. On the other hand, cuts on the x_1 and c parameters do reduce contamination as one would expect. Requiring $|x_1| < 2$ reduces contamination from 0.108 to 0.080 while keeping over 83% of the sample. A greater improvement on contamination arises when requiring $|c| < 0.2$; these tighter color restrictions decrease contamination from 0.109 to 0.074 and improve completeness from 0.924 to 0.941. C13 used simulations to determine the parameters of an ellipse in $x_1 - c$ space to maximize a figure of merit based on efficiency and purity. Using the new photometric classification, we reproduce their cuts; we find values of contamination and completeness of 0.063 and 0.936, respectively. We determined two elliptical cuts for our sample: one to maximize completeness and the other to minimize contamination. The ellipse to minimize contamination has semimajor axis $x_1 = 2.0$ and semiminor axis $c = 0.225$. To maximize completeness, we find an ellipse with semimajor axis $x_1 = 2.3$ and semiminor axis $c = 0.2$. These two cuts are very similar in SALT2 parameter and have very similar contamination, completeness, and sample size.

We compare the performance of these light curve parameter cuts with the performance of data quality cuts from Section 4.3. The best performance found in Section 4.3 occurred when requiring early time light curve coverage and late time light curve coverage, represented as the final entry in Table 4.4. The contamination, completeness, and total sample size were found to be 0.095, 0.965, and 511, respectively. The C13 cuts in Table 6.1 reduce contamination by a factor of 1.5, reduce completeness by a factor of only 1.015, and produce a sample size that is only 2.6% smaller.

C13 estimated contamination and the efficiency of selecting SNe Ia by tuning cuts on a large sample of simulated light curves. The primary limitation of this technique is that it requires a full understanding of SN rates to accurately populate the simulations. In this dissertation, we estimate contamination and efficiency based on the consistency of SN photometric classifications with and without host galaxy redshift information. The main limitation of this approach is that the true classifications of each transient is not known. These caveats aside, we compare the contamination and efficiency of the C13 results to our results. For ease of comparison, we define efficiency in our sample as the number of SNe Ia in a subset relative to the total number of SNe Ia in the sample (first entry in Table 6.1). C13 find a contamination of 8.3% and an efficiency of 71.6% using their cuts modeled on simulated data. We find a contamination of 6.3% and an efficiency of 70.0% (498/711) by applying those same cuts in $x_1 - c$ parameter space.

Table 6.1. Light Curve Restrictions

	Contamination	Number in photometric classified sample	Completeness	Number in redshift classified sample
No Cuts	0.109	737	0.924	711
$z < 0.5$	0.109	737	0.925	710
$z < 0.4$	0.110	692	0.926	665
$z < 0.3$	0.101	593	0.927	575
$z < 0.2$	0.139	318	0.920	298
$-4 < x_1 < 4$	0.107	719	0.926	693
$-3 < x_1 < 3$	0.100	697	0.926	677
$-2 < x_1 < 2$	0.083	617	0.934	606
$-0.4 < c < 0.4$	0.095	671	0.928	654
$-0.3 < c < 0.3$	0.080	602	0.936	592
$-0.2 < c < 0.2$	0.074	499	0.941	491
C13 $x_1 - c$ ellipse ($x_1 = 3.0, c = 0.25$)	0.063	497	0.936	498
$x_1 - c$ ellipse to minimize contamination ($x_1 = 2.0, c = 0.225$)	0.050	422	0.950	423
$x_1 - c$ ellipse to maximize completeness ($x_1 = 2.3, c = 0.2$)	0.054	423	0.952	420

6.2 Distribution of SN Light Curve Properties With Redshifts From the Host Galaxies

As a demonstration of the value of the photometric Z Ia sample for cosmology, we now perform an analysis on the completeness as a function of redshift. For each of these 1002 transients, we again fit SALT2 light curves to the time domain photometry, this time using the spectroscopic redshift information. We use these fits to derive estimates of the x_1 and c parameters. The light curve fits fail to converge for 97 of these transients, again due to low S/N. The failure rate, however, is much smaller than the rate found in Section 6.1 (337/1128). The much smaller failure rate is likely due to fewer free parameters in the light curve fits, demonstrating yet another advantage of host galaxy redshifts. The remaining sample of 905 photometric Z Ia SN are used to observe the distribution of the light curve properties with spectroscopic redshift.

Figure 6.1 shows the SALT2 parameters x_1 and c as a function of redshift for the entire photometric Z Ia sample. Both the distribution of x_1 and c shift with increasing redshift. At higher redshift, the sample tends towards higher values of x_1 and more negative values of c ; these trends are to be expected due to the well-known Malmquist bias (Malmquist 1936) in which only brighter SNe Ia are identified at higher redshift. This correlation begins roughly near $z = 0.3$. Assigning a turnover point at $z = 0.3$, we split the sample into low redshift and high redshift SNe Ia and fit simple linear models to demonstrate the effect of redshift incompleteness. For x_1 versus redshift, the slope of the low redshift and high redshift fit is consistent with 0. For c , we see a slope at low redshift of 0.09 ± 0.06 and at high redshift we determine a slope of -0.40 ± 0.06 . This analysis demonstrates the presence of Malmquist bias in the sample; a full correction must be applied from the cosmological perspective as done in C13.

6.3 SN Light Curve Properties With and Without Host Galaxy Redshifts

To determine the impact of redshift on the light curve properties, we return to the sample of 1128 transients that were classified as either photometric Ia or photometric Z Ia. This time, we fit a SALT2 light curve to each object twice, once allowing redshift as a free parameter, and once with the redshift constrained to that of the host galaxy. We use the sample of SNe Ia for which the SALT2 fits converged both with and without the host galaxy redshift. There are 773 SNe Ia that meet this criteria. We use the results to quantify the differences in the distributions of photometric redshift, x_1 , and c .

We first look at how the photometric redshift determined from the best-fit light curve compares to the spectroscopic redshift of the host galaxy (Figure 6.2). Instances in which a candidate is a photometric Ia and not a photometric Z Ia are highlighted independently; these are likely contaminants in the photometric Ia sample. The redshift determined photometrically from the SN Ia light curves is generally biased towards lower values. The line of best fit has a slope of

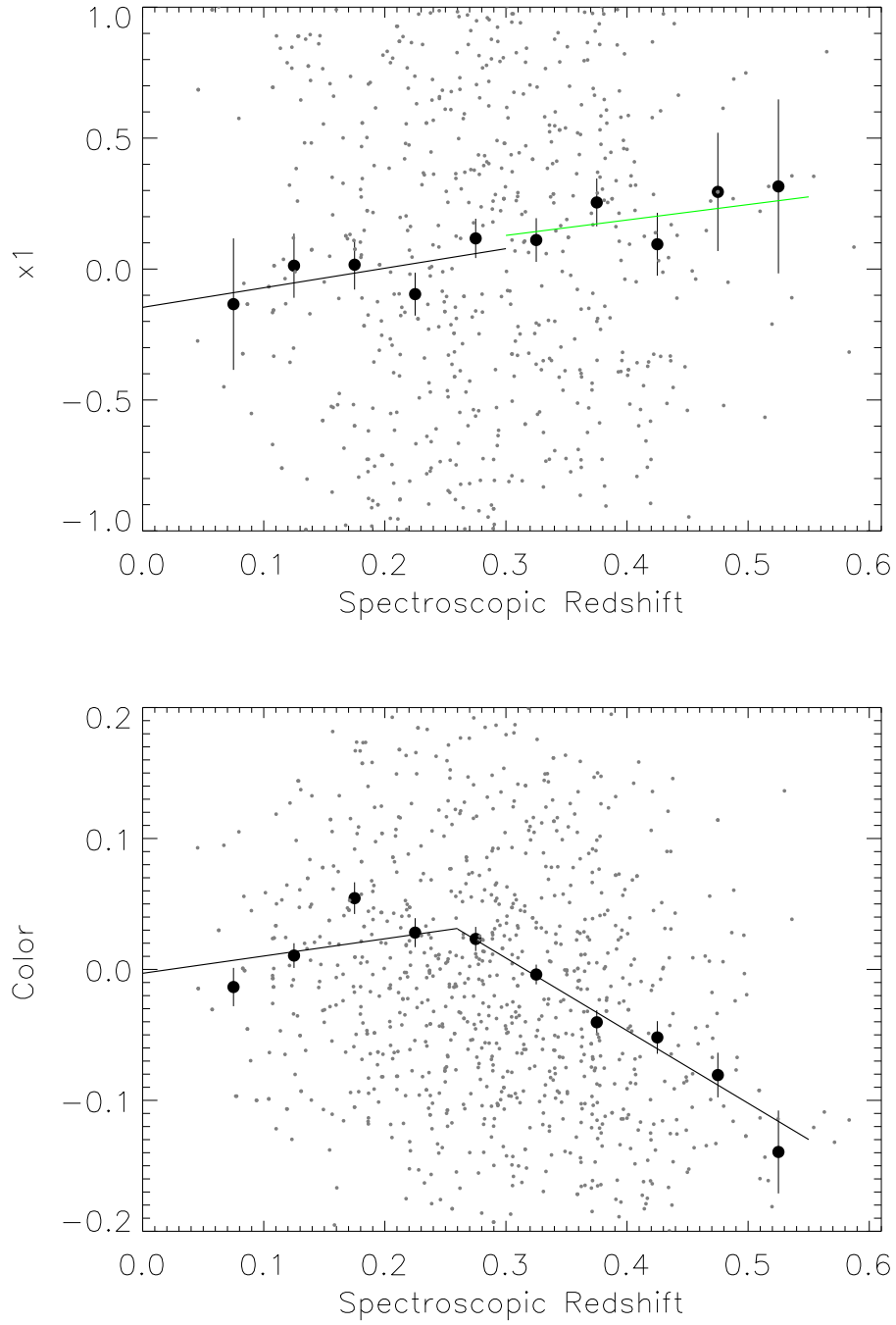


Figure 6.1 SALT2 parameters x_1 and c . **Top:** Measured x_1 using the redshift prior for the entire BOSS and SDSS sample of SNe Ia as a function of redshift. The larger filled circles are the mean of the data points in a redshift bin of 0.05 with RMS error bands shown. **Bottom:** Measured color when using redshift prior for entire BOSS and SDSS SNe Ia sample as a function of spectroscopic redshift. The larger filled circles are the mean of the data points in a bin in a redshift bin of 0.05.

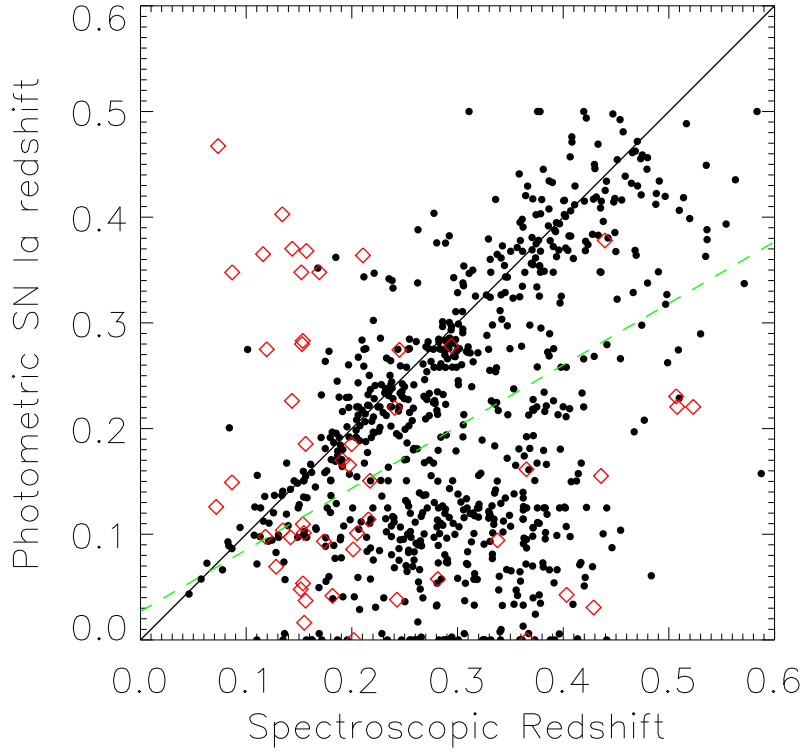


Figure 6.2 The best fit SN Ia photometric redshift versus the spectroscopic redshift. The black points represent candidates that are consistently classified as SNe Ia with and without spectroscopic redshifts. The red diamonds show the candidates identified as photometric Ia and not photometric Z Ia (likely contaminants). The solid black line simply represents a slope of unity. The dashed green line is the line of best fit to the black data points.

0.54 ± 0.39 , where one would expect a slope of unity for an unbiased photometric redshift. As described below, the poor estimate of the redshift manifests itself in the derived color parameters.

We examine the x_1 values determined by SALT2 with and without a spectroscopic redshift. Figure 6.3 demonstrates the impact of redshift knowledge on estimates of x_1 . Fitting a simple linear model to the x_1 values derived with photometric redshift as a free parameter relative to x_1 values derived with the spectroscopic redshift, we find no significant bias. The best-fit model has a slope of 0.98 ± 0.09 and y-intercept of -0.08 ± 0.09 .

We next examine the impact of redshifts on estimates of c . The top panel of Figure 6.4 compares estimates of c with no spectroscopic redshift to estimates with a host galaxy redshift. The SALT2 light curve fits clearly trend towards redder colors when redshift is included as a free parameter. This bias toward red colors occurs over the full range of true SN color with a bias described by a linear fit with intercept of 0.09 ± 0.02 and slope of 0.9 ± 0.3 . We again divide the data, this time

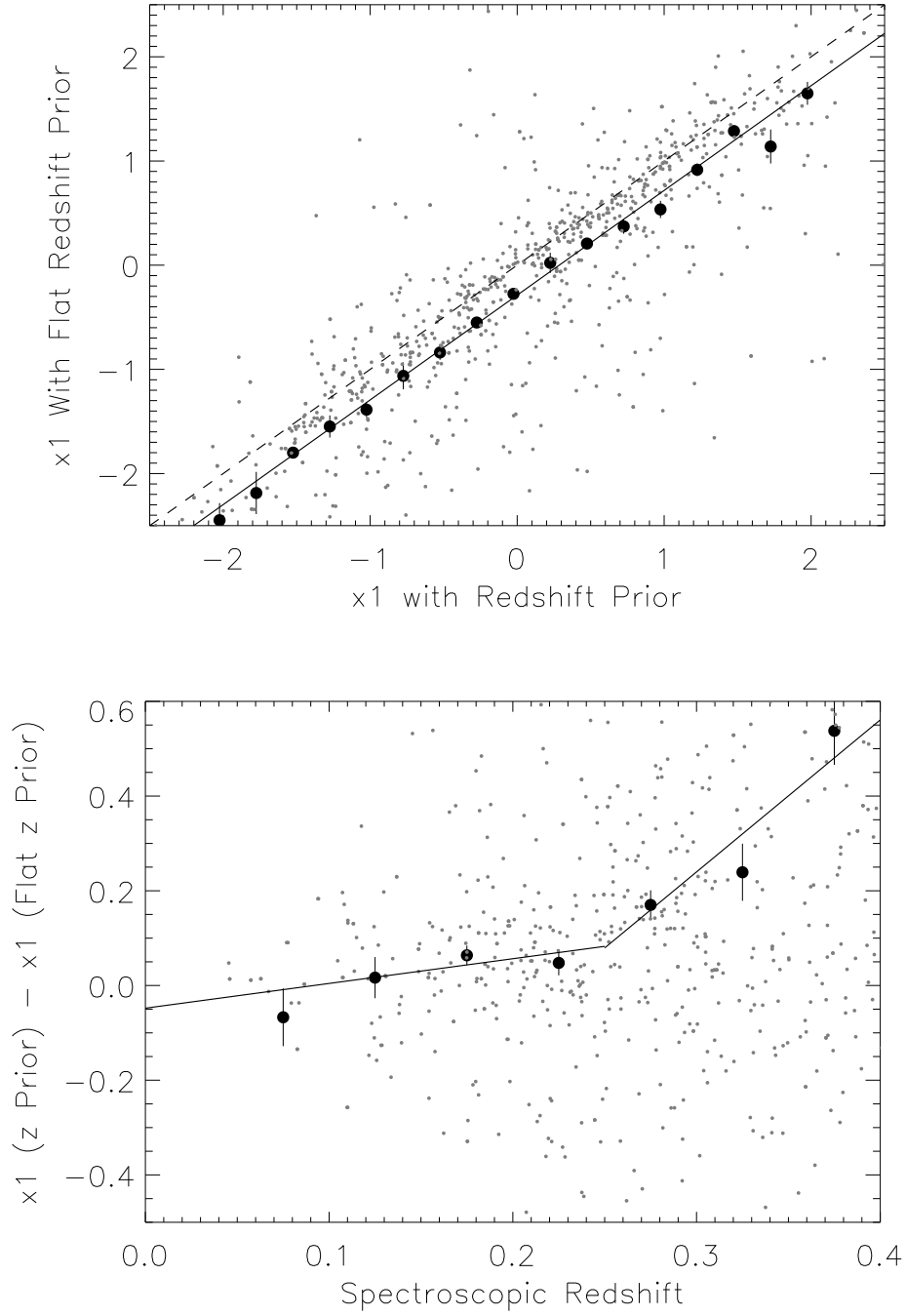


Figure 6.3 Comparisons of x_1 with and without spectroscopic redshift. Top: Measured x_1 with flat redshift prior versus x_1 with redshift prior shown with a line of slope equal one. Bottom: The difference between measured x_1 using spectroscopic redshift and measured x_1 assuming a flat redshift prior as a function of redshift.

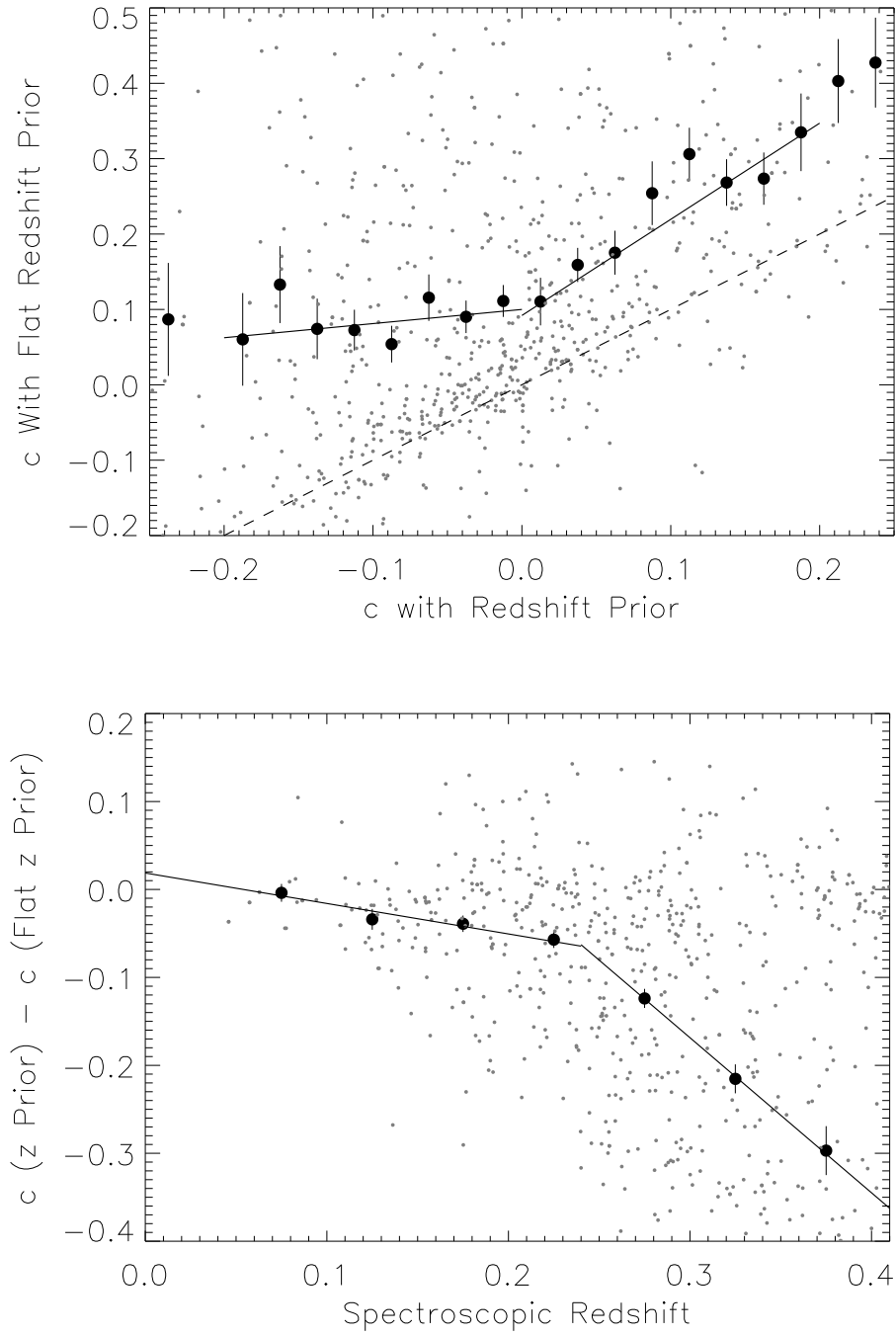


Figure 6.4 Comparisons of color with and without spectroscopic redshift. **Top:** Measured color with flat redshift prior versus color with redshift prior shown with a dashed line of unity. The solid line shows the line of best fit for the two redshift samples: $z < 0.3$ and $z \geq 0.3$. **Bottom:** The difference between measured c using spectroscopic redshift and measured c assuming a flat redshift prior as a function of redshift.

using the color estimates with redshift information. We make the cut at $c = -0.05$. We see a slope at low values of c of 0.2 ± 0.3 and for high values of c we determine a slope of 1.36 ± 0.07 . There is a significant change in estimates of c between the two data samples. The bottom panel shows that SNe at higher redshift produce more bias estimates of color when the precise redshift is not known.

The systematic underestimates in photometric redshift shown in Figure 6.2 are likely responsible for the bias in the distribution of color estimates shown in Figure 6.4. Figure 6.5 shows the relationship between bias in color estimates and bias in photometric redshift estimates. Candidates for which the photometric redshift is underestimated are also interpreted to be redder. As shown in the top panel, the effect is worse for high redshift SNe Ia than for low redshift SNe Ia. We attribute this trend to a general reduction in S/N and data quality at increasing redshift. To assess the effect of data quality, we examine the trend in bias for samples cut on the number of epochs sampling the light curve in the middle panel, and maximum S/N in the r -band in the bottom panel. As can be seen in the three panels, when including either low redshift SNe Ia, SNe with at least 10 r -band epochs with $S/N > 3$, or at least one r -band epoch with $S/N > 10$, the bias in both color and photometric redshift disappear. A simple linear fit to the data with spectroscopic redshift < 0.25 has a slope consistent with zero (0.03 ± 0.03) and a y-intercept of -0.011 ± 0.01 while the fit to the data at higher redshift has a slope of 0.20 ± 0.03 and a y-intercept of -0.09 ± 0.01 . Again we perform a simple linear fit to the data, but this time using the light curves with at least 10 r -band epochs with $S/N > 3$, we find a slope of 0.14 ± 0.04 and a y-intercept of -0.04 ± 0.01 while the fit to the data with fewer epochs has a slope of 0.22 ± 0.03 and a y-intercept of -0.09 ± 0.01 . Finally, we perform a simple linear fit to the data with at least one r -band epoch with $S/N > 10$, we calculate a slope of 0.09 ± 0.04 and a y-intercept of -0.03 ± 0.01 while the fit to the data with lower maximum S/N has a slope of 0.24 ± 0.03 and a y-intercept of -0.09 ± 0.01 .

The bias in color estimates will lead to a different interpretation of the elliptical cuts in C13 if one does or does not use host galaxy redshifts in the SALT2 fits. We reproduce the elliptical cuts described in Section 6.1 using the sample of 773 SNe Ia with light curve parameters determined with and without host galaxy information. These samples of photometric Ia and photometric Z Ia are shown with the elliptical cuts in $x_1 - c$ parameter space in Figure 6.6. A total of 706 (91.3%) of the photometric Z Ia sample lie within the ellipse, while only 73.4% of the photometric Ia sample lie within the ellipse. As a final test, we determine the number of photometric Z Ia inside the ellipse when using the SALT2 parameters determined with knowledge of the redshift. Using the sample of 905 photometric Z Ia with SALT2 light curve parameters described in Section 6.2, we find 790 (87.2%) SNe Ia inside the ellipse.

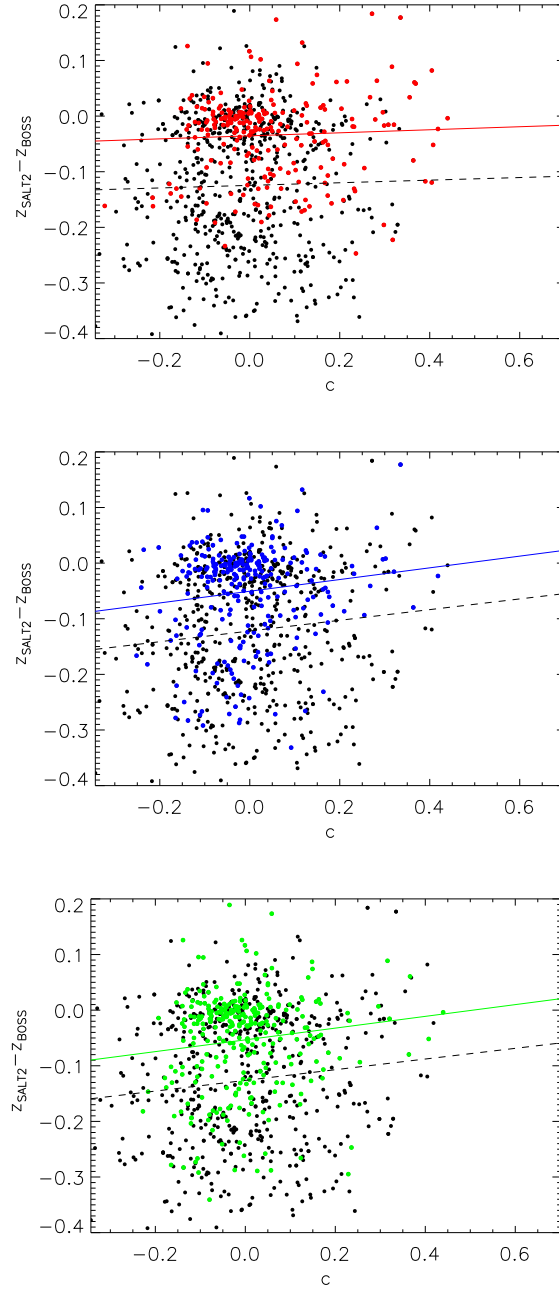


Figure 6.5 The difference between the SALT2 redshift estimate and the host galaxy spectroscopic redshift as a function of color for different data quality cuts. The solid, colored lines are the lines of best fit to the higher quality data. Top: The red dots represent the sample with $z < 0.25$. Middle: The blue dots represent the sample with at least 10 epochs with $S/N > 3$ in r -band. Bottom: The green dots represent candidates with at least one epoch of $S/N > 10$ in r -band.

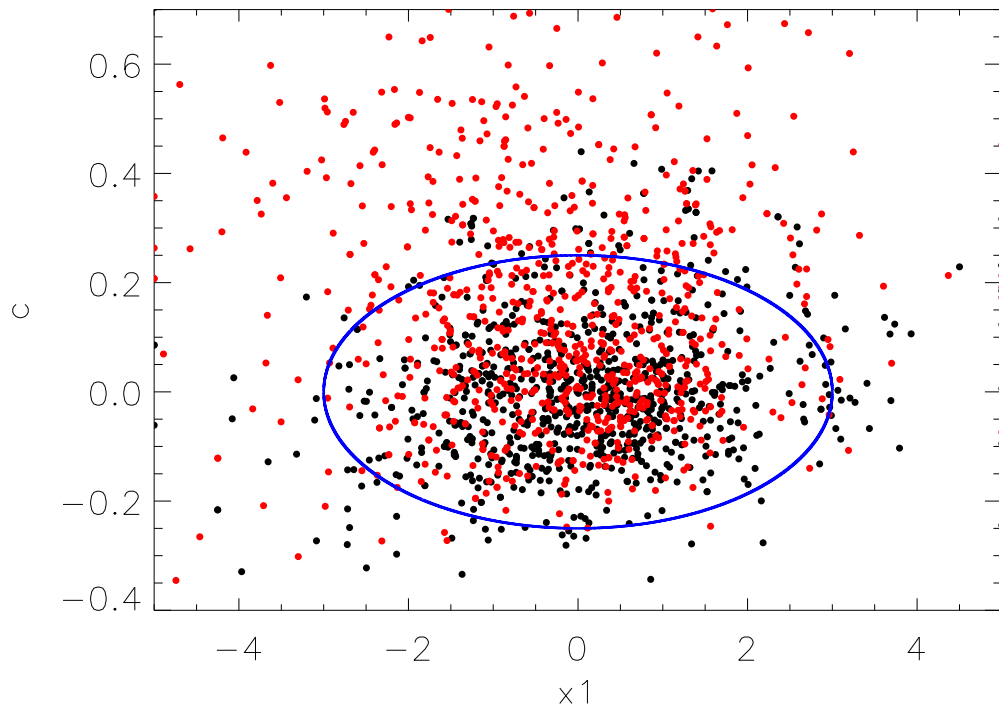


Figure 6.6 A plot of the SALT2 parameters c vs x_1 including the ellipse found in C13. The black points are determined using spectroscopic redshift as a prior and the red points are determined with a flat redshift prior.

CHAPTER 7

CONCLUSIONS

7.1 Summary

In this dissertation, I describe the impact of host galaxy spectra on the classification and interpretation of SN candidates from the SDSS-II SN data release. I begin in Chapter 1 with a general overview of SN astrophysics and cosmology. I continue in Chapter 2 with a description of the spectrographs used for host galaxy spectroscopy. I next guide the reader through the SDSS and BOSS host galaxy spectra and the DR10 galaxy product. I also provide analysis of the consistency in SN classification between a sample when only photometric data is available and a sample with well-constrained redshifts from host galaxy spectra. Finally, I show significant differences in SALT2 light curve properties depending on whether or not the host galaxy redshift is used in the fit.

In total, 2998 spectra were obtained with BOSS and 2292 spectra were obtained with SDSS. The redshift range for the combined sample is $0 < z < 4$. The range of redshifts for host galaxies of the transients determined to be SNe Ia with our most rigorous classification using host galaxy redshifts (“photometric Z Ia”) is $0.057 < z < 0.688$, and the range for the analogous core-collapse sample (photometric Z CC) is $0.041 < z < 0.562$.

Using the host galaxy spectroscopic redshift as a prior, I have photometrically typed these candidates using three different schemes. In previous work (Kessler et al. 2010; Bernstein et al. 2012), simulations were performed to test completeness and purity of SNe samples with only photometric information; here I apply an independent test by evaluating the consistency of photometric classification with and without spectroscopic redshift. I recommend using classifications derived from the nearest neighbor full photometric classification. With the full photometric classification, there are 1120 SNe Ia when using photometry alone and 1094 SNe Ia when using host galaxy redshifts. In total, 90 transients were classified as SNe Ia only when host galaxy redshifts were used; 126 transients were classified as SNe Ia when only photometric information was used. Assuming the typing with redshifts to be more accurate, I interpret this result to imply that the contamination of our sample using only photometric information is 12.1% and the completeness is 88.7%. I can reduce the contamination from 12.1% to 9.5% by additionally requiring both early time coverage and late time coverage. Slightly more than 50% of the SDSS-II SNe Ia meet this more stringent condition. I find larger improvements by filtering on the light curve parameters derived from a

photometric-only sample. By including photometric SNe with SALT2 x_1 and c parameter fits that lie within a simple ellipse defined in C13, I find a larger number of SNe Ia with only 4.8% contamination.

This sample of 522 photometric Ia with 4.8% contamination appears to demonstrate the usefulness of photometric only samples. However, the addition of redshift provides subtle, yet important, improvements on the sample of SNe Ia. First, when the spectroscopic redshift of the SN Ia is not known, there is an additional degree of freedom in the SALT2 light curve fits, leading to a larger number of fits that fail selection cuts. In addition, there is a bias in the estimate of photometric redshift and SN color that appears when the fits are performed without a redshift. These effects appear to be highly correlated with poor data quality and are significantly mitigated when the host galaxy spectroscopic redshifts are used.

For future large SN surveys there will be far too many candidate transients for full spectroscopic confirmation to be feasible. Obtaining the spectroscopic redshift of each host galaxy in multi-object spectroscopy is an efficient means to improve the science returns from these large samples. The host galaxy redshift constrains the redshift axis of the Hubble diagram. The addition of host galaxy spectra increases both the diversity of the host galaxy sample, allowing for fainter, more distant galaxies, and improves the observed host galaxy properties. Using the redshift removes a degree of freedom in light curve parameter space, thereby increasing the fraction of transients with reliable fits. Finally, using the host galaxy redshifts mitigates an apparent bias in the SN light curve fits tending toward lower redshift estimates and redder colors. The spectroscopic host galaxy properties can also be used to study the relationship between SN properties and the local environment. Stellar mass, absolute luminosity, velocity dispersion, star formation rate, and metallicity can be derived from a sample of galaxies observed in imaging and spectroscopy to investigate trends in Hubble residuals and SN rates. For these reasons, current SN projects such as DES and future projects such as LSST will benefit from a dedicated spectroscopic campaign to follow up host galaxies, even if the SN has faded.

7.2 Summary of Other Related Work

Here I provide a brief overview of four studies led by members of the SDSS SN Survey, where my work on the BOSS spectroscopy contributed to the final results.

As described in Section 3.5, C13 used a sample of photometrically-classified SNe Ia with host galaxy redshifts and performed a cosmological study. We found competitive results for $w = -0.96^{+0.10}_{-0.10}$, $\Omega_m = 0.29^{+0.02}_{-0.02}$ and $\Omega_k = 0.00^{+0.03}_{-0.02}$ when assuming a constant w CDM cosmological model and combining our SNe sample with H_0 , CMB, and LRG data. Figure 7.1 shows the Hubble diagram containing only photometrically-classified SNe Ia from the SDSS-II SN Survey. Figure 7.2 shows confidence contours of Ω_m - Ω_Λ for this sample in the solid lines, again comparable to the

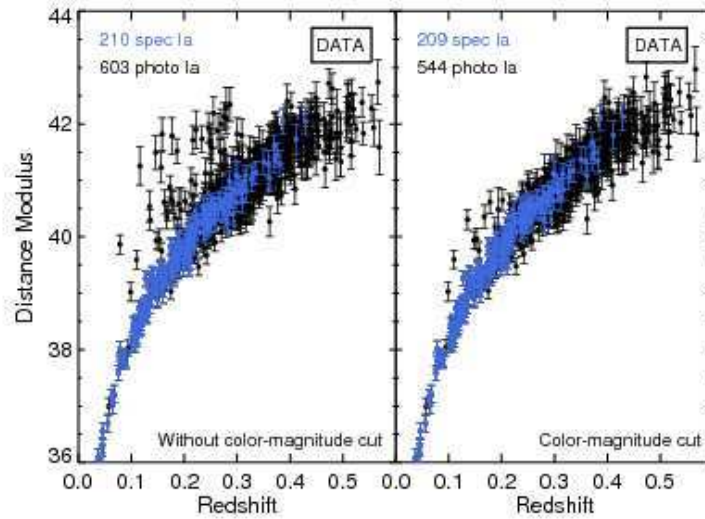


Figure 7.1 Hubble diagram for the photometrically-classified SNe Ia sample in C13. Blue points are the subsample of spectroscopically confirmed SNe Ia, while black points are new SNe Ia. Credit: Figure 16, “Cosmology with Photometrically Classified Type Ia Supernovae from the SDSS-II Supernova Survey,” Campbell, H. et al., *Astrophys. J.*, 763, 88. Reproduced by permission of the AAS.

spectroscopic results in Figure 1.6. These results are very promising for future SN surveys which will require accurate SNe Ia photometric classification.

In a different study, we examined the properties of 32 SNe Ia (11 spectroscopically-confirmed, 21 photometrically-classified) inside rich galaxy clusters (Xavier et al. 2013). Most of the characteristics were found similar to other SNe Ia, but the x_1 distribution of this sample was shifted lower than that of SNe Ia found in the field, where x_1 is a parameter that characterizes the rise and fall time of an SN Ia light curve, with small x_1 meaning a fast rise and fast fall. We also found evidence that x_1 of SNe Ia inside passive galaxies in rich clusters is smaller than x_1 of SNe Ia hosted in passive galaxies not in galaxy clusters. This is likely due to higher concentration of old passive galaxies in clusters. We also confirmed reports that SNe Ia in passive galaxies have smaller average x_1 and are ~ 0.1 mag brighter after light curve corrections.

In Galbany et al. (2012), we explored the SNe Ia properties as a function of distance from the center of the host galaxy. We used almost 200 SNe Ia with $z < 0.25$ and split the sample based on galaxy morphology. The distance to the center of the host galaxy was used as a proxy for local galaxy properties including star-formation rate and metallicity. We found a 4-sigma detection that

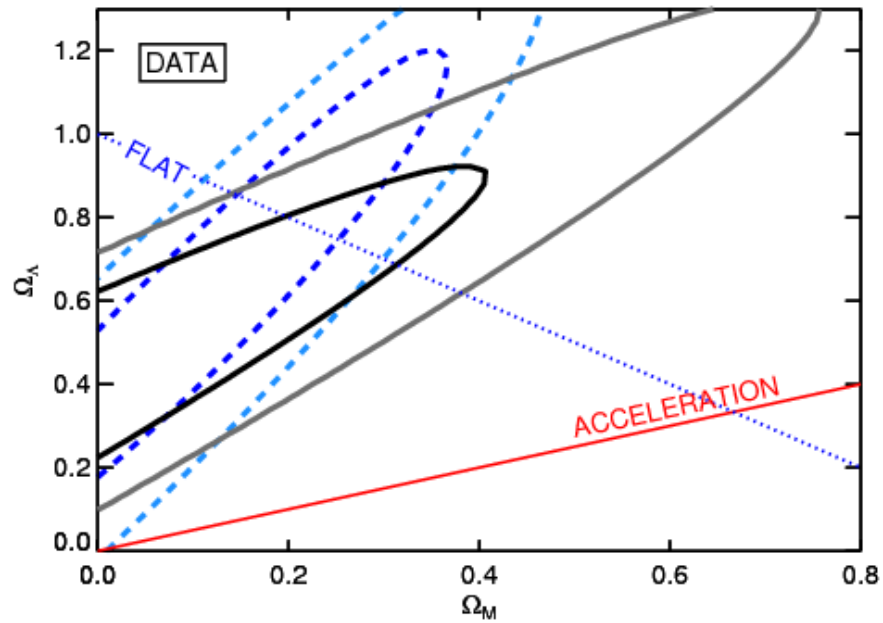


Figure 7.2 The 68% and 95% confidence contours of Ω_m versus Ω_Λ for a Λ CDM model using only the photometrically classified SNe from C13 and allowing curvature to vary. Only statistical errors in the contours are shown. The blue dashed contours show the comparable SNLS3 constraints taken from Guy et al. (2010). Credit: Figure 24, “Cosmology with Photometrically Classified Type Ia Supernovae from the SDSS-II Supernova Survey,” Campbell, H. et al., *Astrophys. J.*, 763, 88. Reproduced by permission of the AAS.

the SALT2 color parameter, c , decreases with distance in spiral galaxies. The sample also provides hints that SNe Ia in elliptical galaxies may have narrower light curves when they occur at large distances from the center of the host galaxy.

We also studied the correlation between spectroscopic properties of star-forming host galaxies SNe Ia Hubble residuals. We used the low redshift SNe Ia sample, $z < 0.15$ because this sample is nearly complete. The final sample contains ~ 40 emission line galaxies. The host galaxy spectra were used to obtain star-formation rates and gas-phase metallicities. We found a greater than 3-sigma detection of the correlation between Hubble residuals and the specific star-formation rate. We also found that SNe Ia in high-metallicity hosts are ~ 0.1 magnitudes brighter after light curve corrections.

7.3 Future Work

The large sample of photometrically-classified SNe Ia identified in Chapter 4 will provide an important selection of SNe Ia for future analysis. In addition, the collection of host galaxy spectra for all of these candidates will allow for a detailed analysis of correlations between host galaxy properties and SNe Ia properties. Instead of using derived quantities like stellar mass and metallicity, I will focus on the properties found purely in the spectra including equivalent line widths. I will perform principal component analysis using the SALT2 parameters of the SN and spectral parameters of the host galaxies. I anticipate that this will provide independent measures on the correlations between SN and host galaxy properties.

REFERENCES

- Abazajian, K. N., et al. 2009, *Astrophys. J., Suppl. Ser.*, 182, 543
- Adelman-McCarthy, J. K., et al. 2008, *Astrophys. J., Suppl. Ser.*, 175, 297
- Ahn, C. P., et al. 2012, *Astrophys. J., Suppl. Ser.*, 203, 21
- Aihara, H., et al. 2011, *Astrophys. J., Suppl. Ser.*, 193, 29
- Astier, P., et al. 2006, *Astron. Astrophys.*, 447, 31
- Badenes, C. & Maoz, D. 2012, *Astrophys. J., Lett.*, 749, L11
- Barbary, K., et al. 2012a, *Astrophys. J.*, 745, 32
- . 2012b, *Astrophys. J.*, 745, 31
- Barris, B. J., et al. 2004, *Astrophys. J.*, 602, 571
- Bebek, C., et al. 2002, in *Society of Photo-Optical Instrumentation Engineers (SPIE) Conference Series*, ed. M. M. Blouke, J. Canosa, & N. Sampat, Vol. 4669, 161–171
- Bernstein, J. P., et al. 2012, *Astrophys. J.*, 753, 152
- Bolton, A. S., et al. 2012, *Astron. J.*, 144, 144
- Bruzual, G. & Charlot, S. 2003, *Mon. Not. R. Astron. Soc.*, 344, 1000
- Campbell, H., et al. 2013, *Astrophys. J.*, 763, 88
- Cannon, R., et al. 2006, *Mon. Not. R. Astron. Soc.*, 372, 425
- Cappellari, M. & Emsellem, E. 2004, *Publ. Astron. Soc. Pac.*, 116, 138
- Chen, Y.-M., et al. 2012, *Mon. Not. R. Astron. Soc.*, 421, 314
- Colless, M., et al. 2001, *Mon. Not. R. Astron. Soc.*, 328, 1039
- Conley, A., et al. 2011, *Astrophys. J., Suppl. Ser.*, 192, 1
- Conroy, C., Gunn, J. E., & White, M. 2009, *Astrophys. J.*, 699, 486
- Csabai, I., Dobos, L., Trencsényi, M., Herczegh, G., Józsa, P., Purger, N., Budavári, T., & Szalay, A. S. 2007, *Astronomische Nachrichten*, 328, 852
- da Silva, L. A. L. 1993, *Astrophys. Space. Sci.*, 202, 215
- D’Andrea, C. B., et al. 2011, *Astrophys. J.*, 743, 172
- Dawson, K., et al. 2008, *IEEE Transactions on Nuclear Science*, 55, 1725
- Dawson, K. S., et al. 2009, *Astron. J.*, 138, 1271
- Dawson, K. S., et al. 2013, *Astron. J.*, 145, 10
- de Vaucouleurs, G. & Corwin, Jr., H. G. 1985, *Astrophys. J.*, 295, 287

- Dilday, B., et al. 2010a, *Astrophys. J.*, 715, 1021
- Dilday, B., et al. 2008, *Astrophys. J.*, 682, 262
- Dilday, B., et al. 2010b, *Astrophys. J.*, 713, 1026
- Doggett, J. B. & Branch, D. 1985, *Astron. J.*, 90, 2303
- Drinkwater, M. J., et al. 2010, *Mon. Not. R. Astron. Soc.*, 401, 1429
- Eisenstein, D. J., et al. 2011, *Astron. J.*, 142, 72
- Filippenko, A. V., Li, W. D., Treffers, R. R., & Modjaz, M. 2001, in *Astronomical Society of the Pacific Conference Series*, Vol. 246, IAU Colloq. 183: Small Telescope Astronomy on Global Scales, ed. B. Paczynski, W.-P. Chen, & C. Lemme, 121–+
- Foster, C., et al. 2012, *Astron. Astrophys.*, 547, A79
- Frieman, J. A., et al. 2008, *Astron. J.*, 135, 338
- Fukugita, M., Ichikawa, T., Gunn, J. E., Doi, M., Shimasaku, K., & Schneider, D. P. 1996, *Astron. J.*, 111, 1748
- Galbany, L., et al. 2012, *ArXiv e-prints*
- Gallagher, J. S., Garnavich, P. M., Caldwell, N., Kirshner, R. P., Jha, S. W., Li, W., Ganeshalingam, M., & Filippenko, A. V. 2008, *Astrophys. J.*, 685, 752
- Ganeshalingam, M., et al. 2010, *Astrophys. J.*, Suppl. Ser., 190, 418
- Gao, Y. & J., P. C. 2013, *ArXiv e-prints*
- González Hernández, J. I., Ruiz-Lapuente, P., Tabernero, H. M., Montes, D., Canal, R., Méndez, J., & Bedin, L. R. 2012, *Nature*, 489, 533
- Gunn, J. E., et al. 1998, *Astron. J.*, 116, 3040
- Gunn, J. E., et al. 2006, *Astron. J.*, 131, 2332
- Gupta, R. R., et al. 2011, *Astrophys. J.*, 740, 92
- Guy, J., et al. 2007, *Astron. Astrophys.*, 466, 11
- Guy, J., Astier, P., Nobili, S., Regnault, N., & Pain, R. 2005, *Astron. Astrophys.*, 443, 781
- Guy, J., et al. 2010, *Astron. Astrophys.*, 523, A7
- Hamuy, M., et al. 2006, *Publ. Astron. Soc. Pac.*, 118, 2
- Hamuy, M., et al. 1996a, *Astron. J.*, 112, 2408
- Hamuy, M., Phillips, M. M., Suntzeff, N. B., Schommer, R. A., Maza, J., & Aviles, R. 1996b, *Astron. J.*, 112, 2391
- Hayden, B. T., Gupta, R. R., Garnavich, P. M., Mannucci, F., Nichol, R. C., & Sako, M. 2013, *Astrophys. J.*, 764, 191
- Heger, A., Fryer, C. L., Woosley, S. E., Langer, N., & Hartmann, D. H. 2003, *Astrophys. J.*, 591, 288
- Hicken, M., Wood-Vasey, W. M., Blondin, S., Challis, P., Jha, S., Kelly, P. L., Rest, A., & Kirshner, R. P. 2009, *Astrophys. J.*, 700, 1097

- Holtzman, J. A., et al. 2008, *Astron. J.*, 136, 2306
- Hubble, E. 1929, *Proceedings of the National Academy of Science*, 15, 168
- Jha, S., Riess, A. G., & Kirshner, R. P. 2007, *Astrophys. J.*, 659, 122
- Johansson, J., et al. 2012, *ArXiv e-prints*
- Kessler, R., et al. 2010, *Astrophys. J.*, 717, 40
- Krughoff, K. S., Connolly, A. J., Frieman, J., SubbaRao, M., Kilper, G., & Schneider, D. P. 2011, *Astrophys. J.*, 731, 42
- Lampeitl, H., et al. 2010, *Astrophys. J.*, 722, 566
- Law, N. M., et al. 2009, *Publ. Astron. Soc. Pac.*, 121, 1395
- LSST Science Collaborations, Abell, et al. 2009, *ArXiv e-prints*
- Malmquist, K. G. 1936, *Medd. Stockholmes Obs.*, 26
- Maraston, C. & Strömbäck, G. 2011, *Mon. Not. R. Astron. Soc.*, 418, 2785
- Meyers, J., et al. 2012, *Astrophys. J.*, 750, 1
- Miknaitis, G., et al. 2007, *Astrophys. J.*, 666, 674
- Minkowski, R. 1941, *Publ. Astron. Soc. Pac.*, 53, 224
- Perlmutter, S., et al. 1999, *Astrophys. J.*, 517, 565
- Pettini, M. & Pagel, B. E. J. 2004, *Mon. Not. R. Astron. Soc.*, 348, L59
- Phillips, M. M. 1993, *Astrophys. J., Lett.*, 413, L105
- Rau, A., et al. 2009, *Publ. Astron. Soc. Pac.*, 121, 1334
- Riess, A. G., et al. 1998, *Astron. J.*, 116, 1009
- Riess, A. G., et al. 2004, *Astrophys. J.*, 607, 665
- Riess, A. G., et al. 2007, *Astrophys. J.*, 659, 98
- Rodney, S. A. & Tonry, J. L. 2010, *Astrophys. J.*, 715, 323
- Sako, M., et al. 2008, *Astron. J.*, 135, 348
- Sako, M., et al. 2011, *Astrophys. J.*, 738, 162
- Sarzi, M., et al. 2006, *Mon. Not. R. Astron. Soc.*, 366, 1151
- Scannapieco, E. & Bildsten, L. 2005, *Astrophys. J., Lett.*, 629, L85
- Schlegel, D. J., Finkbeiner, D. P., & Davis, M. 1998, *Astrophys. J.*, 500, 525
- Smee, S. A., et al. 2013, *Astron. J.*, 146, 32
- Smith, M., et al. 2012, *Astrophys. J.*, 755, 61
- Sullivan, M., et al. 2011, *Astrophys. J.*, 737, 102
- Sullivan, M., et al. 2006, *Astrophys. J.*, 648, 868
- Suzuki, N., et al. 2012, *Astrophys. J.*, 746, 85

- The Dark Energy Survey Collaboration. 2005, ArXiv Astrophysics e-prints
- Thomas, D., et al. 2012, ArXiv e-prints
- Whelan, J. & Iben, Jr., I. 1973, *Astrophys. J.*, 186, 1007
- White, M., et al. 2011, *Astrophys. J.*, 728, 126
- Wood-Vasey, W. M., et al. 2007, *Astrophys. J.*, 666, 694
- Xavier, H. S., et al. 2013, *Mon. Not. R. Astron. Soc.*, 434, 1443
- York, D. G., et al. 2000, *Astron. J.*, 120, 1579
- Zheng, C., et al. 2008, *Astron. J.*, 135, 1766